Search for a Higgs Boson Produced in Association with a W Boson at ATLAS

Dissertation der Fakultät für Physik

der

Ludwig-Maximilians-Universität München

vorgelegt von

Benjamin Ruckert

geboren in Kaufbeuren

München, im September 2009

Abstract

The Large Hadron Collider at CERN the most modern proton-proton collider and data taking will start in 2009, with a centre-of-mass energy of $\sqrt{s} = 7$ TeV. The ATLAS detector, which is one of two multi-purpose detectors at the Large Hadron Collider, is able to detect a Standard Model Higgs boson if it exists. This is one of the main tasks of the ATLAS experiment.

This thesis deals with a Standard Model Higgs boson produced in association with a W boson. The Monte Carlo study is based on physics events generated at the nominal centre-of-mass energy of the Large Hadron Collider of $\sqrt{s} = 14$ TeV. Large parts of this analysis have been done using the global Grid infrastructure of the Large Hadron Collider experiments. A mass range of the Higgs boson of $m_H = 130 - 190$ GeV has been taken into account. In this mass range, the Higgs boson dominantly decays into a pair of W bosons, leading to initially three W bosons: $WH \rightarrow WWW$. Two orthogonal analysis channels have been investigated in detailed studies of the background properties.

The first channel considers the leptonic decay of two W bosons, such that the leptons are of opposite charge. The third W boson then decays hadronically. The analysis is based on one-dimensional cuts, where the best cuts found are strict cuts on the transverse momenta of the leptons, a cut on the invariant mass of the jets, as well as a cut on the transverse jet momenta and the missing transverse energy.

The second decay channel studied is dedicated to the leptonic decay of all three W bosons. Again, cuts on the transverse momenta of the leptons and the jets have been proven to be efficient, as well as the use of the spatial correlation of the decay products of the Higgs boson. The invariant mass of the leptons with opposite sign has been emerged as a very efficient cut to reject dominant diboson background contributions.

The discovery reach of both channels separately as well as the combination has been calculated using Bayesian methods. The discovery reach is at maximum for a mass range of $m_H = 150 - 170$ GeV, with a peak for $m_H = 170$ GeV at 5.0σ. All results are scaled to an integrated luminosity of $\mathscr{L} = 30$ fb^{-1}, which corresponds to approximately three years of data-taking at the design luminosity of 10^{33} cm^{-2} s^{-1}. The associated WH production improves the discovery reach for a Standard Model Higgs boson at the ATLAS detector and would also be useful for precision measurements of the couplings of the Higgs boson.

Zusammenfassung

Der Large Hadron Collider am CERN ist der modernste Proton-Proton Beschleuniger und wird im Jahre 2009 mit der Datennahme bei einer Schwerpunktsenergie von $\sqrt{s} = 7$ TeV beginnen. Der ATLAS Detektor, einer von zwei Universalexperimenten am Large Hadron Collider, ist in der Lage, ein Standardmodell Higgs Boson zu finden, wenn es existiert. Dies ist eine der Hauptaufgaben des ATLAS Experiments.

Diese Arbeit befasst sich mit einem Standardmodell Higgs Boson, welches in Assoziation mit einem W Boson produziert wird. Die Monte Carlo Studie basiert auf simulierten Physik-Ereignissen, welche bei der nominellen Schwerpunktsenergie des Large Hadron Collider von $\sqrt{s} = 14$ TeV generiert wurden. Große Teile der Analyse wurden unter Zuhilfenahme der globalen Grid-Infrastruktur der Large Hadron Collider Experimente durchgeführt. Es wurde ein Massenbereich des Higgs Bosons von $m_H = 130 - 190$ GeV untersucht. In diesem Massenbereich zerfällt das Higgs Boson dominant in ein Paar von W Bosonen, was zunächst zu drei W Bosonen führt: $WH \rightarrow WWW$. Zwei orthogonale Analysekanäle wurden unter Berücksichtigung detaillierter Untergrundstudien untersucht.

Der erste Kanal befasst sich mit dem leptonischen Zerfall von zwei W Bosonen, sodass beide Leptonen die gleiche Ladung tragen. Das dritte W Boson zerfällt hadronisch. Die Analyse basiert auf eindimensionalen Schnitten, wobei strenge Schnittkriterien auf die Transveralimpulse der Leptonen sich als sehr effizient herausgestellt haben. Des weiteren werden Schnitte auf die invariante Masse der Jets, die transversalen Impulse der Jets und die fehlende transversale Energie durchgeführt.

Der zweite untersuchte Kanal setzt einen leptonischen Zerfall aller W Bosonen voraus. Harte Schnitte auf die transversalen Leptonimpulse sind auch hier effizient. Zusätzlich wird auf die transversale Energie der Jets geschnitten, sowie die räumliche Korrelation der Zerfallsprodukte des Higgs Bosons ausgenutzt. Ein Schnitt auf die invariante Masse der Leptonen mit unterschiedlicher Ladung ist besonders effizient gegenüber Untergrundanteilen aus dem Zerfall von W/Z-Boson-Paaren.

Sowohl für die einzelnen Kanäle, als auch für die Kombination wurde mit Hilfe Bayesischer Methoden das Entdeckungspotential berechnet. In einem Massenbereich von $m_H = 150 - 170$ GeV ist das Entdeckungspotential am grössten, mit dem Maximum von 5.0σ für $m_H = 170$ GeV. Alle Resultate wurden für eine integrierte Luminosität von $\mathscr{L} = 30$ fb^{-1} bestimmt; dies entspricht etwa einer Laufzeit von drei Jahren mit einer Design-Luminosität von 10^{33} cm^{-2}s^{-1}. Die assoziierte WH-Produktion verbessert das Entdeckungspotential für ein Standardmodell Higgs Boson am ATLAS Detektor und ist des weiteren für eine präzise Bestimmung der Kopplungen des Higgs Bosons geeignet.

Contents

Chapter 1

Introduction

The understanding of matter and its constituents has always been of interest for mankind. The knowledge gain from thought experiments of ancient philosophers to today's experiments is tremendous. The description of matter and the interaction of elementary particles culminated in the formulation of the Standard Model of particle physics beginning in the 1960s. This theory describes all known elementary particles and their interactions (without gravitation), these are: electromagnetic interaction, weak interaction and strong interaction. The Standard Model has regularly been challenged over the last decades and its predictions have been confirmed experimentally.

Nevertheless, the Standard Model has one main difficulty: it can not accommodate *a priori* masses of the weak gauge bosons. One mechanism to overcome this problem introduces a spontaneous symmetry breaking, called the Higgs-mechanism. The spontaneous symmetry breaking leads to a new particle, called Higgs boson which is the last particle missing to complete the Standard Model. There have been extensive searches carried out for this particle over many years, but with no discovery. The Large Hadron Collider at CERN, the largest experiment in human history, is about to start in autumn 2009 with a centre-of-mass energy of $\sqrt{s} = 7$ TeV[1] and a Higgs boson with the Standard Model couplings will be found, if it exists.

The focus of this thesis is the investigation of the discovery reach of the ATLAS detector to find a Higgs boson in the so-called associated WH-production channel, which is one of the several production and decay modes. This thesis discusses the so-called associated production of a Higgs boson with a W boson in a mass range

---

[1] Throughout this thesis so-called *natural units* are used, i.e. $\hbar = 1$ and $c = 1$.

of $130 - 190$ GeV from proton-proton collisions with a centre-of-mass energy of $\sqrt{s} = 14$ TeV.

This thesis comprises ten chapters. Chapter 2 gives a short introduction into the Standard Model of particle physics with a focus on the electroweak symmetry breaking mechanism. The Higgs boson as a result of the symmetry breaking is discussed, as well as more specific properties of the Higgs boson, like the production and decay of this particle. Chapter 2 closes with an overview on experimental results of the search for the Higgs boson. Chapter 3 introduces the Large Hadron Collider at CERN and discusses the properties of proton-proton collisions and the measurements of an important accelerator parameter, the luminosity. This is followed by chapter 4, which presents the ATLAS detector, one of the experiments to be carried out at LHC. All subdetectors and their features are introduced, as well as the computing infrastructure, which is an essential component of this global experiment. Chapter 5 introduces the physics objects, i.e. the reconstructed data to be used for analyses. The influence of the trigger and the preselection of interesting physics events is also discussed in chapter 5. The cut-based analysis of the associated production of a W boson and a Higgs boson is divided into two parts: chapter 6 discusses the mixed hadronic-leptonic decay $WH, H \rightarrow WW, WWW \rightarrow l\nu l\nu + 2$ jets while chapter 7 presents the orthogonal analysis of the fully leptonic decay, $WH, H \rightarrow WW, WWW \rightarrow 3l3\nu$. Both channels are subject to systematic uncertainties, which will be discussed in chapter 8. This is followed by the calculation of the discovery reach of both analysis channels separately as well as their combination, chapter 9. This thesis finishes with a summary and discussion of the results (chapter 10).

Chapter 2

Theoretical Foundations

2.1 The Standard Model of Particle Physics

The Standard Model of particle physics describes matter and the interaction of its constituents. These so-called elementary particles form two classes of particles, fermions and bosons. Fermions are spin 1/2 particles and constitute matter. Bosons are spin 1 particles and describe the fundamental interactions between all of those particles. There are different interactions (table 2.1), namely electromagnetic, weak and strong interaction. Gravitation is the fourth fundamental force, but is not included in the Standard Model. Being approximately 40 orders of magnitude weaker than the other three forces, this yields no problem for particle physics[1], fermions can be classified into three generations, see table 2.2, where the constituents of the first generation make up the matter of stable particles, e.g. protons or neutrons. Particles of other generations can also build particles, e.g. mesons or baryons, but those are not stable. In fact, in nature those exotic particles existed only shortly after the big bang and can only be created in high energetic particle collisions as they happen for example in particle accelerators or stars. As mentioned above, the Standard Model describes three different fundamental forces, which will be introduced in more detail below.

Boson	Mass [GeV]	Charge [e]	Range [m]	Interaction
γ	0	$< 5 \cdot 10^{-30}$	∞	electromag.
$W^\pm$	80.398 ± 0.225	± 1	10^{-18}	electroweak
Z^0	91.1876 ± 0.0021	0	10^{-18}	electroweak
g	0	0	10^{-15}	strong

Table 2.1: The gauge bosons of the Standard Model [1].

---

[1]It should be noted, that many extensions of the Standard Model exist, with the aim to unify the electroweak and strong interaction, so-called Grand Unified Theories (GUTs).

	1st gen.		2nd gen.		3rd gen.	
	Flavour	Mass [MeV]	Flavour	Mass [MeV]	Flavour	Mass [MeV]
Leptons	e	0.510999	μ	105.658	τ	1776.84
	ν_e	≈ 0	ν_μ	≈ 0	ν_τ	≈ 0
Quarks	u	$1.5-3$	c	1.27	t	171.2
	d	$3.5-64$	s	104	b	4.20

Table 2.2: Properties of the leptons and quarks of the Standard Model [1].

2.1.1 Strong Interactions

The underlying theory of the so-called strong force is called quantum chromodynamics (QCD). The strong force acts upon particles which carry a colour-charge, i.e. quarks and gluons. In a mathematical way, QCD is a local, gauge-invariant SU(3) quantum field theory. Each flavour of quarks (table 2.2) has three fields, called colour-triplets, e.g.

$$\mathbf{u} = \begin{pmatrix} u_r \\ u_g \\ u_b \end{pmatrix} \tag{2.1}$$

where each of the components is a four-dimensional Dirac spinor[2]. It can be shown that the gauge field can be expressed through eight matrices[3], which leads to eight independent gluon gauge fields. It should be stressed, that gluons carry colour charge itself, resulting in a self-interaction. Two main features of QCD are confinement and asymptotic freedom.

Confinement

It has been shown that the force between particles taking part in the strong interaction increases rapidly with distance. This means that those particles can not be separated; quarks will always build hadronic systems (mesons or baryons[4]) and it would take an infinite large amount of energy to separate two quarks. At some point the energy is sufficient to create new particles out of the vacuum, this is called pair-production. In other words: quark systems are always colour-neutral. This includes hadronic objects (so-called particle jets), that are reconstructed in a particle detector.

---

[2]r, g, b label the colour state. The primitive colours red, green and blue are chosen as a convention. Each colour-charge has an anticolour-charge, $\bar{r}, \bar{g}, \bar{b}$.

[3]These matrices are called Gell-Mann matrices.

[4]Mesons are particles comprised of one quark and one antiquark, while baryons are composed of three quarks.

Asymptotic Freedom

The interaction between quarks and gluons depends on the energy scale. At high energies (which translates into small distances) there is a very weakly interaction. This implies that quarks can move freely within nucleons without interaction[5]. As the quarks interact freely, i.e. the coupling strength is very small, the calculation is more easily than for confined systems and can be done using perturbation theory.

2.1.2 Electroweak Interactions

The electroweak theory is a combination of the electromagnetic and the weak force. This theory has been developed by Sheldon Glashow, Abdus Salam and Steven Weinberg[6]. As QCD, the electroweak theory is a Yang-Mills theory. It is based on the symmetry group $SU(2)_L \times U(1)_Y$ and will be briefly described below. The index L of the special unitary group $SU(2)$ denotes the weak left-handed isospin and the index Y of the unitary group $U(1)$ indicates the weak hypercharge. Before electroweak symmetry breaking, there are two fields. Matter fields (describing fermions) and gauge-fields. The gauge-fields correspond to the generators of the respective groups, where the field B_μ arises from the generator Y of the group $U(1)_Y$ and three fields $W_\mu^{1,2,3}$ of the group $SU(2)_L$. These correspond to the Pauli-matrices. As mentioned above, the group $SU(3)_C$ has eight generators (the Gell-Mann[7] matrices) which give the gluon fields $G_\mu^{1,\cdots,8}$.

The Standard Model Lagrangian

Without mass terms, the Lagrangian of the Standard Model can be written as

$$\begin{aligned} \mathcal{L}_{SM} &= -\frac{1}{4}G_{\mu\nu}^a G_a^{\mu\nu} - \frac{1}{4}W_{\mu\nu}^a W_a^{\mu\nu} - \frac{1}{4}B_{\mu\nu}B^{\mu\nu} \\ &+ \bar{L}_i iD_\mu\gamma^\mu L_i + \bar{e}_{Ri}iD_\mu\gamma^\mu e_{Ri} + \bar{Q}_i iD_\mu\gamma^\mu Q_i + \bar{u}_{Ri}iD_\mu\gamma^\mu u_{Ri} + \bar{d}_{Ri}iD_\mu\gamma^\mu d_{Ri} \end{aligned} \qquad (2.2)$$

This Lagrangian is invariant under local gauge transformations

$$\begin{aligned} \phi &\rightarrow \phi' = e^{ig\chi(x)}\phi \\ A^\mu &\rightarrow A'^\mu = A^\mu - \partial^\mu\chi(x) \end{aligned} \qquad (2.3)$$

As already said, this Lagrangian describes massless particles. Adding mass terms for the particles always leads to a violation of the $SU(2)_L \times U(1)_Y$ gauge

---

[5]Asymptotic freedom has been discovered by David Gross, Frank Wilczek and David Politzer in 1973. They were awarded the Nobel Prize in physics in 2004.

[6]They were awarded the Nobel prize in physics in 1979.

[7]Murray Gell-Mann was awarded the Nobel Prize in physics 1969 for his contributions and discoveries concerning the classification of elementary particles and their interactions.
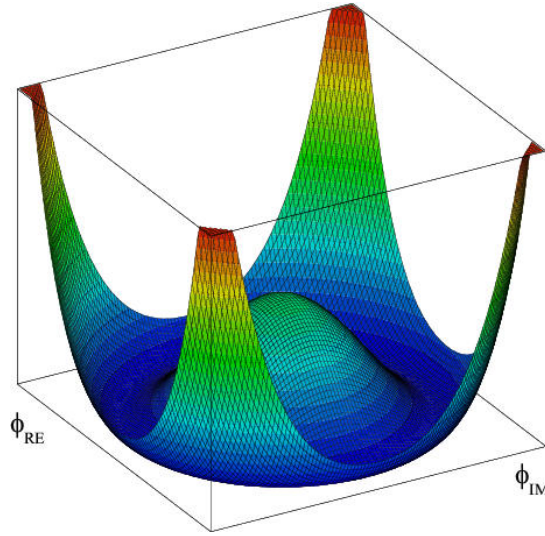
Figure 2.1: The Higgs potential.

invariance. The fact that particles have a mass (see table 2.1) means the symmetry must be broken. A possibility to generate gauge boson and fermion masses without violating the SU(2)×U(1) gauge invariance is the Higgs mechanism of spontaneous symmetry breaking, which will be described below.

2.2   The Higgs Mechanism

The Higgs mechanism[8] [2, 3, 4, 5] is a theory to generate the masses of bosons and fermions – without violating the gauge invariance – through a spontaneous symmetry breaking. In physics, a spontaneous symmetry breaking always leads to massless scalar particles, so-called Goldstone bosons [6]. In the electroweak theory, masses for the $W^{\pm}$ and Z bosons must be generated, while the photon has to remain massless. The simplest choice is a complex doublet of SU(2) scalar fields ϕ

$$\Phi = \begin{pmatrix} \phi^+ \\ \phi \end{pmatrix} = \frac{1}{\sqrt{2}} \begin{pmatrix} \phi_1 + i\phi_2 \\ \phi_3 + i\phi_4 \end{pmatrix} \tag{2.4}$$

where the ϕ_i are real fields. The invariant terms of the scalar field are

$$\mathcal{L}_s = (D^\mu \Phi)^\dagger (D_\mu \Phi) - \mu^2 \Phi^\dagger \Phi - \lambda (\Phi^\dagger \Phi)^2 \tag{2.5}$$

---

[8]In fact, this theory has been proposed by different people independently, namely by Peter Higgs, by Robert Brout and Francois Englert and by Gerald Guralnik, C. R. Hagen, and Tom Kibble. Therefore it can also be referred to as Higgs-Brout-Englert-Guralnik-Hagen-Kibble mechanism.

where $T = (D^\mu \Phi)^\dagger (D_\mu \Phi)$ is a kinetic term and $V = \mu^2 \Phi^\dagger \Phi + \lambda (\Phi^\dagger \Phi)^2$ represents the potential of the Lagrangian (illustrated in fig. 2.1). The product

$$\Phi^\dagger \Phi = \frac{1}{2} \left(\phi_1^2 + \phi_2^2 + \phi_3^2 + \phi_4^2 \right) \tag{2.6}$$

(and therefore the potential $V(\Phi)$) is invariant under local gauge transformations. The parameter $\lambda > 0$, so that the potential is bounded from below. When calculating the minimum of the potential for $\mu^2 < 0$, it can be seen that the minimum is at

$$\Phi^\dagger \Phi = -\frac{\mu^2}{2\lambda} =: \frac{v^2}{2} \tag{2.7}$$

In a field theory, the vacuum expectation value represents the ground state and excitations are particles. The Lagrangian in the vicinity of the minimum defines the particles. Hence, by expanding the Lagrangian in radial and longitudinal direction around v, a field with a mass $m_H = \sqrt{2\lambda v^2}$, as well as other massive particles (the $W^\pm$ and Z bosons), can be identified. Excitations in the direction of the minimum (see fig. 2.1) experience no force and therefore are massless. The expansion also leads to further terms, interpreted as interaction terms which define the production and decay of the Higgs boson (chapter 2.3). A more detailed derivation of the Higgs mechanism can be found in [7].

The Higgs boson should occur in nature, e.g. at high-energetic collisions at particle accelerators. The mass of the Higgs boson depends on the parameters λ and v. While the mass of the gauge boson determines v, the parameter λ of the scalar potential remains unknown. Hence, the mass of the Higgs boson is unknown and can not be calculated. Nevertheless, from precise measurements of other Standard Model parameters it is possible to set limits on the mass of the Higgs boson (chapter 2.5.2).

2.3 Production Mechanisms and Decay Modes of the Higgs Boson

2.3.1 Production Mechanisms of the Higgs Boson at LHC

There are four different ways to produce a Higgs boson at the LHC:

- gluon-gluon fusion: in a top quark loop, two gluons can produce a Higgs boson. At LHC the gluon-gluon fusion is the process with the largest production cross-section (figure 2.2a).

- vector boson fusion: the fusion of two W or Z bosons can produce a Higgs boson. There are also two quarks which hadronise and form jets. This process has the second-highest production cross-section at LHC (figure 2.2b).

(a) gluon-gluon fusion

(b) vector boson fusion

(c) associated production with W or Z bo-
son

(d) associated production with $t\bar{t}$
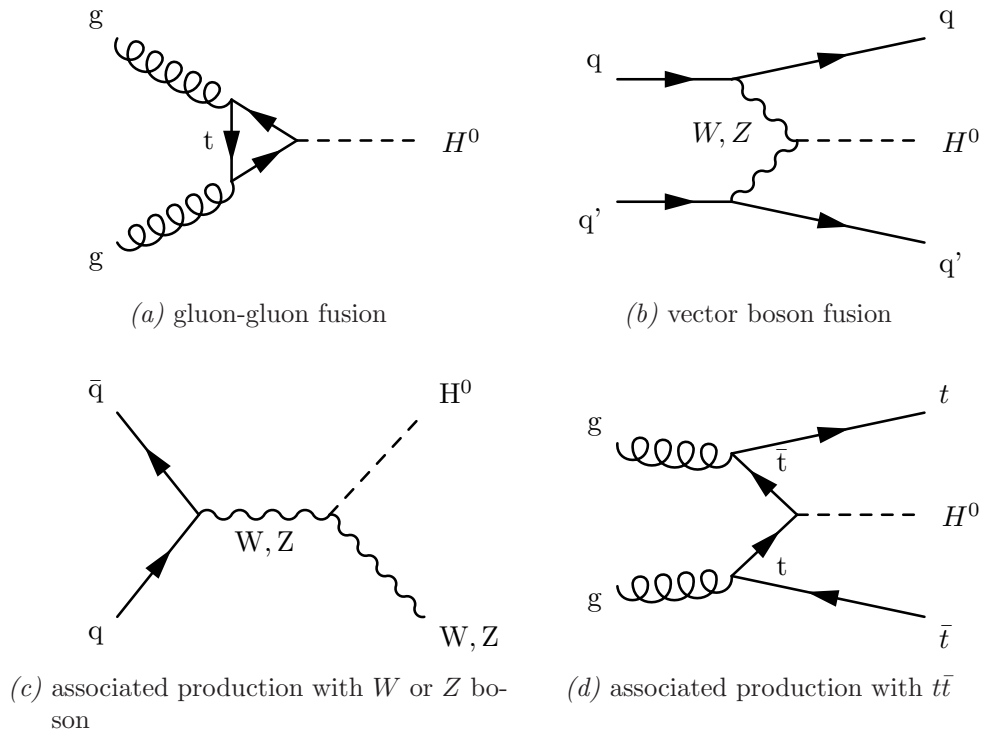
Figure 2.2: The different production mechanisms of the Higgs boson.
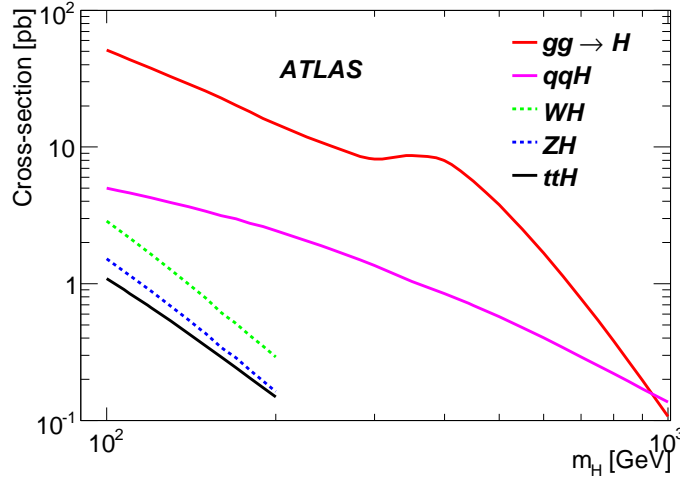
Figure 2.3: The cross-sections of the different production channels of the Higgs boson
at LHC. The numbers are calculated for a centre-of-mass energy of $\sqrt{s} =$
14 TeV.

- associated production with a W boson or a Z boson: the Higgs boson
  is radiated off a W or a Z boson. The first case, henceforth called WH
  production is the subject of this thesis (figure 2.2c).

- associated production with a $t\bar{t}$ pair: this channel has the lowest production
  cross-section, but can become important for a low mass Higgs, where the
  decay $H \to b\bar{b}$ is dominant (figure 2.2d).

The production cross-sections for each of these processes are illustrated in
figure 2.3. It becomes clear, that gluon-fusion is the dominant production mech-
anism, several orders of magnitude larger than vector boson fusion. For example,
for $m_H = 130$ GeV the production cross-sections is 31.76 pb for gluon-gluon fu-
sion and 4.13 pb for vector boson fusion, while the production of a Higgs boson
in association with a W boson has a production cross-section of only 1.35 pb.

2.3.2 Decay Modes of the Higgs Boson

The mass-dependent branching ratios of the Higgs boson are shown in figure
2.4. The predominant decay mode of the Higgs boson depends on its mass. In
the low mass region, where 100 GeV$< m_H <$ 140 GeV the Higgs boson mainly
decays into a pair of b quarks: $H \to b\bar{b}$. This channel is hard to investigate,
because of the large background; the main analysis channel for this will be $t\bar{t}H$,
where the $t\bar{t}$ pair decays semileptonically. The decay $H \to \gamma\gamma$ has a very low
branching ratio, but produces a clear signal. This channel could be used for
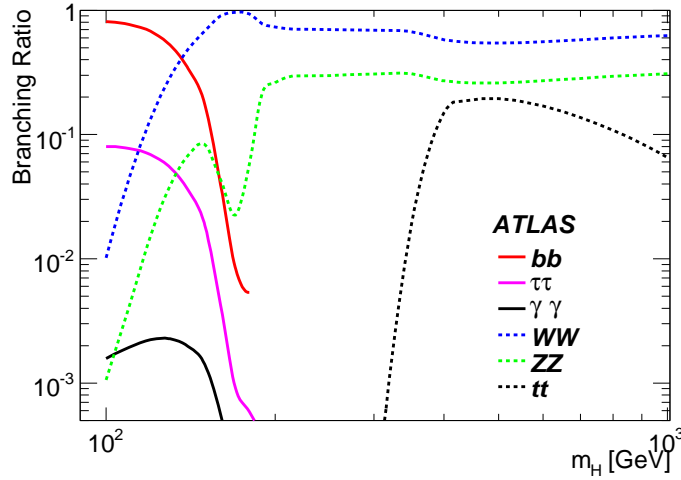
Figure 2.4: The mass-dependent branching ratios of the Higgs boson.

a precise determination of the Higgs boson mass. The decay into a pair of Z bosons, $H \rightarrow ZZ$ with a subsequent leptonic decay of the Z bosons is a feasible channel over a wide mass range (see fig. 2.4) and could be used for an early detection, because of the clear signal. The decay of the Higgs boson into two W bosons, $H \rightarrow WW$ has the largest branching ratio over a wide mass range ($m_H > 140$ GeV) and is the focus of many studies. The analysis presented in this thesis also uses this decay mode, but the Higgs boson is accompanied by an extra W boson: $WH \rightarrow WWW$. This is the so-called production of a Higgs boson in association with a W boson, or shortly referred to as WH production. Tables 2.3 and 2.4 summarise the production cross sections and the branching ratios for this channel.

m_H [GeV]	130	140	150	160	170	180	190
σ_{NLO} [pb]	1.3463	1.0612	0.8456	0.6814	0.5547	0.3772	0.3772

Table 2.3: The production cross sections of the associated WH production, calculated to Next-to-leading order [8].

m_H [GeV]	130	140	150	160	170	180	190
$H \rightarrow WW$	0.2888	0.4854	0.6831	0.9015	0.9654	0.9346	0.7761

Table 2.4: The branching ratios $H \rightarrow WW$ have been calculated with HDECAY [9].

2.4 Background Processes

In this section the most important background processes will be introduced. As mentioned before, the focus of this thesis is the investigation of the associated WH production, with a decay of the Higgs boson into two W bosons, $H \rightarrow WW$. As will be discussed in more detail later, the final states considered are

- $WH, H \rightarrow WW$ with $WWW \rightarrow 2l2\nu + 2$jets, with $(l = e, \mu)$

- $WH, H \rightarrow WW$ with $WWW \rightarrow 3l3\nu$, with $(l = e, \mu)$

The selection of signal events is complicated because of the contamination with background events. These are processes which show – at least in parts – similarities with the topology of the signal process. For example, the kinematics of the decay products could resemble that of the signal and thus fake a signal event. The predominant background processes for this analysis are

- $W^{\pm}Z$ production: this diboson process has many similarities with the signal process, e.g. the decay into two or three leptons, which are accompanied by neutrinos and/or hadronic activity (i.e. jets), the Feynman diagram is shown in fig. 2.5a.

- ZZ production: both Z bosons must decay leptonically in order to contaminate the signal. The branching ratio of $Z \rightarrow ll$ is 3.36%, hence this background gives only a minor contribution, see fig. 2.5b.

- W^+W^- production: another diboson background, but with only low impact, because of only two leptons and no hadronic contribution (high energetic jets). No third high energetic lepton can be expected from the signal, figure 2.5c.

- $t\bar{t}$: top quarks almost exclusively decay into a W boson and a b quark, $t \rightarrow Wb$. Hence, two leptons (and accordingly neutrinos) can be created from the decay of the W boson. Additionally, the decay of a b quark can lead to jets or an additional lepton through the decay into a charm quark via weak interaction: $b \rightarrow Wc$ The topology of the $t\bar{t}$ decay is not very similar to that of the signal, but $t\bar{t}$ production has a very large production cross section ($\sigma = 833$ pb [10]) and even a small amount of misreconstructed events can contaminate the signal selection, fig. 2.5d.

- $W+$ jets: the decay of one W boson can only lead to a single, high-energetic lepton. In order to contribute to the signal, the jets have to be misreconstructed. If, for example, a jet is misidentified as lepton, it can possibly fake a signal event. Especially, if the W boson is produced with more than one jet. This process has a very large cross section, but as will be shown

(a) $W^{\pm}Z$ production

(b) ZZ production

(c) $W^{+}W^{-}$ production

(d) $t\bar{t}$ production
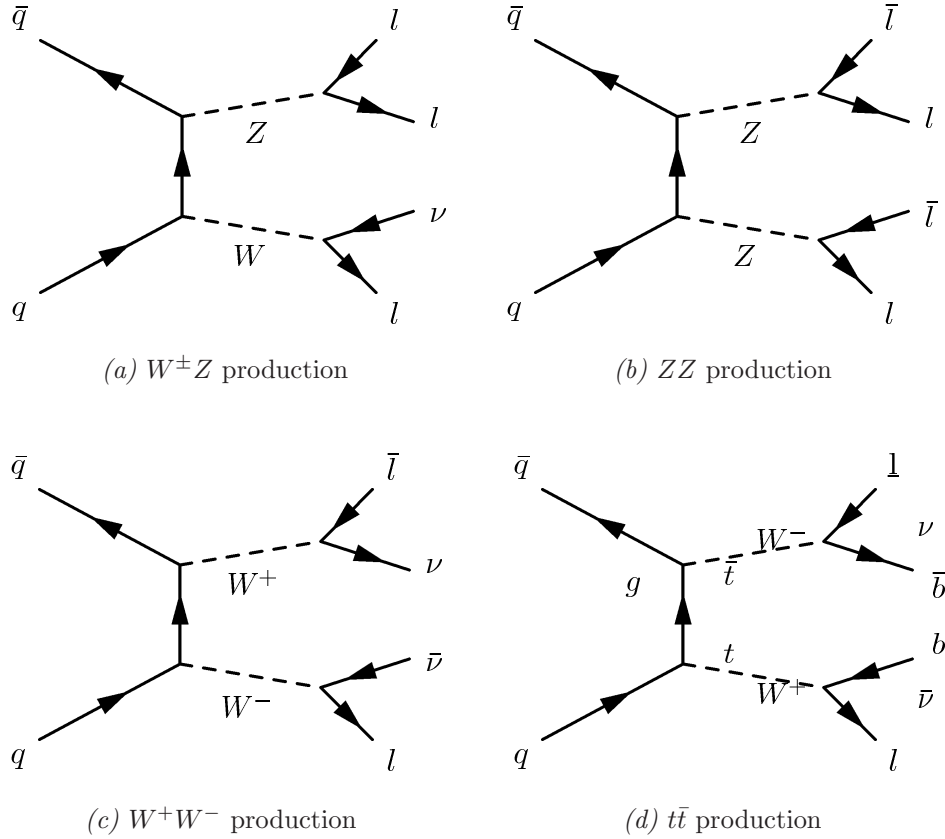
Figure 2.5: The background processes which are relevant for this analysis.

later, can be controlled very well. The same applies, if the jets are due to the decay of heavy quarks that have been produced in association with a W boson, e.g. $Wb\bar{b}$ or Wt.

Table 2.5 summarises important information the background processes. More details on the Monte Carlo samples used for this study can be found in chapter 6.

Process	WZ	ZZ	WW	$t\bar{t}$	W+jets	$Wb\bar{b}$	Wt
Cross section [fb]	49950	14750	112000	833000	$20 \cdot 10^6$	27000	66000

Table 2.5: The production cross sections of the background processes [11]. No filters have been applied.

2.5 Summary of Experimental Results

Extensive searches for the Higgs boson have been carried out over the last decade, so far without a discovery. In this section the status of the experimental status will be presented. This includes not only direct searches through analysing the decay products of high-energetic particle collisions, but also setting constraints on the mass of the Higgs boson through precision measurements of Standard Model parameters.

2.5.1 Direct Measurements

Results of LEP experiments

The experiments at LEP[9] were the first to search for the Higgs boson. At the end of the running period no evidence could be found, nonetheless it was possible to set a lower limit on the mass of the Standard Model Higgs boson [12]: $m_H > 114.4$ GeV at 95% C.L.

Higgs Searches at Tevatron

The Tevatron experiments at Fermilab[10] have been searching for the Higgs boson, but until summer 2009 have not found any evidence. Combining the Higgs analyses of both experiments (D0 and CDF), it was possible to exclude the mass of a Standard Model Higgs boson within a mass range of $160 - 170$ GeV at 95% C.L. [13].

2.5.2 Constraints through Indirect Measurements

Electroweak Precision Measurements

It has been mentioned above, that it is impossible to calculate the mass of the Higgs boson, because of the unknown self-coupling λ. However, from precision measurements of electroweak Standard Model parameters it is possible to constrain the mass. Figure 2.6 shows the results of measurements of LEP-1 and SLD (solid line) and LEP-2 and Tevatron (dashed line) of m_t and m_W. The green shaded area shows the Standard Model prediction on these masses for different masses of the Higgs boson which are correlated with the Fermi Constant G_f. That implies, that from a precise knowledge of m_W and m_t it is possible to constrain the mass of the Higgs boson. The impact of these measurements on the Higgs boson mass are shown in figure 2.7. A fit of all electroweak parameters

---

[9]**L**arge **E**lectron **P**ositron Collider was a collider at CERN from 1990 to 2000 with four experiments, ALEPH, L3, Delphi and OPAL.

[10]Tevatron is a $p\bar{p}$ accelerator at Fermilab National Accelerator Laboratory in Batavia, Illinois. At Tevatron the top quark has been discovered in 1995.
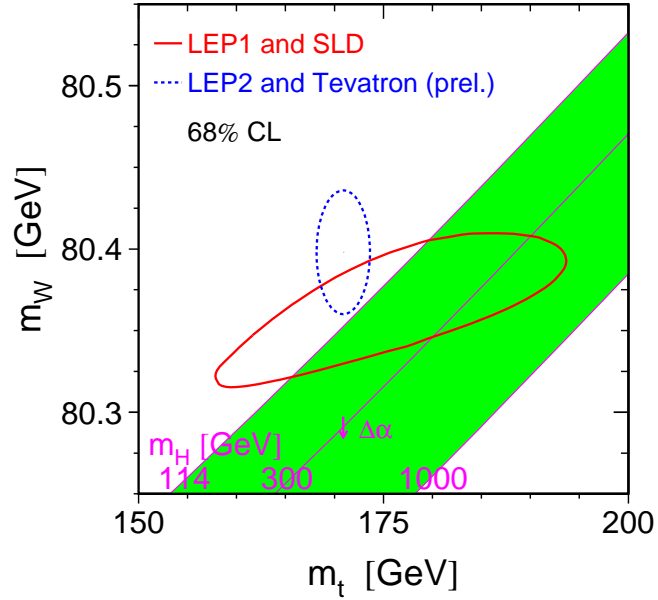
Figure 2.6: The comparison between the direct and indirect determinations of m_t and m_W.

constrains the mass of the Higgs boson, where the upper limit is calculated to be 144 GeV. The yellow shaded area denotes the mass region excluded by LEP in direct searches. Including this result raises the limit to $m_H \leq 182$ GeV [14].
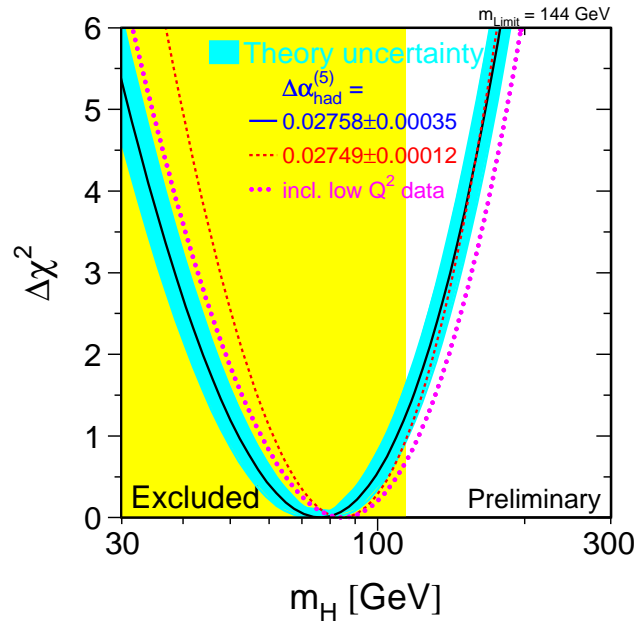
Figure 2.7: The determination of Higgs boson mass limits, obtained through electroweak precision measurements.

Chapter 3

The Large Hadron Collider

3.1 The LHC

The Large Hadron Collider (LHC) at CERN is todays most modern particle accelerator, see figure 3.1. It accelerates bunches of protons and collides them at centre-of-mass energies of up to $\sqrt{s} = 14$ TeV. Furthermore, LHC has the capability of accelerating lead ions to centre-of-mass energies of up to $\sqrt{s} = 2.76$ TeV per nucleon.

The accelerator has been built in the tunnel of the former LEP collider and a circumference of approximately 26.7 km. The LEP collider accelerated beams of electrons and positrons but at high energies synchrotron radiation makes circular electron accelerators not feasible[1].

The protons used for acceleration are stripped-off hydrogen atoms. These get accelerated by four succeeding pre-accelerators before being injected into the LHC ring. The first part is a linear accelerator (Linac) which accelerates the protons to energies of 50 MeV. This is followed by a chain of three circular accelerators, which boost the proton bunches ($\approx 10^{11}$ particles) stepwise to 1.4 GeV, 26 GeV and finally 450 GeV [15].

The LHC ring consists of superconducting magnets (fig. 3.2) and two beam pipes, one for each proton beam. The focussing and bending of the particle beams is done through magnets which act as optical lenses: dipole magnets are used for bending, while quadrupoles are used for focussing (and defocussing) and higher order magnets (sextupoles and octopoles) are used for corrections to the beam structure. Both beams being made of protons (i.e. the particles have the same charge), the magnetic field in the beam pipes must be of opposite direction. This is achieved by two single-dipoles, each around a beam-channel, both contained in the same structure. The LHC is built of 1232 such dipole magnets, the cold mass is helium, which is operated in the superfluid state at 1.9 K. The magnet

---

[1]Synchrotron radiation is emitted by relativistic charged light particles when being deflected by a magnetic field.
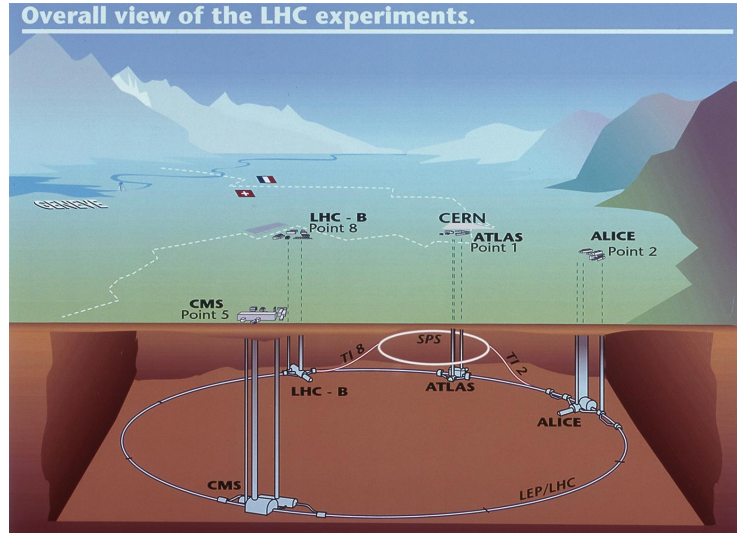
Figure 3.1: A sketch of the LHC complex, also showing the main experiments.

strength of the dipoles reaches up to 8.5 T.

There are four different experiments at the LHC. Two multi-purpose experiments, called ATLAS[2] and CMS[3], have been built for a wide research on high energy physics. They will search for new physics like Supersymmetry and perform precision measurements of Standard Model parameters, e.g. the top-quark mass or the W-boson mass. In contrast to these multi-purpose experiments, there are more specialised ones: the LHCb experiment is specialised on B-physics, i.e. the study of b-mesons and the CP-violation. As mentioned earlier, LHC is capable of accelerating lead ions. The ALICE detector[4] is dedicated to research on lead-ion collisions to study the quark-gluon plasma.

3.2   Proton-Proton Collisions

In the late 1960s it became obvious that nucleons (here: protons) are not elementary particles, but have a substructure[5]. At high-energy collisions the measured cross-section did not decrease as expected for an elastic scattering process. A close look at the momentum dependence of the so-called structure functions revealed the substructure of protons. Especially it could be shown, that the constituents

---

[2]**A T**oroidal **L**HC **A**pparatu**S**

[3]**C**ompact **M**uon **S**olenoid

[4]**A L**arge **I**on **C**ollider **E**xperiment

[5]First experiments have been carried out at SLAC. In 1990, Jerome I. Friedman, Henry W. Kendall and Richard E. Taylor were awarded the Nobel prize in physics for their studies on deep-inelastic scattering.
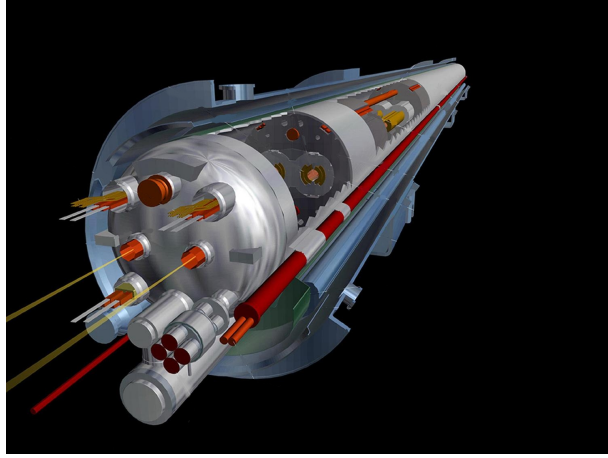
Figure 3.2: A 15 m long cryodipole of the LHC.

of a nucleon are spin $\frac{1}{2}$ particles[6]. A nucleon is composed of valence quarks (e.g. a proton's valence quarks are two *up*-quarks and one *down*-quark, which sums up to a total electric charge of $q = +1e$), but also of so-called sea-quarks and gluons which mediate the (self-)interaction of the constituents. Sea-quarks are quark-antiquark pairs created from the field established by the strong interaction of gluons within the nucleon. These virtual particles carry only a small fraction of the momentum of the nucleon.

A collision, i.e. the hard scattering process of two protons at sufficiently high energies can be described as interaction between two partons of the protons. As mentioned earlier (section 2.1.1), observable particles are colour-neutral. Hence, single quarks or gluons will hadronise. These particles interact with the gluon field and create new particles until a colour-neutral state is reached, i.e. a bound system is formed. Figure 3.3 illustrates this process.

3.3 Luminosity Measurement

The luminosity $\mathscr{L}$ is a basic quantity of a particle accelerator. The exact knowledge of the luminosity is crucial, because the measurement of the cross-section σ of physics processes depends on it:

$$\frac{dN}{dt} = \mathscr{L} \cdot \sigma \tag{3.1}$$

where dN/dt is the interaction rate. The luminosity depends on several machine parameters of the accelerator

---

[6]This is known as Callan-Gross relation [16].
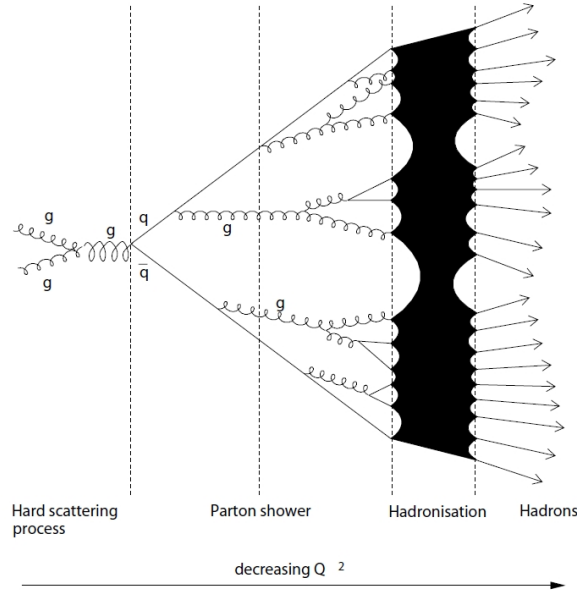
Figure 3.3: The hadronisation process. After the hard interaction, new and colour-neutral particles are created [17].

- n_1, n_2: the number of particles per bunch

- f: the revolution frequency

- σ_x, σ_y: the lateral dimension of the bunch

and is given as

$$\mathscr{L} = \frac{n_1 n_2 f}{4\pi \sigma_x \sigma_y} \tag{3.2}$$

The design luminosity of LHC is $\mathscr{L} = 10^{33}$ cm^{-2} s^{-1} at $\sqrt{s} = 14$ TeV. In the beginning LHC will run at $\mathscr{L} = 10^{32}$ cm^{-2} s^{-1} and $\sqrt{s} = 7$ TeV. There are two different methods to estimate the luminosity, either by an absolute measurement or by a relative measurement.

Relative luminosity measurement

The measurement of the luminosity which is proportional to the actual luminosity, apart from a constant, but unknown factor is called relative luminosity. A subdetector of the ATLAS detector called LUCID[7] will be used for this purpose. It consists of 40 Cherenkov tubes (filled with gas) surrounding the beam pipe

---

[7]**Lu**minosity measurement using **C**herenkov **I**ntegrating **D**etector
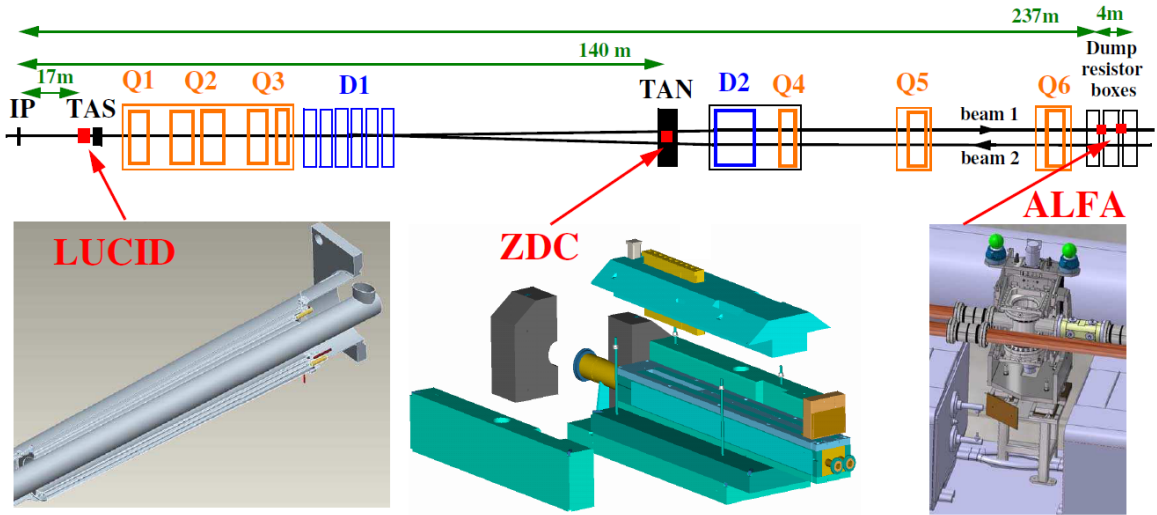
Figure 3.4: The main systems used for luminosity measurement at ATLAS are LUCID and ALFA. LUCID is next to the interaction point (IP), located beside the TAS (collimator). ALFA is the most remote luminosity detector. The system marked ZDC is mainly used for the detection of neutrons in forward direction. Detector elements marked with D or Q are magnets used for controlling the beam.

in a distance of 17 m from the interaction point attached to photomultipliers for the readout. The measurement of LUCID [18] is based on the principle that the number of interactions in a bunch crossing is proportional to the number of particles detected.

Absolute luminosity measurement

The measurement of the absolute luminosity basically means to determine the constant factor mentioned above. This is done by measuring the machine parameters or the investigation of elastic-scattering processes at small angles. The total cross-section is related to the imaginary part of the forward elastic scattering amplitude via the optical theorem[8], which allows a determination of the luminosity. The respective detector at ATLAS is called ALFA[9] [18]. To be able to measure the elastic pp-scattering at very small scattering angles, it is necessary to place the readout as near as possible to the beam. So-called Roman-pots are used, which consist of scintillating-fibre trackers that can be moved very closely to the beam. Unfortunately, these measurements can only be carried out under special

---

[8]$\Im F(0) = \frac{k}{4\pi}\sigma_t$, with $F(0)$ being the forward amplitude, k the wave number and σ_t the total cross-section. A detailed derivation of the optical theorem can be found in [19].

[9]**A**bsolute **L**uminosity **F**or **A**TLAS

preconditions, to be able to measure at very small scattering angles. This means, that special calibration runs of the LHC are necessary for a determination of the luminosity.

Chapter 4

The ATLAS Experiment

The ATLAS[1] detector is one of two multi-purpose particle detectors at the Large
Hadron Collider. More than 2000 scientists from all over the world work to-
gether in an effort to extend the understanding of nature. This chapter firstly
describes the construction of the ATLAS detector (figure 4.1). In the following
subsection 4.2 the trigger and data acquisition system and finally the computing
infrastructure (4.3) of this challenging experiment will be introduced.

4.1 The ATLAS Detector

At ATLAS two opposing, high-energetic proton beams will collide in the centre of
the detector, the so-called interaction point [20]. As a consequence, the products
of the collision will scatter in all directions. To reconstruct one event[2] full infor-
mation of everything which happens inside the detector is needed. This involves
the reconstruction of the properties of the collision products, e.g. the momenta,
energy and charge. This is done through the combination of measurements of all
subdetectors which will be described in the following subchapters [21].

4.1.1 Magnet System

The magnet system is an important part of a modern particle detector. According
to the Lorentz force

$$\vec{F} = q(\vec{E} + \vec{v} \times \vec{B})$$

the trajectory of a charged particle q with velocity $\vec{v}$ is bent circular under
the influence of a magnetic field $\vec{B}$. From the radius of the circle it is possible to
reconstruct the momentum of a particle.

---

[1]A Toroidal LHC ApparatuS

[2]An *event* describes the whole process starting with the collision of two protons and the
propagation and decay of the products of the collision through the detector.
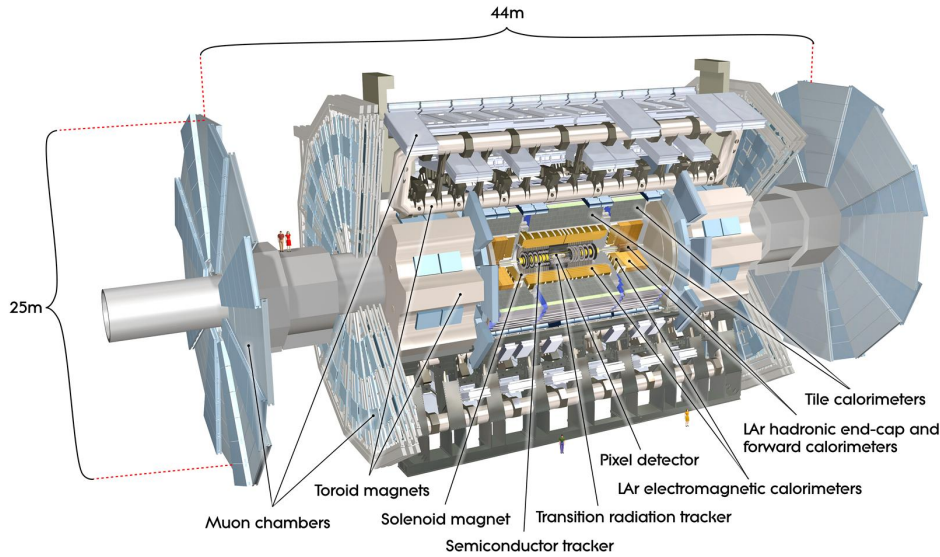
Figure 4.1: Computer generated image of the whole ATLAS detector.

The ATLAS detector uses two different magnetic fields, the Inner Detector (to be described in the next subchapter) is surrounded by a solenoidal magnetic field, the so-called central solenoid, while the Muon Spectrometer lies within a huge toroidal magnetic field (barrel toroid) . The properties of the magnet system will be described in the following.

A solenoid [22] is a three-dimensional coil; the electric current produces a uniform magnetic field inside the volume. Inhomogeneities which influence the measurement arise due to the fact that the coil is shorter than the Inner Detector. The solenoid field is aligned on the beam axis; the strength of the axial magnetic field is 2 T [23]. The material of the solenoid is minimised with respect to the interaction length the particles have to traverse ($0.66X_0$ [3]). This is achieved by a shared vacuum vessel of the solenoid windings and the liquid argon calorimeter (see chapter 4.1.3). The inner diameter of the solenoid is 2.46 m and the outer diameter is 2.56 m, while the axial length is 5.8 m. The cold mass weighs 5.4 t and the coils are operated at a nominal current of 7.73 kA producing a magnet stored energy of 0.04 GJ. The peak field strength is 2.6 T. This is achieved through superconducting NbTi [4] (supported by aluminium and copper) magnets with the cold mass being cooled down to 4.5 K.

The toroidal magnetic field is created through eight coils in the barrel region

---

[3] X_0 is the radiation length. It is a characteristic of a material which describes the energy loss of electromagnetic particles through interaction with it.

[4] NbTi is an alloy of niobium and titanium and used as superconductor.
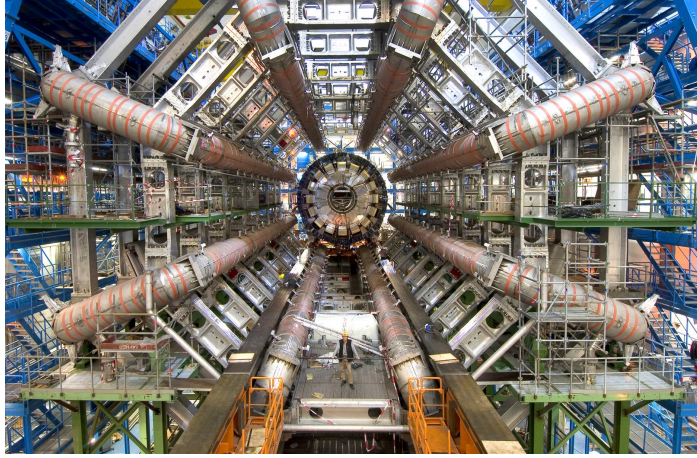
Figure 4.2: The eight toroid magnets of the ATLAS detector can be seen surrounding the calorimeter which is in the centre of the detector (during installation).

(shown in figure 4.2) of the detector [24] and the two end-cap toroids [25]. The magnetic field created by the coils is circular with respect to the beam axis. It has been designed to help reconstructing the muons on a standalone base within a huge field volume of $\approx$ 7000 m^3 and down to a forward angle of $\approx$ 8°. The support structure occupies only $\approx$ 2% of the volume. The barrel toroid coils have an inner diameter of 9.4 m and an outer diameter of 20.1 m, with an axial length of 25.3 m. The cold mass weighs 370 t and the coils are operated at a nominal current of 20.5 kA. The energy stored within the magnet is 1.08 GJ, leading to a peak field strength of 3.9 T. It is important to stress that the coils are not surrounded by iron (to increase the magnetic field strength), but air (to minimize scattering of the particles).

4.1.2 Inner Detector

The ATLAS detector [21] in general consists of several layers, like an onion. The innermost layer is the Inner Detector (ID). The shape of the Inner Detector is cylindrical and it is contained within the solenoidal magnetic field. The ID is a system of pixel- and silicon microstrip (SCT) detectors and transition radiation trackers (TRT) which covers the pseudorapidity [5] range $|\eta| < 2.5$, see figure 4.3. The ID components are exposed to huge radiation doses, therefore the radiation hardness was a main point in the development, for example the inner layer of the pixel detector is planned to be replaced after three years of operation.

---

[5]The pseudorapidity is a quantity, that is related to the direction of a particle in a plane perpendicular to the x-y plane (expressed through θ). It is defined as $\eta = -\log(\tan(\frac{\theta}{2}))$. The ATLAS coordinate-system is right-handed, the positive x-direction points to the centre of the LHC ring and the z-axis into the beam direction.
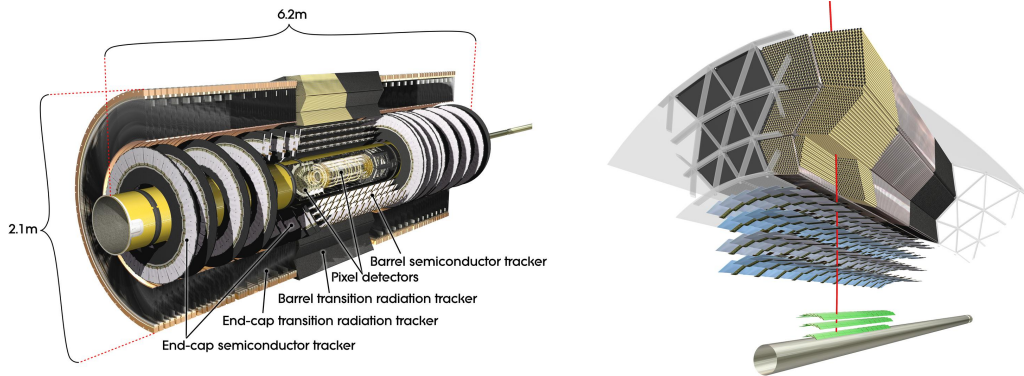
Figure 4.3: The Inner Detector of the ATLAS detector. It consists of three different systems, the pixel detector, SCT and TRT. Each of the systems consists of several layers.

The properties of these components of the ID will be discussed in the following paragraph.

The pixel detector

The pixel detector [26] consists of 80 million readout channels distributed over three layers and the barrel region. Being the innermost part of the detector it is important for secondary vertex reconstruction and for the b-tagging of jets. Furthermore it has a high spatial resolution for the reconstruction of primary vertices. The pixel detector should measure at least three points of the track of a charged particle. The pixel detector consists of silicon sensors (wafers), shown in figure 4.4, where one pixel has a size of $50 \times 400\ \mu\mathrm{m}^2$. One module contains ≈ 46000 pixel channels and each channel is build of ≈ 1000 transistors. The pixel sensor can be described as solid-state ionisation chamber. Particles passing the wafer produce electron hole pairs and through application of an electric potential the electrons and holes drift to opposite sides of the pixel detector. The detection efficiency has been measured as 99.9% for unradiated modules and decreases by $\approx 2.5\%$ for irradiated modules.

The semiconductor tracker

The semiconductor tracker (SCT)[27] also uses semiconductor technology for detection and precise reconstruction of space-time coordinates of charged particles. The SCT consists of ≈ 15000 single-sided p-in-n sensors in the barrel and the end-cap region, fig. 4.4. As the SCT is a semiconductor sensor, the same effects as described for the pixel detector applies: the sensors are exposed to a high radiation dose, which causes a type inversion from initially n-type to p-doped
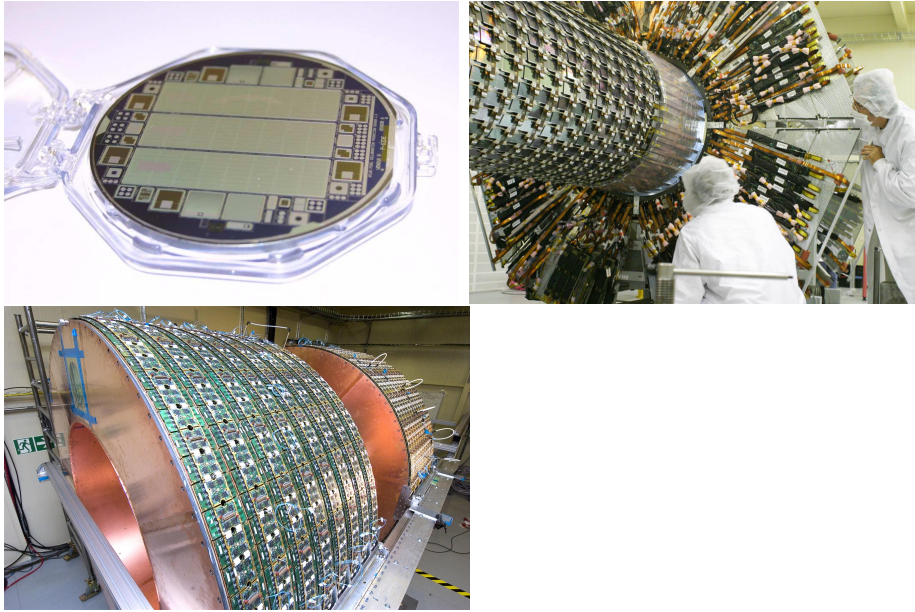
Figure 4.4: A pixel sensor wafer and the barrel of the semiconductor tracker.

after some time. To reduce the detector material the thickness of the silicon sensors is 285μm. For high precision in the resolution, pattern recognition and occupancy a strip pitch of 80μm with a rotation angle of 40 mrad between the sensors on each side of the module has been chosen. The design of the end-cap sensors is slightly different because of the disk layout of the end-cap; the pitch is not constant because of the wedge-shaped geometry. Each sensor consists of 768 readout strips.

The transition radiation tracker

The third component of the ID are the straw tubes which build the transition radiation tracker (TRT). The straw tubes are proportional drift tubes. The barrel part[28] of the TRT consists of ≈ 50000 straws of 144 cm length which are aligned parallel to the beam axis. The two end-caps[29] are comprised of ≈ 120000 straws (of length 37 cm) each and aligned radially. A particle crosses 35-40 straws which allows constant tracking through the ID. The tubes have a diameter of 4 mm which is a trade-off between high hit efficiency and speed of response (the event rate is 40 MHz). Another reason for the use of straw tubes is the relatively low cost compared to semiconductor modules. The straws are embedded in polypropylene/polyethylene fibres which produce the transition radiation. The straw anodes are made of gold-plated tungsten wires (diameter 30μm) and located in the middle of the tube. The straws are filled with a gas mixture of 70% Xe, 27% CO_2 and 3% O_2. Particles traversing a tube cause
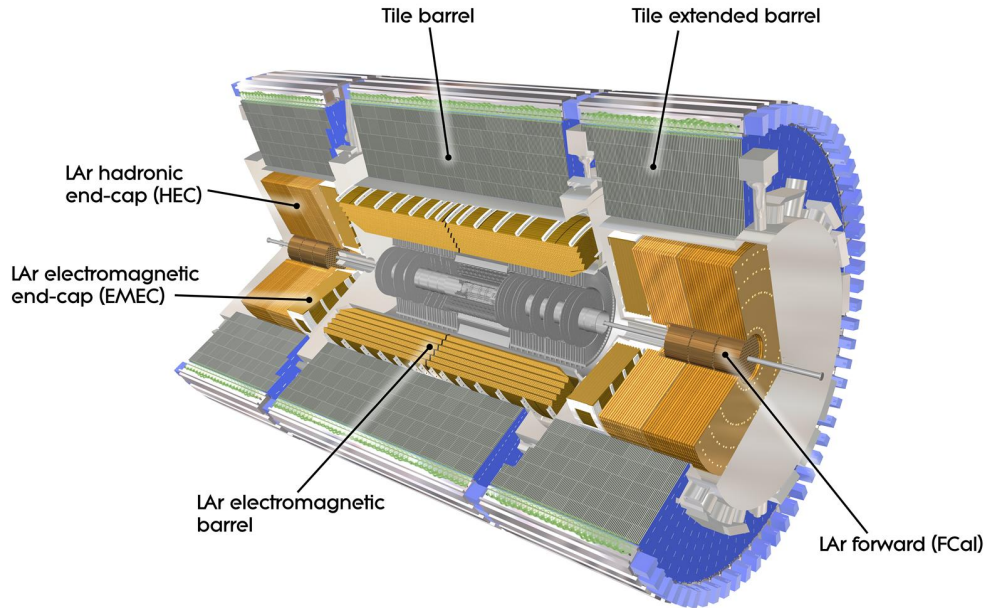
Figure 4.5: Cut-away view of the ATLAS calorimeter system.

ionisation of the gas.

4.1.3   The Calorimetry System

Calorimeters represent a substantial part of a particle detector. They measure the energy of particles through absorption of their energy. The special construction also allows the determination of the position of the particles. Precise energy measurement requires the electromagnetic and hadronic showers produced by the particles to be contained within the respective calorimeter. Additionally, a punch-through into the muon system must be inhibited.

There are two different types of calorimeters at ATLAS [20] which will be described below: the electromagnetic calorimeter and the hadronic calorimeter. Both are cylindric and aligned with the beam axis. The hadronic calorimeter envelopes the electromagnetic calorimeter which itself envelopes the Inner Detector, as shown in figure 4.5. The purpose of an EM calorimeter is the energy measurement of particles which interact primarily through electromagnetic interaction (electrons and photons), while the hadronic calorimeter measures the energy of particles which interact through the strong force (quarks and gluons).
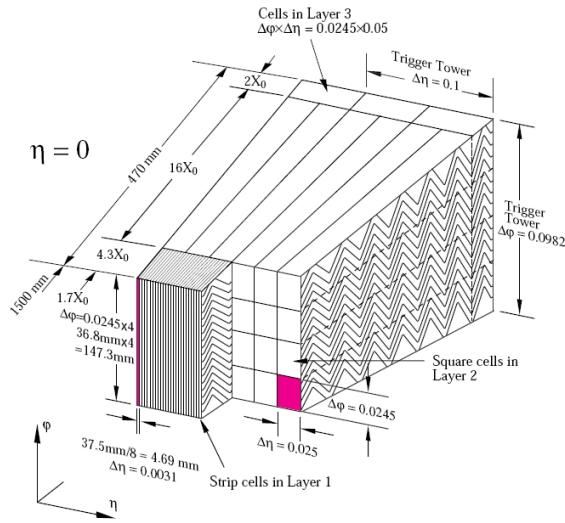
Figure 4.6: The barrel module of the electromagnetic calorimeter. The accordion structure of the different layers is clearly visible.

The Electromagnetic Calorimeter

The electromagnetic (EM) calorimeter consists of three parts: a barrel region and two end-cap modules. This covers a pseudorapidity range of $|\eta| < 3.2$. The barrel consists of two half-barrels, one weighs 57 t and has inner and outer diameters of 2.8 m and 4 m respectively; the length of one barrel is 3.2 m.

The barrel of the EM calorimeter and the solenoid share one vacuum vessel, in order to minimise detector material. The cryostats in the endcap contain not only the EM endcap calorimeter, but also the hadronic endcap calorimeter and the forward calorimeter. The EM calorimeter itself is a lead-LAr [6] calorimeter with accordion-shaped electrodes and lead absorber plates, fig. 4.6. LAr is used as active medium. The accordion geometry has full ϕ symmetry and avoids azimuthal cracks, which leads to a very uniform performance in terms of linearity and resolution as a function of ϕ. The thickness of the EM calorimeter is at least 22 radiation lengths. In the central region where $|\eta| < 1.8$ a presampler detector (which consists of an active LAr layer) is used to correct for energy loss.

The Hadronic Calorimeter

Following the electromagnetic calorimeter the next detector layer is the hadronic calorimeter. It consists of several subdetectors, which will be described below.

---

[6]LAr = liquid Argon. Argon ($\alpha\rho\gamma o\nu$) is an extremely inert noble gas. Liquid argon has a linear behaviour and by being inert liquid argon has a high radiation-hardness.
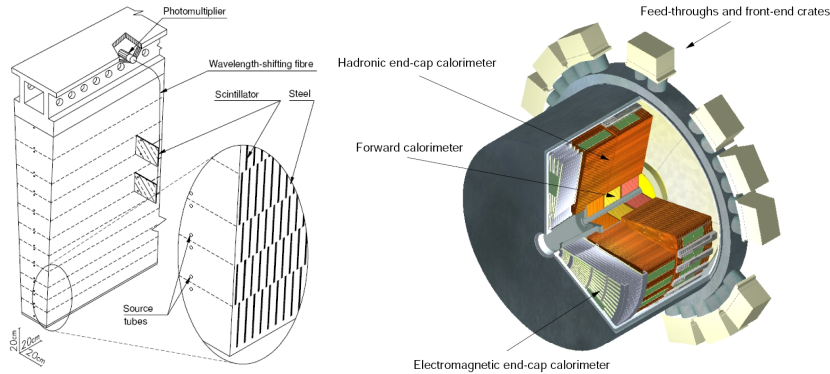
Figure 4.7: The structure of the hadronic calorimeter. Each wedge shaped module consists of the tile calorimeter and the read-out electronics. There are 64 modules. The sketch on the right side illustrates the layout of the endcap calorimeter.

Tile calorimeter The barrel part of the hadronic calorimeter consists of a central barrel ($|\eta| < 1.0$) and two extended barrels ($0.8 < |\eta| < 1.7$). Like the EM calorimeter it uses the sampling technique, but with steel as absorber and scintillating tiles as the active material. The steel-scintillator volume-ratio is roughly 4.7 : 1. The signals are read-out via photomultipliers which receive the signal of the scintillators through wavelength-shifting fibres, see figure 4.7.

The tile calorimeter has inner and outer radii of 2.28 m and 4.25 m, respectively. It is divided into three layers radially from the inside to the outside, which have a thickness of roughly $1.5, 4.1$ and 1.8 interaction lengths in the barrel region. The interaction lengths of the extended barrel region are $1.5, 2.6$ and 3.3λ. The total thickness of the tile calorimeter is 9.7λ at $\eta = 0$.

LAr hadronic endcap calorimeter (HEC)   This part of the endcap calorimeter consists of two wheels, behind the electromagnetic calorimeter. To reduce the drop in material parts of the different subdetectors overlap. The HEC shares the LAr cryostats with the EM endcap calorimeter and the forward calorimeter, see figure 4.7. The wheels are made of copper plates filled with LAr gaps as active medium. The discoidal HEC covers the range $1.5 < |\eta| < 3.2$.

LAr forward calorimeter (FCal) This subdetector is integrated into the endcap cryostats and consists of three different layers to enable the measurement of electromagnetic as well as hadronic interactions. The innermost layer is made of a copper matrix and the two outer layers are made of tungsten. In between the layers LAr is used as the active medium. The FCal reaches up to $|\eta| < 4.9$ in order to provide a maximum envelope to measure all particles traversing the
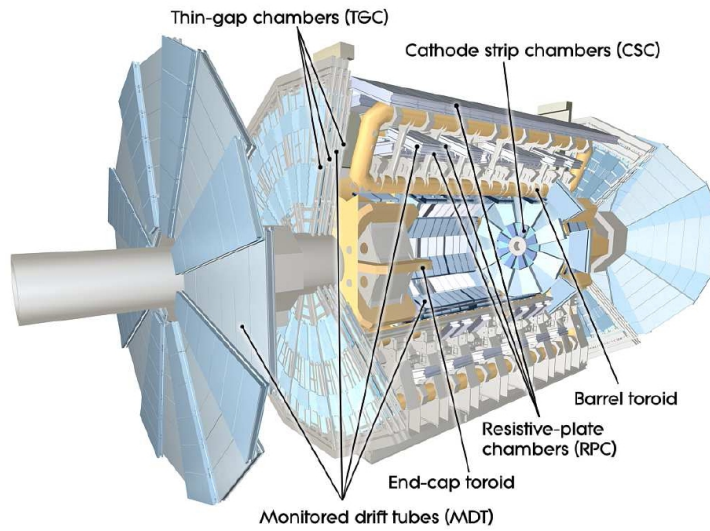
Figure 4.8: The different parts of the ATLAS muon system are shown.

detector after the collision.

4.1.4 Muon Spectrometer

The muon system is the outermost and largest subdetector of ATLAS. Muons are the only particles (besides the weakly interacting neutrinos) which reach the muon detector of ATLAS. Other particles either get absorbed by the calorimeters or can not reach the muon system because of their low momentum, which leads to small spiral trajectories in the toroidal magnetic field. The magnetic field is created by three large superconducting air-core toroids, one barrel toroid and two endcap toroids. They consist of eight coils each and are located in a symmetrical manner around the beam axis.

The bending of the muon trajectories depends on the magnetic field strength and the lever between the inner and outer muon chamber. The bending power is 1.5 to 5.5 Tm in the central region ($|\eta| < 1.4$) and 1 to 7.5 Tm in the endcap region ($1.6 < |\eta| < 2.7$).

Figure 4.8 shows the layout of the muon system. Subdetectors are arranged in three layers, both in the barrel and the endcap region. In the central region the muon chambers are located at radii of 5 m, 7.5 m and 10 m. In the endcap regions the muon chambers form large wheels at distances of 7.4 m, 10.8 m, 14 m and 21.5 m from the interaction point (measured along the beam axis). The track of a particle gets measured within each layer. A big advantage is the large lever arm that allows the reconstruction of a very precise track over a high momentum range and consequently a very good resolution.

The subsystems are: Monitored Drift Tubes (MDT) for tracking and Resistive
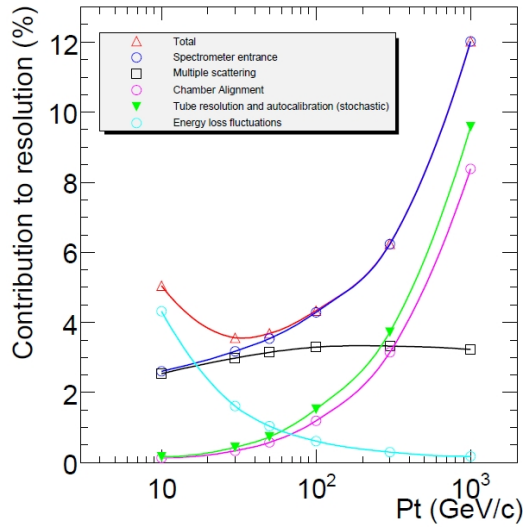
Figure 4.9: The momentum resolution as a function of transverse momentum (for $|\eta| <$ 1.5) and the respective contributions to the resolution [10].

Plate Chambers (RPC) for triggering in the barrel region and Cathode Strip Chambers (CSC) for tracking and Thin Gap Chambers (TGC) for triggering in the endcap region. The components of the muon spectrometer are described below.

Monitored Drift Tubes (MDT)
The MDTs are drift tubes made of aluminium with a diameter of approximately 30 mm. They are filled with a 93:7 mixture of Ar:CO_2 at 3 bar[7]. Traversing muons ionise the gas mixture and create electrons which drift to the tungsten-rhenium wire in the middle of the tube. These wires are at a potential of 3080 V which leads to an avalanche effect and a measurable signal. The position of the muon track can then be reconstructed through a r-t-relation. Throughout ATLAS different sizes of MDT chambers are used, but the basic design is identical: they are arranged in layers of three or four drift tube layers which build a so-called multilayer. A MDT chamber consists of two multilayers. The large dimensions of the muon spectrometer requires precise alignment of the chambers. This is done through an optical alignment system.

Cathode Strip Chambers (CSC)
Due to the high rate in the forward region ($|\eta| > 2$, $z = 7$ m) of the detector the

---

[7]ArCO$_2$ was chosen because of its good ageing properties, which leads to no deposits on the wires. A disadvantage is the high drift time, this could lead to problems after a high luminosity upgrade of LHC.

MDT chambers are replaced by the cathode strip chambers. They work reliable up to rates of 1000 Hz and provide a high spatial and time resolution. The system consists of two discs and each of the discs contains four layers. This yields four η-ϕ measurements.

The CSC are multiwire proportional chambers with cathodes segmented into strips which build the inner layer at large pseudorapidities. They have a higher granularity to cope with the large rate and radiation. The track is reconstructed by measuring the charge on adjacent cathode strips. The CSCs reach a resolution of 60 μm.

Resistive Plate Chambers (RPC)
The trigger system in the central region consists of three layers of RPCs. A large lever arm between the inner and outer RPC allows the triggering of high-p_T muons. The rather simple layout does not contain wires but two parallel electrode-plates. These plates are made of a plastic laminate and contain a gas mixture. The electric field of approximately 4.9 kV/mm produces avalanches of ionised particles to the electrodes. On the back of the plates readout strips are applied in a 2-dimensional scheme. This allows the determination of coordinates in η and ϕ direction.

Thin Gap Chambers (TGC)
The TGC are used as trigger in the endcap muon spectrometer. A TGC is a multi-wire proportional chamber that consists of two parallel, graphite coated cathode layers at a distance of 2.8 mm. A plane of anode wires is located in between the plates. The volume is filled with a mixture of CO_2 and n-C_5H_{12}. Through a high electric field and a small wire-to-wire distance a good time resolution is possible.

One of the main features of the ATLAS muon spectrometer is the reconstruction resolution performance. The muon spectrometer has a resolution of $\approx 10\%$ at 1 TeV. Measurements over the full momentum range from 3 GeV to 3 TeV are accessible. Figure 4.9 shows the contribution to the momentum resolution for muons reconstructed in the Muon Spectrometer.

The performance goals of the subdetectors of the ATLAS detector are summarised in table 4.1.

4.2 Trigger and Data Acquisition

In LHC protons will circulate with a frequency of 40 MHz. Each collision of two proton bunches produces approximately 23 (at the design luminosity of $\mathscr{L} = 10^{33}$ cm^{-2} s^{-1}) simultaneous interactions additionally to a signal event which leads to a rate of ≈ 1 GHz. It is impossible to store every event (one reconstructed event has a size of ≈ 1.5 MB), hence the amount of physics data needs to be reduced. This is done through so-called triggers, which have to identify interesting physics

Detector component	Required resolution	η coverage	
		Measurement	Trigger
Tracking	$\sigma_{p_T}/p_T = 0.05\% p_T \oplus 1\%$	± 2.5	
Calorimetry	$\sigma_E/E = 10\%/\sqrt{E} \oplus 0.7\%$	± 3.2	± 2.5
Hadronic calorimetry (jets)			
barrel- and end-cap	$\sigma_E/E = 50\%/\sqrt{E} \oplus 3\%$	± 3.2	± 3.2
forward	$\sigma_E = 100\%/\sqrt{E} \oplus 10\%$	$3.1 < |\eta| < 4.9$	$3.1 < |\eta| < 4.9$
Muon spectrometer	$\sigma_{p_T}/p_T = 10\%$ at $p_T = 1$ TeV	± 2.7	± 2.4

Table 4.1: The performance goals of the ATLAS detector [21].

events and reduce the event rate by five orders of magnitude. Many interesting events occur at rates of less than 1 Hz which clearly illustrates the need for reliable triggers.

4.2.1   The Trigger System at ATLAS

The trigger system consists of three stages which are based on the definition and evaluation of Regions of Interest (RoI). The trigger sequence which is illustrated in figure 4.10 will be described below.

The Level 1 Trigger
The first level trigger (L1) purely relies on hardware. Custom made electronics is used to quickly discriminate event rates from 40 MHz to 75 kHz, at a latency of 2.5μs. The classification of an event depends on the information of the calorimeter and the muon system, both with reduced granularity to save storage space. The L1 muon system uses information of the RPCs and the TGCs (described in chapter 5.1.2) while the calorimeter evaluates so-called trigger-towers in $\Delta\eta - \Delta\phi$-regions of the electromagnetic and the hadronic calorimeters. For events that do not get rejected, the L1 trigger defines the geometrical RoI with possibly interesting signatures, e.g. muons above a transverse-momentum threshold. Information on events which qualify for further investigation are moved to computing farms near the ATLAS cavern, where the next trigger levels based on software algorithms are executed.

The Level 2 Trigger
The Level 2 trigger (L2) reduces the event rate from 75 kHz to 1 kHz and has a time window of 40 ms for a decision. The L2 trigger belongs to the software based triggers (combined as High Level Trigger, HLT). It uses the seed information (RoI) of the L1 trigger and has access to all of the information within the RoI and makes its decision before the full event has been built. The meanwhile
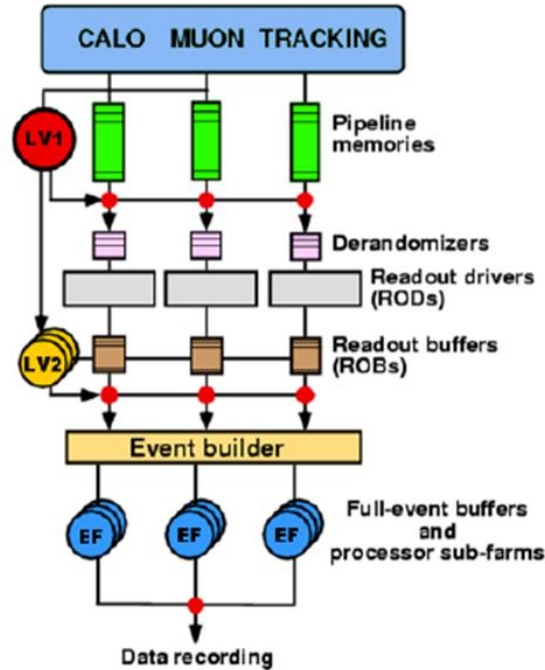
Figure 4.10: The structure of the trigger system at ATLAS.

buffered event information is then passed on to the Event Filter. An event that failed L1 can not be detected in the subsequent trigger levels.

The EventFilter
The final step of the trigger system is the Event Filter (EF), which reduces the event rate from 1 kHz to 200 Hz. The EF is also software based and examines the full event (the buffered information is collected by the Event Builder). Events that pass the EF get stored and distributed within the computing grid for analyses after a full offline reconstruction of the event. The decision time of the EF is ≈ 4 s and the write-rate is expected to be 300 MB/s, leading to an annual storage requirement of $\approx$ 1 PB. The computing framework which is needed to cope with such large data rates and computing power will be introduced in chapter 4.3. The main difference between L2 and EF is the use of more sophisticated reconstruction algorithms because of the longer latency time. A trigger menu is formed by logical combinations of several trigger items, like number of leptons or jets.

4.3   ATLAS Computing

The first sections of this chapter have been dedicated to the ATLAS detector and the data acquisition. From the scale of the detector and the manpower involved it becomes clear that extraordinary methods for dealing with the storage, distribution and analysis of the data are necessary. The data used for physics analyses is either Monte Carlo-simulated data (section 4.3.1) or real data collected by the detector itself. Both, real and simulated data need to be processed in order to provide a common, yet flexible interface. The necessary steps performed within the general computing framework of ATLAS will be discussed in section 4.3.2. As indicated by the discussion on triggers, this experiment is unthinkable without huge computing capacities. The approach to cope with this challenge will be introduced in section 4.3.3 of this chapter.

4.3.1   Monte Carlo Simulation and Generators

The Monte Carlo (MC) technique is a stochastic method, that helps to understand processes through repeatedly executed random experiments.[8] It is a common tool in High Energy Physics, but also in other areas of science, like meteorology and even risk management. In particle physics it is used to simulate physics processes like the collision of high-energetic protons.

Physics processes usually have many degrees of freedom, each represents a possible outcome of a random experiment, e.g. the probabilities of the decay of particles like the Higgs-boson into W bosons and leptons. The description of this process is based on the random choice of possibilities which are defined through a so-called probability density function (PDF).

MC methods are not only used to describe physics events itself, but also the simulation of the detector response, i.e. the propagation of the remnants through the detector. At ATLAS this is done through an implementation which is called GEANT; the details of this procedure will be described in section 4.3.2.

There exist many different implementations of the MC method to simulate physics events. Some of them are multi-purpose generators, others are tuned to describe special types of interactions with high precision. It should be stressed, that Monte Carlo results should be interpreted with care. Generated events are unable to mimic reality, it is always an approximation with different precision. MC generators used throughout this analysis are introduced briefly below.

MC@NLO
For a reliable prediction of physics processes and cross-sections a precise description of these processes is necessary. This is usually done to next-to-leading order

---

[8]The Monte Carlo method has been developed by N. Metropolis and S. Ulam[30] and was used firstly by physicists of the Los Alamos laboratory working on the Manhattan project.

accuracy[9]. MC@NLO [31] calculates matrix elements for the scattering process, but only the so-called hard interaction of two protons. Therefore the showering and hadronisation of the collision must be calculated externally. This is done through HERWIG or JIMMY, which can be interfaced through the Les Houches interface [32]. The MC@NLO generator has been used for the simulation of the signal events, as well as for some of the background events. This will be described later in more detail.

Herwig/Jimmy

HERWIG [33, 34] is a Monte Carlo package for simulating hadron emission reactions with interfering gluons and can be seen as multi-purpose generator, based on leading-order calculations. At ATLAS JIMMY [35] generates multiple parton scattering events in hadron-hadron events. JIMMY is a library used in addition to HERWIG.

Alpgen

ALPGEN [36, 37, 38] is another Monte Carlo generator used for the simulation of multiparton hard processes. It can calculate the exact matrix elements for many parton-level processes to be studied at ATLAS. Like MC@NLO it needs to be interfaced with another generator as HERWIG for the simulation of the hadronisation process.

AcerMC

ACERMC [39] is a generator used for the simulation of standard model background processes at the LHC. Again, ACERMC only generates the hard interaction, the hadronisation needs to be done externally, e.g. with HERWIG.

Pythia

PYTHIA [40] is a leading order multi-purpose Monte Carlo generator. PYTHIA offers many different physics processes but mostly in lowest nontrivial order, without multijets and effects like spin correlation.

4.3.2 Athena – The ATLAS Computing Framework

The data acquisition process of the ATLAS detector has already been described (chapter 4.2). The reconstruction and analysis of this data – as well as the simulated data – is done within a large computing framework called ATHENA[41]. It is a highly modularised software environment, based on the Gaudi framework [42, 43]. This approach allows on one hand to work independently on separate

---

[9]Perturbation theory is the method of choice for the calculation of these processes. The calculation comprises a power series and the leading term is called leading-order. The first correction term is called next-to-leading order.

modules and on the other hand access to all modules through a single gateway, called STOREGATE. A user uses the algorithms of the separate parts of the software through one single access point.

ATHENA is mainly used for the reconstruction of data recorded with the AT-LAS detector, in case of Monte Carlo simulated events it also provides algorithms for the generation, simulation and digitisation of these events, illustrated in figure 4.11. This will be described in more detail below.

Simulation and Reconstruction

The event generation using a particular Monte Carlo generator has been described above. The events are stored in a generic data format which is called HepMC.

The second step simulates the propagation of the hadronised particles through the detector by using the GEANT4 package [44]. This toolkit offers a large variety of processes like electromagnetic or hadronic interaction featuring a full description of the detector geometry, different materials and the tracking of these particles exposed to a magnetic field. All of the information gathered in this step is stored in so called G4 Hits for the next step, the digitization.

Now the passage of particles has been calculated, but to be able to reconstruct the event, the detector response needed. This is achieved in the digitization step: hits in subdetectors, energy deposition in calorimeters or drift times are calculated. The outcome of the digitization is stored in G4 Digits objects which resemble real data that has been measured with the detector.

The reconstruction step applies equally for both, Monte Carlo and real events. Starting with the information on the detector response, Athena reconstructs the event, including the matching of tracks or the identification of leptons or jets. The identification of the objects is determined through algorithms and the interaction of the particles with each of the subdetectors. The output of the reconstruction is stored as Event Summary Data (ESD) and as Analysis Object Data (AOD). The ESD contains more information about the events (mainly needed for validation), but for analyses the AOD is better suited. It contains a reduced amount of data which is sufficient for most analyses.

The production of one Monte Carlo event and the subsequent process of simulation, digitization and reconstruction takes approximately 10-20 minutes, depending on the complexity of the event, on a modern CPU. Taking into account the huge production cross sections of physics processes at ATLAS, it becomes clear, that only massive capacities of computing power can cope with this enormous challenge. For the production of Monte Carlo events, as well as for the distribution of the data globally connected computing centres are used. This is called the Grid and will be described in more detail in chapter 4.3.3.

AODs contain a lot of information, usually more than needed for a physics analysis. Hence it is useful to create small files containing only relevant infor-
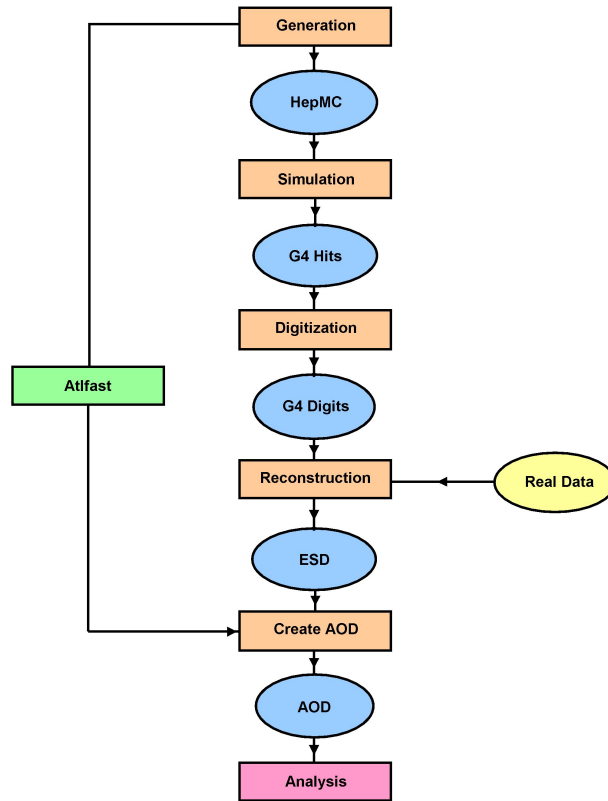
Figure 4.11: Simulation of physics events using the full chain of the ATLAS software framework Athena.

mation. These files are called N-tuples and are analysed using the data analysis framework ROOT [45]. The write-out of selected events ("dumping") is done using EventView [46], which will be described in more detail in chapter 5.

Atlfast

As stated earlier, the production of a fully simulated Monte Carlo event lasts 10-20 minutes, depending on the CPU. Large quantities of data are produced using a so-called fast detector simulation. The software is called ATLFAST [47] and uses a parametrised description of the ATLAS detector response. The input from the Monte Carlo generators is smeared according to the expected detector response and resolution. The output format is AOD and by skipping the different steps in between (detector simulation and reconstruction) the computing time for one event improves by several orders of magnitude.

To be able to study large cross-section processes in more detail, ATLFAST
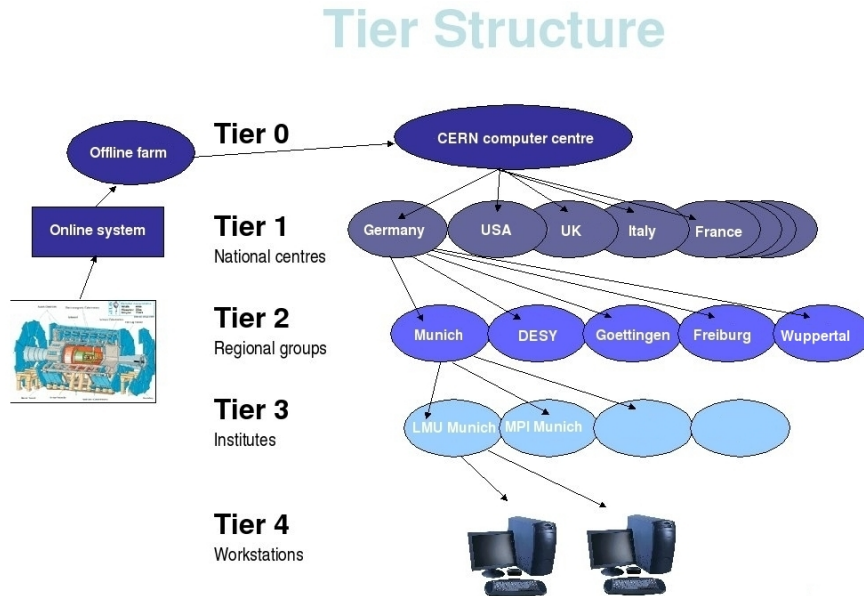
Figure 4.12: This sketch illustrates the structure of the Grid as used with ATLAS.

II has been developed. It uses partially parametrised detector description and partially the standard reconstruction also used with full simulation. To be more specific, the inner detector is fully simulated, while the calorimeters use a fast calorimeter simulation. The muon system can either be simulated fully or using a parameterisation.

4.3.3 Grid Computing

With ATLAS being a worldwide collaboration, a global distribution of regional computing centres has been chosen. At CERN consequently only the first processing and distribution of data is done (this is also referred to as Tier-0), thereafter the data gets distributed to regional computing facilities, called Tier-1 centres, which are responsible for the storage and reprocessing of data. Furthermore, smaller Tier-2 centres will be used as facilities for physics analyses and storage of data, while small Tier-3 facilities are used only for analysis purposes. Figure 4.12 illustrates the structure of the Grid as it is used at ATLAS. A defining characteristic of Grid computing is the policy which requires that the analysis jobs are sent to the data, not vice versa. This is far more efficient, because no computing centre (except Tier-0) has a copy of all data. That way no further file transfers are necessary. A more detailed introduction into distributed computing at the ATLAS experiment is given in Appendix A.

Chapter 5

Physics Objects and Event Selection

5.1 Analysis Object Data

The Athena software framework has been introduced in chapter 4.3.2. The reconstructed particles get stored in so-called containers, thus enabling simple access to all physics objects stored in the AOD through keys. These objects and the reconstruction will be explained below, with a focus on particles relevant to this study.

5.1.1 Electrons

The reconstruction of electrons relies on the response of the electromagnetic calorimeter and on a track measurement in the Inner Detector. Offline reconstruction uses two different algorithms, one is dedicated to electrons with high transverse momenta and based on a seeded cluster in the calorimeter. The second one is better suited for electrons with lower transverse momenta (a few GeV) and is seeded by a track in the Inner detector. The cluster based algorithm is the standard and used for this study. For the identification of electromagnetic clusters, a so-called sliding-window algorithm is used [48], where a fixed size window maximises the energy deposited within a cluster. The matching of a track and a cluster is done trough a comparison of the η and ϕ regions and a subsequent extrapolation of the track to the calorimeter entries.

5.1.2 Muons

Muons are heavier, thus the bremsstrahlung probability is largely reduced. Muons do not produce showers in the calorimeters, but leave tracks in every subdetector. Other particles (beside neutrinos) do not reach the Muon Spectrometer. Therefore the identification of particles as muons is rather simple, nonetheless the

reconstruction of the muon properties is not. Athena provides two standalone algorithms for the reconstruction. Both form track segments in different parts of the Muon Spectrometer and then build tracks through combination.

For this analysis the STACO algorithm [49] has been chosen. This technique uses the statistical combination of two independent track measurements – one from the Inner Detector and one from the Muon Spectrometer. The track measurements in the Inner Detector are reconstructed by the xKalman package [50]. The reconstruction done by xKalman either extends over the full Inner Detector or focuses on a Region of Interest (defined by a jet or lepton). Primary tracks give possible trajectories for track candidates which are then extrapolated to the precision tracker. The clusters are compared and if enough clusters were hit uniquely, the track is kept.

The track measurements in the Muon Spectrometer are done using the Muonboy algorithm [49]. Muonboy accounts for energy loss corrections in the calorimeters using a momentum dependent parameterisation. The tracks can be described through parameter vectors P_i and covariance matrices C_i. The combined track can then be described by the parameter vector

$$\left(C_1^{-1} + C_2^{-1}\right) \times P = C_1^{-1} \times P_1 + C_2^{-1} \times P_2 \tag{5.1}$$

and the covariance matrix

$$C = \left(C_1^{-1} + C_2^{-1}\right)^{-1} \tag{5.2}$$

The combination is done using a χ^2 matching:

$$\chi^2 = (P - P_1)^T \times C_1^{-1} \times (P - P_1) + (P - P_2)^T \times C_2^{-1} \times (P - P_2) \tag{5.3}$$

The covariance matrices also treat multiple scattering and energy loss fluctuations. After combination the track is propagated to the beam line, where multiple scattering in the Inner Detector is included.

5.1.3 Jets

Several approaches for an optimal reconstruction of jets have been implemented into ATLAS. The classical approach relies on a fixed cone algorithm. Others follow a sequential recombination, e.g. the k_T algorithm [51]. For this analysis a fixed cone jet algorithm [52] has been chosen and will be described briefly. Initially, all input gets sorted in terms of decreasing transverse momentum. Given the object with the highest momentum is above a seed value, all objects within a cone range in η and ϕ (figure 5.1) are combined with the seed to a jet

$$\Delta R = \sqrt{\Delta \eta^2 + \Delta \phi^2} < R_{cone}$$

After including all objects within the cone, a new direction of the jet is calculated. This process is repeated for all objects above the seed value to find all jets of the event.
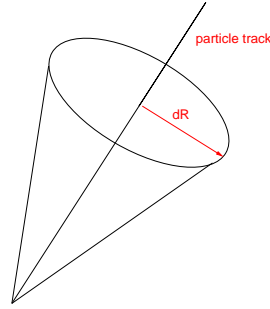
Figure 5.1: Illustration of dR, the radius of a cone around a particle track.

5.1.4   Missing Transverse Energy

Missing transverse energy comprises all fractions of energy which could not be reconstructed by the detector. Due to energy conservation it can be calculated from the centre-of-mass energy of the collision and the vector sum of the calorimeter energies projected onto the transverse plane. The missing transverse energy includes the energy of the weakly interacting neutrinos which escape the detector and detector effects like limited coverage, resolution, dead regions and noise. As mentioned above, muons do not deposit energy in the calorimeters, which is taken into account by the algorithm. The correction for those errors as well as the details on the reconstruction algorithms for the missing transverse energy can be found in [10].

5.2   Event View

The analysis objects ESD and AOD contain much more information than needed for most analyses. This leads to large files and reduces the speed of processing. Hence, tools have been developed to overcome this problem by writing out only relevant objects and variables into a new file. The data can then be analysed using the ROOT framework [45] much quicker.

A software framework suited for this is called EVENTVIEW [46].

With EVENTVIEW it is possible to choose cuts for the preselection of events. It can also be used to remove an overlap between particles that have been reconstructed several times, e.g. as electron and as jet.

There are several implementations of EventView, each aims at typical analyses by a predefined set of cuts, e.g. SUSYVIEW contains variables typically used for SUSY searches. For this thesis HIGHPTVIEW has been used, which is suited for analyses using objects with high transverse momentum. The following cuts have been applied in HIGHPTVIEW. Electrons must pass

- *medium* quality cuts (to be described in chapter 5.4)

- a cut on the transverse energy of $E_T > 15$ GeV and be

- within $|\eta| < 2.5$

For muons the following criteria have been defined:

- transverse momentum of $p_T > 15$ GeV

- within $|\eta| < 2.5$ and

- reconstructed using the STACO algorithm

The same criteria as for electrons apply for jets.

Objects that pass the respective criteria are written into a so-called Ntuple on a per-event base. The analysis is then done within the ROOT framework using C++.

5.2.1 Overlap Removal

It is possible that one object gets identified more than once, leading to ambiguities. Therefore, objects get inserted in a pre-defined order and if one object has more than one representation, the one with higher priority is taken.

Muons have the highest priority and get never removed. Ambiguities between electrons and photons will be solved by removing the photon. Jets have the lowest priority and get removed if they interfere with another object. Additionally, jets overlapping with electrons, photons or taus in a cone of $R = 0.3$ will be removed.

5.3 Trigger Studies

The ATLAS trigger system has been introduced in chapter 4.2. For this analysis a selection of the full trigger menu has been chosen. Both decay channels studied require two or more leptons, either electrons or muons, but no tau leptons. A trigger on electrons or muons with a certain threshold on the transverse momentum has been applied. Only single lepton triggers have been used and no dilepton triggers were required because the efficiency of dilepton triggers is the squared efficiency of single lepton triggers.

The trigger efficiencies have been calculated for all three trigger levels, namely Level 1 (L1), Level 2 (L2) and the Event Filter (EF) separately and combined. The analysis contains only events which have passed all three trigger levels. Thresholds of the minimum transverse momentum are for muons

- Level 1: $p_T > 20$ GeV

- Level 2: $p_T > 15$ GeV
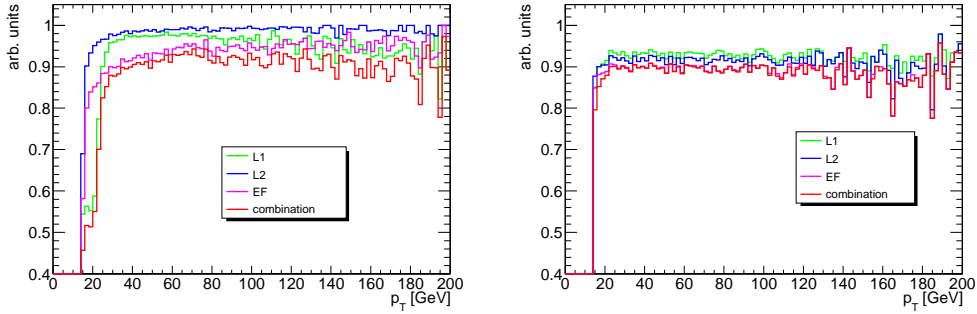
Figure 5.2: Turn on curves for electron (left) and muon (right) triggers. The efficiency of single trigger levels is shown, as well as the combination of all three levels.

	Level 1	Level 2	Event Filter	Combination
electrons	94.5	98.2	93.9	88.8
muons	92.4	91.0	88.9	88.5

Table 5.1: Trigger efficiencies in % for the electron and muon triggers, splitted up into several subtrigger Level 1, Level 2 and Event Filter. The numbers for each level do not include the preceding trigger stages. The last column is the combination of all three trigger levels. The efficiency for the L1 electron filter is lower than L2 and EF, because it has a higher p_T threshold of 23 GeV instead of 15 GeV.

- Event Filter: $p_T > 15$ GeV

The L1 muon trigger is exclusive, which means that a combination of the lowest trigger threshold and all successive thresholds has to be considered. The thresholds of L1 had to be chosen differently from L2 and EF, because the trigger menu does not contain 15 GeV triggers on Level 1.

The following set of trigger thresholds has been chosen for electrons

- Level 1: $p_T > 23$ GeV

- Level 2: $p_T > 15$ GeV

- Event Filter: $p_T > 15$ GeV

The efficiency for the Level 1 electron filter is lower than Level 2 and the Event Filter, because it has a higher p_T threshold of 23 GeV instead of 15 GeV. The trigger efficiencies are given in table 5.1. The efficiencies are approximately 88% for the combination of the triggers. Figure 5.2 shows turn-on curves for the electron and muon triggers for the three trigger levels and the combination.

It can be seen, that the plateau is reached for values of 30 GeV for the electrons and at 20 GeV for the muons. Both thresholds are clearly below the initial cuts on the transverse momenta of the leptons, as will be shown in the next chapters. This means that the trigger turn on has nearly no effect on the analysis of the signal. The influence of a reduced selection efficiency for signal and background events on the significance has been studied and will be discussed in chapter 9.

5.4   Preselection

The preselection includes the basic selection of potential signal events from the input stream. The properties of and differences between each analysis channel will be described in the following chapters 6 and 7, but both rely on an identical preselection. Electrons or muons to be considered must fulfill several quality criteria. Muons must have been reconstructed with the STACO algorithm (see 5.1.2). Additionally, the flags *isCombined* and *bestMatch* are required. This ensures that the muon has been reconstructed using information from the Muon Spectrometer and the Inner Detector while *bestMatch* means if several tracks have been found, the one with the best fit is taken. Electrons to be considered have passed *medium* quality cuts (figure 5.3) and the electron must have either been reconstructed with the track-based algorithm or with the track-based algorithm and the cluster-based algorithm. This information is stored in the flag called *author*.

The *medium* electron identification includes the following cuts [10]:

- geometric acceptance of the detector: $|\eta| < 2.47$

- hadronic leakage: ratio of E_T in the first sampling of the hadronic calorimeter to E_T of the EM cluster

- first layer of EM calorimeter: energy deposit, shower width

- second layer of EM calorimeter: energy within cells, lateral width of the shower

- track quality: number of hits in pixel detector and SCT

- isolation: ratio of *etcone20* (see next page) to the total cluster energy

- vertexing-layer: number of hits in vertexing-layer

- track matching: $\Delta\eta$ and $\Delta\phi$ between cluster and track

- TRT: number of hits
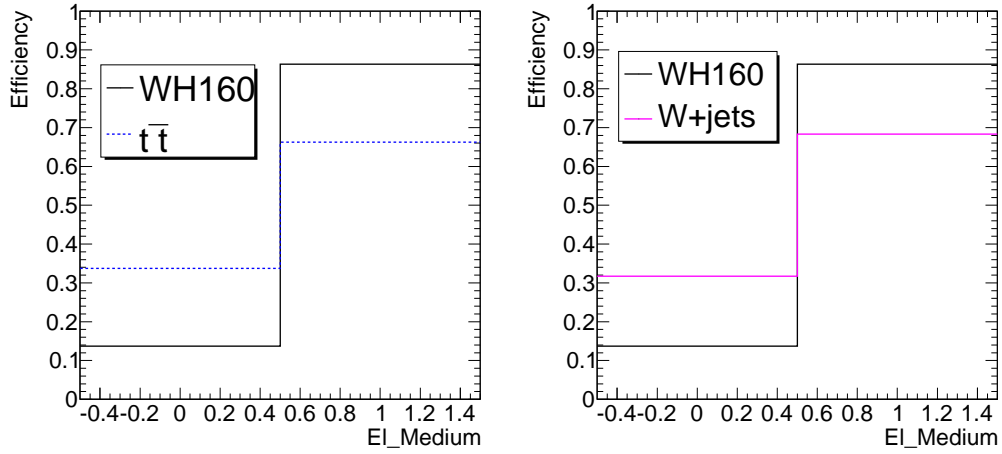
Figure 5.3: Ratio of events passing the medium quality cut for electrons.

Initially, the leptons have to pass a p_T cut of 15 GeV and be confined within a pseudorapidity range of $|\eta| < 2.7$. Electrons that get reconstructed within the so-called "crack region" $1.37 < |\eta| < 1.52$ are rejected, because there are no strip detectors in this region. Jets are constrained within the same η-region, but the minimum p_T is 20 GeV, in order to suppress events with soft jets, like QCD events. The Cone7 algorithm [10] described above (section 5.1.3) is used for the reconstruction of the jets.

Calorimeter isolation cuts on the transverse energy within a cone region of radius R around the lepton track (*etcone*) are also applied (as in fig. 5.1). For muons and electrons a value of *etcone* < 4 GeV has been chosen. Figure 5.4 shows the distribution of these variables for the signal process and selected background contributions. Some of the isolation criteria described above were not accessible for samples that have been reconstructed with Atlfast (mainly W+jets). This leads to a decrease in the performance, but has in this case no influence on the final event numbers.
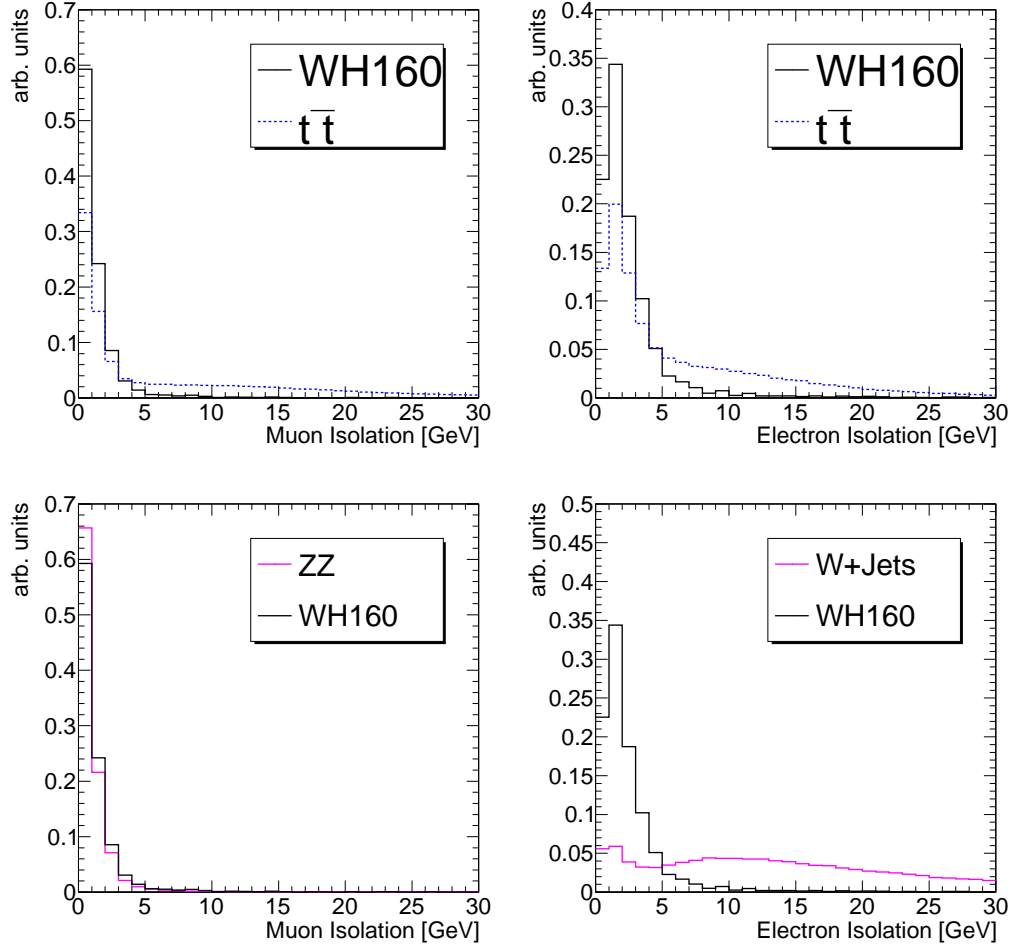
Figure 5.4: Isolation criteria $\sum\limits_{\#tracks < dR} E_T$ for muons (left) and electrons (right). The notation *"arb. units"* on the plots throughout this thesis implies that the curves have been normalised such that the area defined by each curve is equal to one.

Chapter 6

The Hadronic-Leptonic Decay Channel

In chapter 2, the theoretical foundations of the production and the decay of the Higgs boson have been presented. Starting with the preselection discussed in the last chapter, the following chapters will focus on the experimental situation. The starting point are three W bosons, where two are decay products of a Higgs boson which has been produced in association with an additional W boson: $WH, H \rightarrow WW$. In this channel, two W bosons must decay leptonically, while the third one decays hadronically, i.e. in jets. This decay channel will henceforth be referred to as WH2L. Figure 6.1 shows the Feynman diagram of this channel.

6.1 Signal and Backgrounds

6.1.1 The WH Signal

Out of the three W bosons, two are required to decay leptonically (only decays into electrons and muons are considered). This limitation is not unambiguous:

Process	m_H	$\sigma_{tot}(NLO)[fb]$	Generator	$\sigma \times BR[fb]$	N(events)
$WH \rightarrow 3W, \geq 2l$	130	1346.3	MC@NLO	33.78	5.5k
$WH \rightarrow 3W, \geq 2l$	140	1061.2	MC@NLO	43.82	5.5k
$WH \rightarrow 3W, \geq 2l$	150	845.6	MC@NLO	48.78	5.5k
$WH \rightarrow 3W, \geq 2l$	160	681.4	MC@NLO	50.31	5.5k
$WH \rightarrow 3W, \geq 2l$	170	554.7	MC@NLO	44.76	80k
$WH \rightarrow 3W, \geq 2l$	180	455.5	MC@NLO	35.36	5.5k
$WH \rightarrow 3W, \geq 2l$	190	377.2	MC@NLO	24.58	5.5k

Table 6.1: Monte Carlo signal samples for the $WH, H \rightarrow WW$ analyses
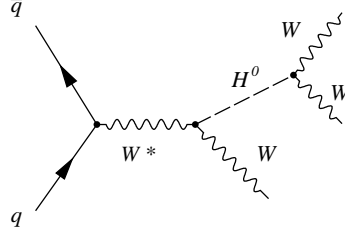
Figure 6.1: The Feynman diagram of the associated WH-production.

either both W bosons of the Higgs boson decay could decay leptonically, or the associatively produced W boson and one of the two W bosons of the decay of the Higgs boson. Both possibilities imply the presence of jets from the third W boson decay.

The decision on which leptons to choose is crucial and has huge influence on the potential backgrounds that have to be recognised in the analysis. Assume, the only limitation is the requirement of exactly two leptons. Then there could be two leptons of opposite charge or of same charge. Two oppositely charged leptons give rise to contributions from many backgrounds, because the leptonic decay of neutral particles (like Z bosons) leads to a pair of oppositely charged leptons. The W^+W^- diboson process would be one of the main background sources. By requiring two leptons with the same charge, the influence of these prospective backgrounds becomes nearly negligible. One could also say, the Higgs boson gets *tagged* by the two leptons of same charge. Therefore, in the following discussion only events with exactly two leptons with the same charge have been considered.

Seven different mass-points for the Higgs boson have been investigated: $m_H = 130, 140, 150, 160, 170, 180$ and 190 GeV. As will become clear from the discussion, it is feasible to use the same cut parameters for all mass points. The discussion mostly focusses on one mass point, namely $m_H = 160$ GeV, chapter 6.3 summarises differences for the respective mass points. The exclusion of a Higgs boson within a mass range of $m_H = 160 - 170$ GeV at 95% C.L. has been mentioned in chapter 2.5.1. Nevertheless a mass point of $m_H = 160$ GeV has been chosen because it is in the middle of the mass range that has been investigated throughout this thesis. All Higgs samples have been generated with MC@NLO and hadronised with HERWIG, with a filter applied onto the number of leptons (at least two leptons) and cuts on the transverse momentum of $p_T > 14$ GeV for

electrons and $p_T > 5$ GeV for muons; all leptons are restricted to a pseudorapidity range of $|\eta| < 2.7$. The filter efficiency is approximately 40% for each sample. Table 6.1 lists the main features of the Monte Carlo samples used for the signal.

6.1.2 Diboson Background

As mentioned above, only events with two leptons of the same charge are analysed. This basically rules out the W^+W^- background because, aside from misreconstructions, the leptons will have opposite charge. The second diboson background, ZZ, in principle is more critical, because both bosons decaying leptonically produce two pairs of leptons with the same charge ($Z \to l^+l^-l^+l^-$), but as mentioned earlier, only events with exactly two leptons are considered. This does not rule out this background *a priori*, because two of the four leptons could have a too low momentum or not have been reconstructed, because of detector properties. The most critical diboson background for this channel is the WZ process. Both bosons have to decay leptonically in order to give two same-charge leptons, but as for the other backgrounds, not all leptons might have been properly reconstructed.

The Monte Carlo samples used have been generated with several generators. The W^+W^- sample has been generated with MC@NLO. There has been no filter applied, the decay has been forced with a MC@NLO parameter. The minimum transverse momentum of leptons is $p_T > 10$ GeV. ZZ boson samples have been generated with PYTHIA or HERWIG. The HERWIG sample has a lepton filter applied, only events with at least one electron or one muon with $p_T > 10$ GeV and $|\eta| < 2.8$ are accepted. The fully leptonic PYTHIA sample includes a four-lepton filter on generator level, with all leptons above $p_T > 5$ GeV and within $|\eta| < 2.7$. The results have been obtained with the PYTHIA generated sample, because of the higher Monte Carlo statistics. Results are consistent with the HERWIG sample within the statistical limits. The WZ process has been generated at next to leading order with MC@NLO as well as in leading order with standalone HERWIG. The WZ HERWIG sample has the same filter applied as the respective ZZ sample: at least one electron or muon with $p_T > 10$ GeV and $|\eta| < 2.8$, while the MC@NLO sample has no filters applied, the transverse momentum threshold of leptons is $p_T > 10$ GeV. The cutflow table contains results of the MC@NLO sample and are consistent with those of the HERWIG generated events.

6.1.3 Top Pair Background

$t\bar{t}$ pair production has a large cross-section at LHC. It is therefore expected to contribute to the background and to have an impact on the optimisation of cuts. *top* quarks decay as $t \to Wb$. With the W bosons decaying leptonically, two oppositely charged leptons are formed, but through a decay of the *bottom* quark via $b \to Wc$ subsequently followed by the decay of the W boson, another lepton

Process	$\sigma_{tot}(NLO)[fb]$	Generator	ϵ_{filter}	$\sigma \times BR \times \epsilon_{filter}[fb]$	N(FullSim)	N(FastSim)
$t\bar{t}$ no all-hadronic	833000	MC@NLO	0.54	450000	526000	—
$t\bar{t}$ same-sign filter	833000	MC@NLO	0.0384	32000	352000	—
WZ	47760	Herwig	0.29	7800	48000	206000
WZ 3l decay	49950	MC@NLO	—	750	94000	—
ZZ	206.4	Pythia	0.22	45.2	94500	—
ZZ	14750	Herwig	0.19	72.5	48000	174000
WW	112000	MC@NLO	—	1418	76000	—
$Wb\bar{b}$	27000	Alpgen	0.0208	11.7	20000	—
Wt	66000	AcerMC	—	26700	18000	—
$W(e\nu) + 0$ partons	$16360 \cdot 10^3$	Alpgen	0.131	$1760 \cdot 10^3$	—	224000
$W(e\nu) + 1$ parton	$4740 \cdot 10^3$	Alpgen	0.631	$1650 \cdot 10^3$	—	172000
$W(e\nu) + 2$ partons	$2029 \cdot 10^3$	Alpgen	0.710	$587 \cdot 10^3$	—	137000
$W(e\nu) + 3$ partons	$770 \cdot 10^3$	Alpgen	0.737	$177 \cdot 10^3$	—	120000
$W(e\nu) + 4$ partons	$273 \cdot 10^3$	Alpgen	0.731	$49.3 \cdot 10^3$	—	11000
$W(\mu\nu) + 0$ partons	$16360 \cdot 10^3$	Alpgen	0.0610	$819 \cdot 10^3$	—	99500
$W(\mu\nu) + 1$ parton	$4740 \cdot 10^3$	Alpgen	0.628	$1630 \cdot 10^3$	—	200000
$W(\mu\nu) + 2$ partons	$2029 \cdot 10^3$	Alpgen	0.712	$588 \cdot 10^3$	—	62000
$W(\mu\nu) + 3$ partons	$770 \cdot 10^3$	Alpgen	0.738	$174 \cdot 10^3$	—	100000
$W(\mu\nu) + 4$ partons	$273 \cdot 10^3$	Alpgen	0.738	$50.4 \cdot 10^3$	—	22000

Table 6.2: Monte Carlo background samples for the WH, $H \to WW$ analyses.

can contribute to the signal. Especially, one W boson decaying into jets and a simultaneous decay of the other W boson into two leptons can contaminate the signal. For the study of the $t\bar{t}$ background a MC@NLO sample has been used. The applied filter selects events with leptons of the same charge if only two leptons have been found. The minimum transverse momentum of the leptons is $p_T > 10$ GeV.

6.1.4 W+Jets Background

W bosons can be produced in association with light jets or heavy (*bottom* or *top*) quarks. The quarks hadronise and build jets. These jets could be misreconstructed as leptons. In combination with a lepton from the W boson decay this could lead to signal-like events. The main difficulty of this background is the huge production cross-section, which makes an in-depth Monte Carlo study not feasible for large integrated luminosities. Only fast simulated (ATLFAST) events were available for the W+jets channel. The events itself have been generated with ALPGEN. The filter requires at least one lepton with $p_T > 10$ GeV within $|\eta| < 2.7$ and at least one jet with a transverse momentum of $p_T > 20$ GeV and $|\eta| < 5.0$.

6.1.5 Summary of Backgrounds

The same-charge requirement on the leptons is a very powerful constraint. There is virtually no background that resembles the topology of the signal perfectly, but several ones that could pass the selection cuts and therefore fake a signal event. Table 6.2 summarises details of the background samples used.

6.2 Event Selection

6.2.1 The Momentum Distribution of Leptons

As illustrated above, this analysis channel relies on an initial selection of two leptons (electrons or muons) with the same charge. After filtering events fulfilling this basic requirement, firstly cuts on the transverse momenta (p_T) of the leptons are applied. The leptons are products of W boson decays and hence high-energetic. Figure 6.2 shows the momentum distribution of the signal leptons and selected backgrounds[1]. It can be seen that especially the p_T distribution of the second-leading lepton looks substantially different for the signal and the backgrounds, in particular the $t\bar{t}$ background. These leptons are misreconstructions or products of the b-quark decay.

---

[1]Plots in chapters 6 and 7 have been created with lowered p_T-cuts due to statistics reasons.
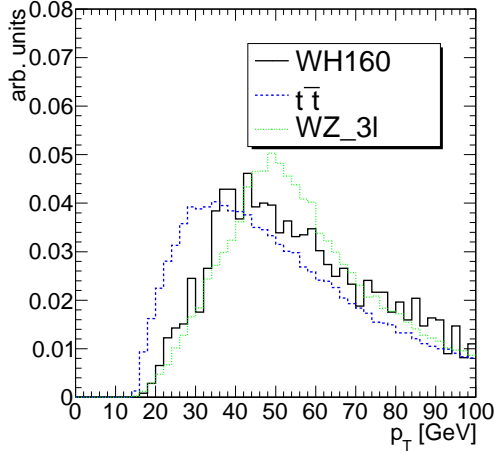
(a) p_T of leading leptons for $WH, t\bar{t}, WZ$
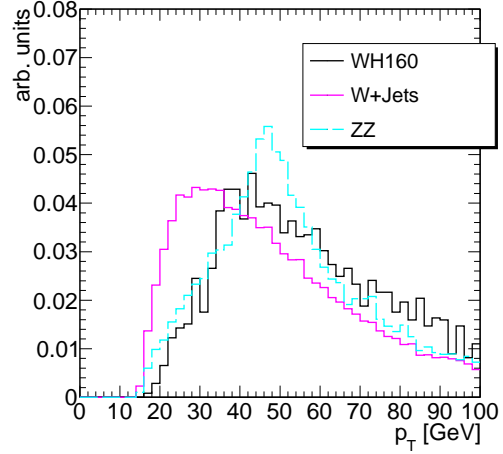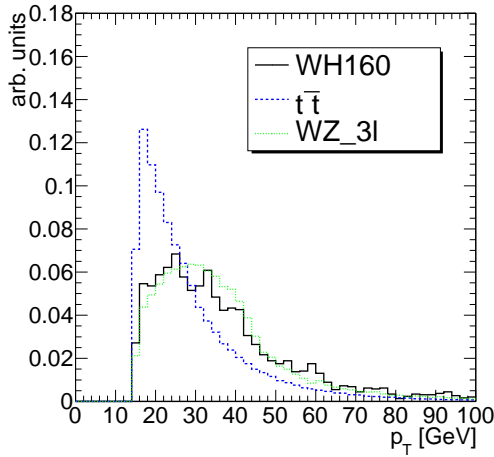
(b) p_T of leading leptons for $WH, W+$Jets, ZZ

(c) p_T of second-leading leptons for $WH, t\bar{t}, WZ$
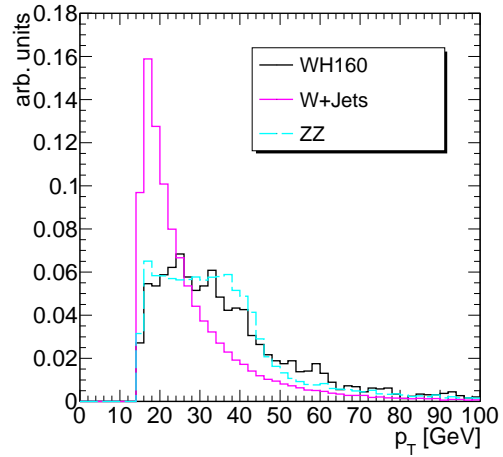
(d) p_T of second-leading leptons for $WH, W+$Jets, ZZ

Figure 6.2: The momentum distributions for the leading (*a* and *b*) and second-leading (*c* and *d*) leptons for the signal and selected background processes.

As lower thresholds for the transverse momenta of the leptons the following cuts have been chosen:

- $p_T^1 > 35$ GeV

- $p_T^2 > 35$ GeV

These cuts are relatively tight and even though a substantial part of the signal is cut away, they are very efficient in cutting away the background. Especially the W+jets background has lower energetic leptons and these events can be rejected with high efficiency using a large cut on the lepton momenta.

In case there is a third lepton reconstructed, the event is a candidate for the leptonic decay channel (to be discussed in chapter 7). Nonetheless, if the third lepton is low energetic, i.e. has a transverse momentum $p_T < 22.5$ GeV, the event will be discarded for the pure-leptonic channel. If the remaining two leptons are of same charge with sufficient momenta, these events will be added to the WH2L channel.

6.2.2 Reconstruction of the W Boson Mass

For the signal process, two leptons out of three W bosons imply the existence of jets from the decay of the third W boson. Figure 6.3 shows the number of jets if a pair of leptons with the same charge above the p_T-threshold is found. From the Feynman diagram of the $t\bar{t}$ decay (shown in figure 2.5) the larger hadronic activity compared with the signal becomes clear. The contribution of the b-quarks leads to additional jets, altogether there are approximately 3 per event. For the WZ diboson background only the W boson produces high-energetic jets. Hence a lower mean number of jets is expected than for the signal.

Using the jet with the highest transverse energy, with each additional jet an invariant mass can be calculated. This mass resembles that of the W boson, at least for the signal process. For the $t\bar{t}$ process there is a higher number of jets available and also more combinations, which leads to a slightly wider shape of the reconstructed mass. Regarding the WZ background, the distribution is much broader. The reason is due to the leptonic decay of both bosons, which goes along with the absence of hard jets. In that case, only jets from initial or final state radiation are used for the reconstruction. For all jets the invariant mass with the smallest deviation from the true mass of the W boson is taken, shown in fig. 6.4. There will always be a combination, but as it can be quite different from the real W mass, the distribution is broadened. The following cut window has been chosen

- 65 GeV $< m_{jj} < 105$ GeV with $p_T^{jets} > 20$ GeV

to remove the tails of the invariant mass of the jets, which are dominated by background events.
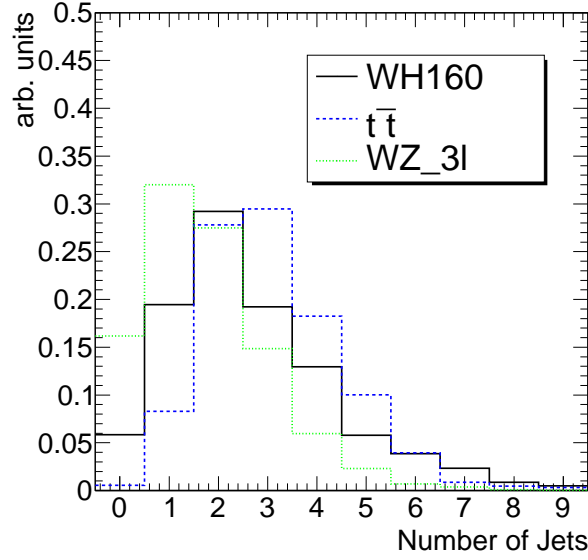
Figure 6.3: Number of jets if a pair of same sign leptons is found after preselection.
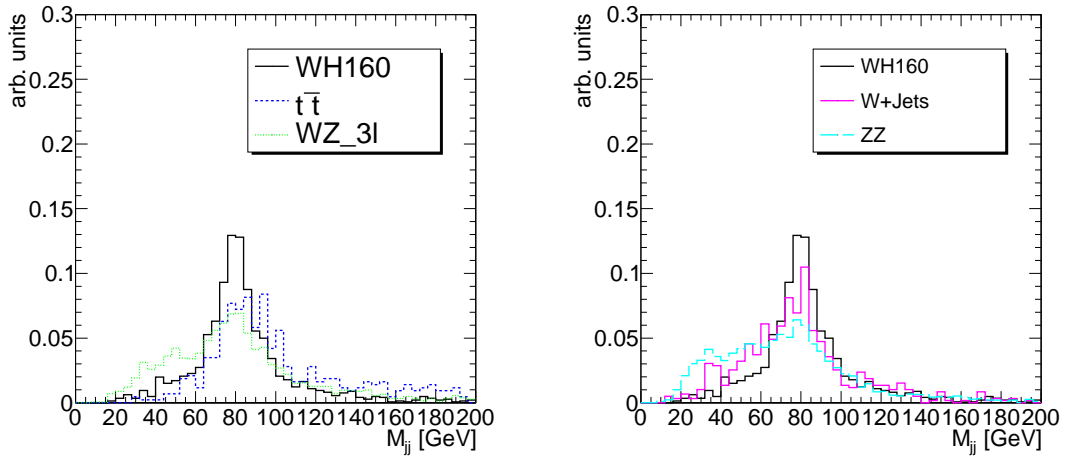
(a) M_{jj} for $WH, t\bar{t}, WZ$

(b) M_{jj} for WH, W+Jets, ZZ

Figure 6.4: The invariant mass reconstructed from the two jets with the highest transverse momenta.
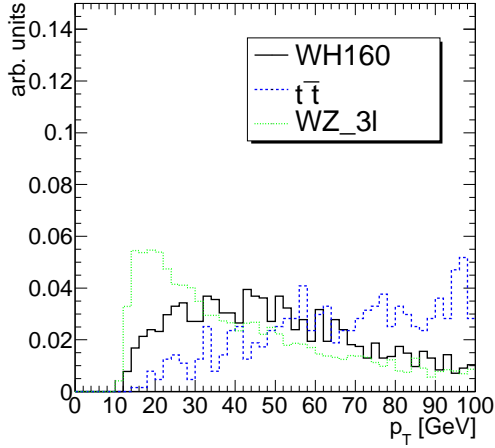
(a) p_T of leading jet for $WH, t\bar{t}, WZ$
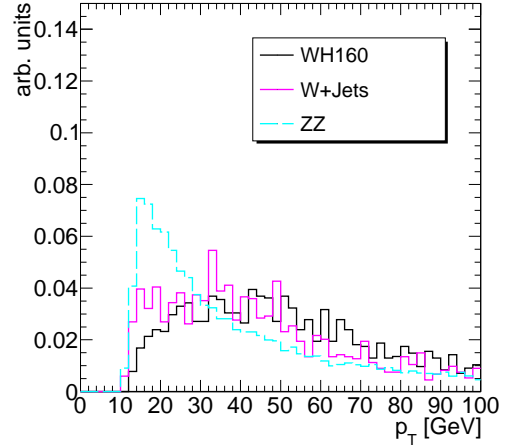
(b) p_T of leading jet for $WH, W+$Jets, ZZ
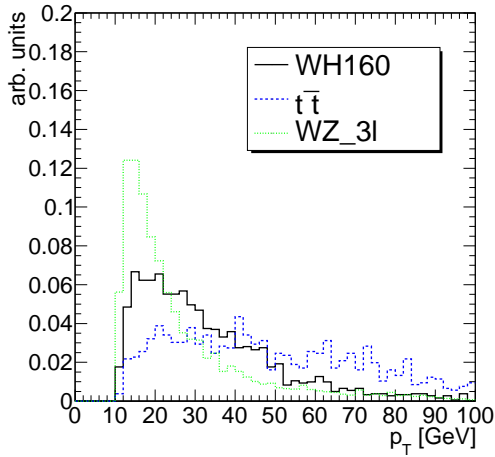
(c) p_T of second-leading jet for $WH, t\bar{t}, WZ$
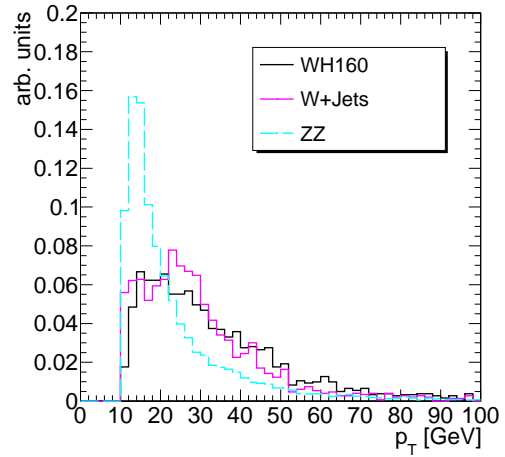
(d) p_T of second-leading jet for $WH, W+$Jets, ZZ

Figure 6.5: The momentum distributions for the leading (*a* and *b*) and second-leading (*c* and *d*) jet for the signal and selected background processes.

6.2.3   Hadronic Activity

The two high-energetic jets from the decay of the W boson can be used to further discriminate the signal from the background. Additional jets are usually low energetic because they do not originate from the hard interaction process. It can be seen (figure 6.5) that there are clear differences in the shapes of the jet energies. The $t\bar{t}$ background for instance has more hadronic activity as stated above and higher jet energies. An explicit cut on jet momenta has been found to be more efficient than a cut on the sum of the energies of all jets; values of

- $p_T^{jet,1} < 75$ GeV

- $p_T^{jet,2} < 65$ GeV

(again, with $p_T^{jets} > 20$ GeV) as upper threshold of jet energies have been chosen as cuts.

6.2.4   Missing Transverse Energy

Finally, a cut on the missing transverse energy ($\not{E}_T$) is applied. For the signal, missing transverse energy is expected from the decay of two W bosons (decay: $W \rightarrow l\nu$). Most of the backgrounds show similar distributions of this parameter, larger differences occur for the ZZ background; because both Z bosons decay leptonically, no neutrinos can be created. The contribution to missing transverse energy is mainly due to misreconstructions or inefficiencies of the detector. Figure 6.6 illustrates this. The shape of the ZZ background is clearly different. Consequently, a low threshold for the missing transverse energy has been chosen:

- events with $\not{E}_T < 40$ GeV are rejected

6.3   Selection Criteria for Different Mass Points

It has been mentioned at the beginning that for all mass-points the same cut values have been chosen. This section illustrates the differences between the mass-points and thereby confirms this decision.

From looking at the momentum distributions of the leptons (fig. 6.7) the minor differences between the mass points becomes clear. In principle, there is a shift of the mean values, but in the order of 5 GeV from the lowest to the highest mass point. The cuts itself have been optimised especially for $m_H = 160$ GeV, which is in the middle of the mass range investigated. From that point the deviations from the mean value of the respective variable are smaller than 5 GeV. In fact, the mass-momentum dependence gets suppressed by the high cuts on the transverse momenta of the leptons. Furthermore, the same background samples
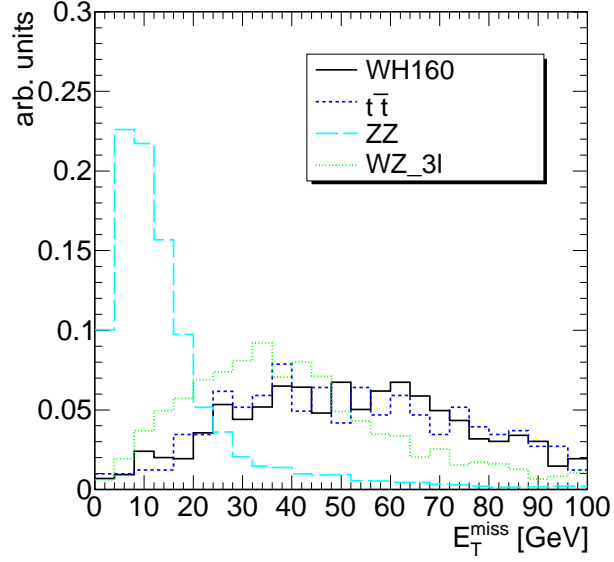
Figure 6.6: The distribution of the missing transverse energy ($\not{E}_T$) for the signal and selected backgrounds.
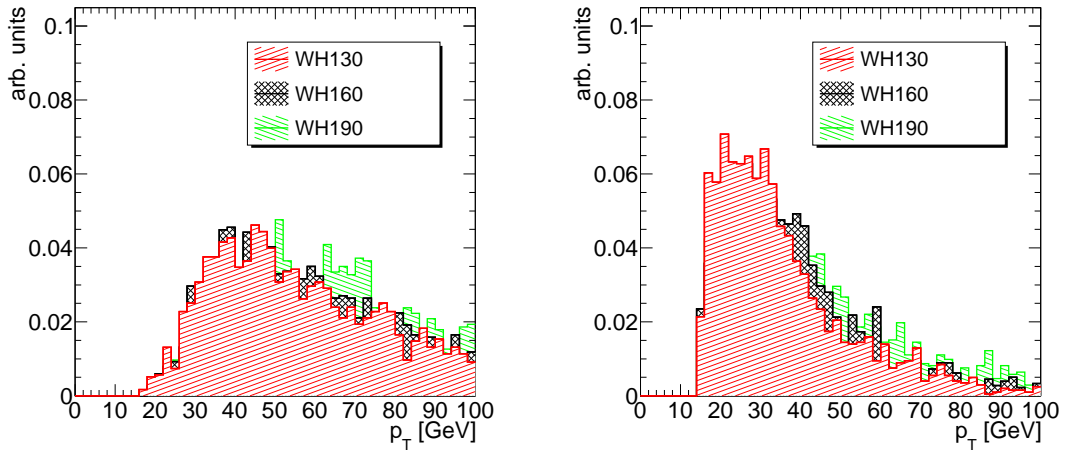
(a) p_T of leptons for $WH, t\bar{t}, WZ$

(b) p_T of leptons for $WH, W+$Jets, ZZ

Figure 6.7: Transverse momenta of the leptons (p_T^1 and p_T^2) for the mass points $m_H = 130, 160$ and 190 GeV.

(a) p_T of jets for $WH, t\bar{t}, WZ$

(b) p_T of jets for $WH, W+$Jets, ZZ
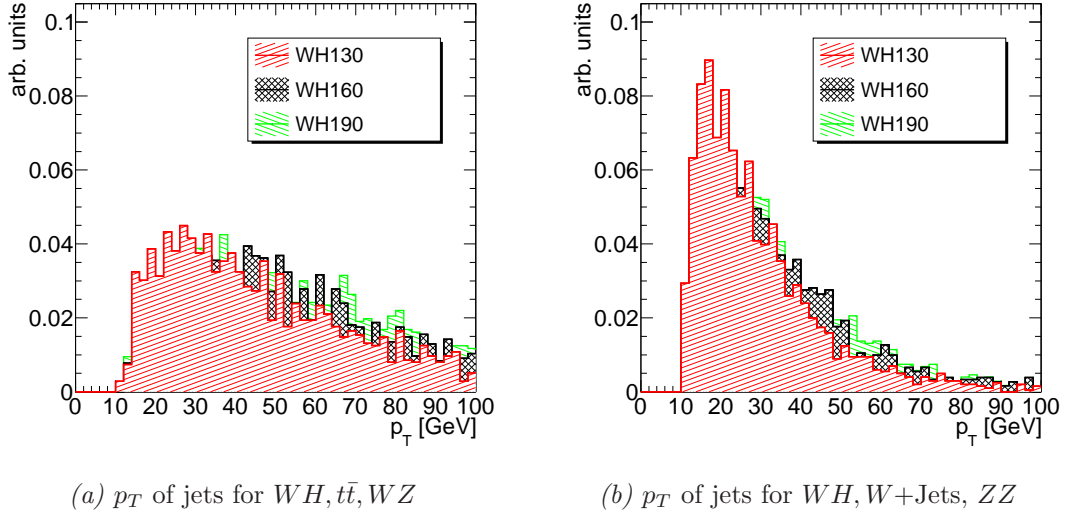
Figure 6.8: Transverse momenta of the jets (p_T^1 and p_T^2) for the mass points $m_H = 130, 160$ and 190 GeV.
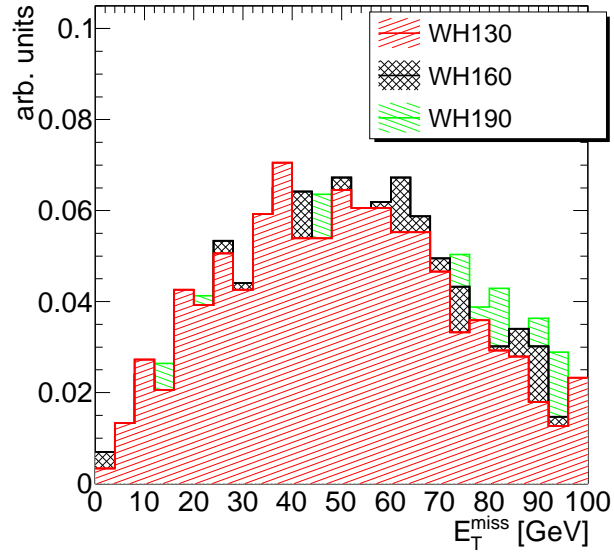
Figure 6.9: The distribution of the missing transverse energy ($\not{E}_T$) for the signal for the mass points $m_H = 130, 160$ and 190 GeV.

have been used for all mass points. This means, by not changing the cut values, the high background rejection does not change. Lowering cut values quickly gives rise to background contributions and that impairs the signal over background ratio. Figure 6.8 illustrates the differences in the jet energies and figure 6.9 those with respect to missing transverse energy. As explained for the lepton p_T, the differences are only small and with the statistics available a mass dependent optimisation of cuts is not possible.

6.4 Selection Efficiency and Cut Flow

The following list recapitulates the cuts and respective thresholds used for the analysis of the process $WH, H \to WW$ with $WWW \to l\nu l\nu + 2$ jets:

- exactly two leptons (e, μ) with same charge

- transverse momenta of the leptons: $p_T^1 > 35$ GeV, $p_T^2 > 35$ GeV

- dijet mass must be in the area 65 GeV $< M_{jj} < 105$ GeV

- transverse momenta of the jets: $p_T^{jet,1} < 75$ GeV, $p_T^{jet,2} < 65$ GeV

- $\not{E}_T > 40$ GeV

The efficiencies for the cuts on signal and backgrounds are summarised in table 6.3. From the cutflow table it becomes clear that a cut at such high p_T values rejects a substantial part – approximately 55% – of the signal events, but the background rejection is much higher. The WZ background is crucial because the event topology resembles that of the signal, while the $t\bar{t}$ background is important because of its large production cross-section. Hence, large cut values are used to safely remove most of the background contributions. Cutting on M_{jj} mainly rejects events from WZ and ZZ diboson processes, because of the Z bosons. The cut on the jet energies is most efficient for removing $t\bar{t}$ events, because of the additional jet, which can be high-energetic, too. As mentioned above, rejecting events with $\not{E}_T < 40$ GeV is very efficient applied onto ZZ dibosons. With respect to the Monte Carlo statistics, ZZ background can be estimated very precisely, as well as the WZ background. The main contribution of the statistical error is due to the $t\bar{t}$ background, because this process has a very large production cross section.

Process	Basic Cuts	p_T/Charge	M_W	Jets	$\not{E}_T$
WH, 130 GeV	340.0	112.3	57.6	28.3	18.0 ± 2.2
WH, 140 GeV	471.3	159.9	79.7	47.8	29.1 ± 3.4
WH, 150 GeV	546.7	212.0	114.5	58.1	36.5 ± 3.9
WH, 160 GeV	582.2	233.4	126.9	58.6	40.4 ± 4.2
WH, 170 GeV	508.2	214.4	119.6	60.0	42.9 ± 4.8
WH, 180 GeV	419.7	188.9	107.5	50.3	30.5 ± 3.1
WH, 190 GeV	290.6	141.9	81.0	33.1	21.7 ± 2.2
WZ 3l	676.3	135.8	49.3	24.4	8.4 ± 1.4
ZZ	38.5	11.6	4.14	2.24	0.1 ± 0.03
WW	1954	9.4	3.3	0	$0 + 0.8$
$t\bar{t}$	1931	86.2	32.3	5.4	5.4 ± 3.1
$Wb\bar{b}$	2.5	0	0	0	0
$W + jets$	6281	0	0	0	0
Wt	133.9	0	0	0	0
Sum of background events					13.9 ± 3.5

Table 6.3: Cutflow for the WH2L analysis for the different Higgs masses studied. Cross sections normalised to $\mathcal{L} = 30$ fb^{-1}. The numbers include only statistical uncertainties due to Monte Carlo statistics.

Chapter 7

The Leptonic Decay Channel

Following the last chapter on the two lepton channel, this chapter is dedicated to the pure leptonic decay of the three W bosons: $WH \rightarrow WWW \rightarrow l\nu l\nu l\nu$. The requirement of at least three leptons makes this channel fully independent from the WH2L channel. This channel will from now on referred to as WH3L.

7.1 Signal and Backgrounds

7.1.1 The WH Signal

The topology of the signal in this channel is simpler than for WH2L, because three leptons (and neutrinos) have to be considered, all of them are decay products of a W boson. Three high-energetic and isolated leptons (only electrons and muons are taken into account) in the final state rule out several potential backgrounds. Nonetheless, a detailed study of the remaining background events is necessary to be able to understand and predict the behaviour of those contributions. Furthermore, the low cross-section of this process (table 7.1) complicates the analysis. Again, only the mass point $m_H = 160$ GeV will be discussed in detail as the same cuts have been used for all mass points. Chapter 7.3 summarises the influence of the cuts on the respective mass points.

m_H [GeV]	130	140	150	160	170	180	190
$\sigma \times BR_{WH3L}$ [fb]	3.76	4.98	5.58	5.94	5.17	4.11	2.83

Table 7.1: Signal cross-sections for the leptonic decay channel. Numbers shown include the leptonic branching ratio of all three W bosons. Other parameters are the same as for table 6.1.
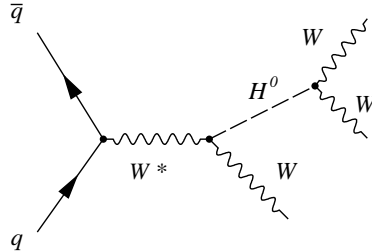
Figure 7.1: The Feynman diagram of the associated WH-production.

7.1.2   Diboson Background

If in a ZZ event at least three leptons are required, this is equivalent to requiring a leptonic decay of both Z bosons. Also, from this decay, no high-energetic jets and no missing energy will be expected. WZ decays are basically irreducible because of three leptons and missing transverse energy ($WZ \to l\nu ll$), which resembles the topology of the signal. As will be discussed in this chapter, for a discrimination the properties of the Z boson must be exploited. The process W^+W^- is mainly ruled out by requiring a third, high-energetic and isolated lepton.

The same backgrounds as for the WH2L channel have been used, therefore any parameters mentioned in chapters 6 and especially in table 6.2 are valid for this channel, too.

7.1.3   Top Pair Background

The $t\bar{t}$ background again contributes mainly to the background due to jets misidentified as leptons or leptons from the decay $b \to Wc$. This way three leptons, two from the direct decay $t \to Wb$ and one through a misreconstruction or a decay through a virtual W boson. This still leaves one b quark unconsidered, which contributes as jet or additional lepton. Overall, this background can be controlled very well, but has a large production cross-section. Chapter 6.1.3 and table 6.2 give an overview about the properties of the Monte Carlo samples used.

7.1.4 W+Jets Background

The W+jets background has only little to none impact to the background contamination. Again, one lepton can be expected from the decay of the W boson, additional leptons must be products of faked leptons (i.e. misreconstructed jet). This background has to be studied because of its huge production cross-section, and it will be shown, that it can be neglected. As for the other backgrounds, the same samples as for WH2L have been used (chapter 6.1.4 and table 6.2).

7.2 Event Selection

7.2.1 The Momentum Distribution

After filtering for three or more leptons (electrons or muons), which makes this channel independent of WH2L, firstly cuts on the lepton momenta are applied in order to conveniently reject events with completely different event topology. As stated above, the third lepton simplifies the analysis because of the minor background contribution. Therefore, the momentum thresholds could be adjusted accordingly:

- $p_T^1 > 35$ GeV

- $p_T^2 > 25$ GeV

- $p_T^3 > 22.5$ GeV

The cut on the transverse momentum of the second lepton has been reduced by 10 GeV compared with the WH2L channel. The third lepton has to pass $p_T^3 > 22.5$ GeV, and if the latter threshold is not passed, the event is treated as candidate for the WH2L analysis (chapter 6). Figure 7.2 shows the distributions of the transverse momenta for the three leading-p_T leptons. Compared with the WH2L channel, the rejection of signal events is much smaller. This is due to the lowered threshold for the second lepton. Three isolated and high-energetic leptons are already sufficient to remove all W+jets background events. For a faked signal, there must be (at least) two misreconstructed leptons, which need to be isolated.

7.2.2 Spin Correlation

The Standard Model Higgs boson is a scalar spin 0 particle. Therefore, the W bosons from the decay of the Higgs boson will have opposite spin orientation, which also affects the leptons as decay products of these W bosons [53, 54, 55]. In order to neglect effects through the boost of the particles, only the transverse plane is recognised. This corresponds to the angular distance in the ϕ-plane. For
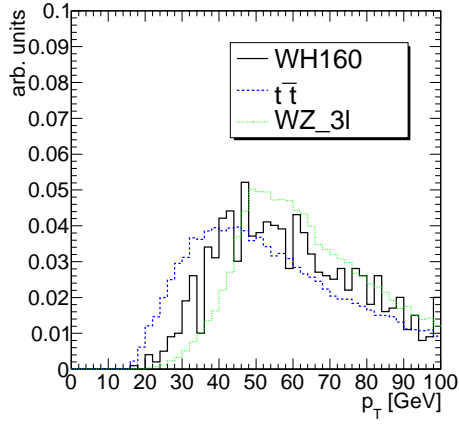
(a) p_T of leading leptons for $WH, t\bar{t}, WZ$
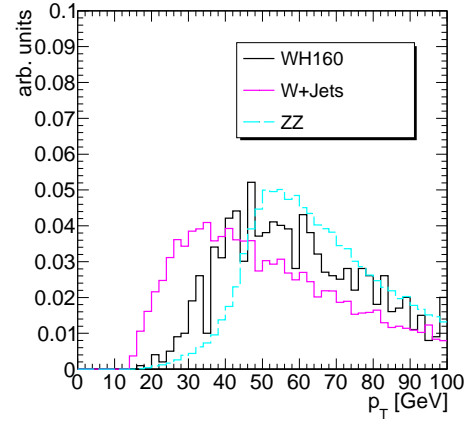
(b) p_T of leading leptons for $WH, W+$Jets, ZZ
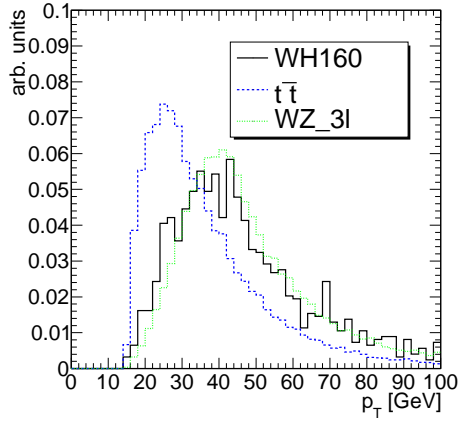
(c) p_T of second-leading leptons for $WH, t\bar{t}, WZ$
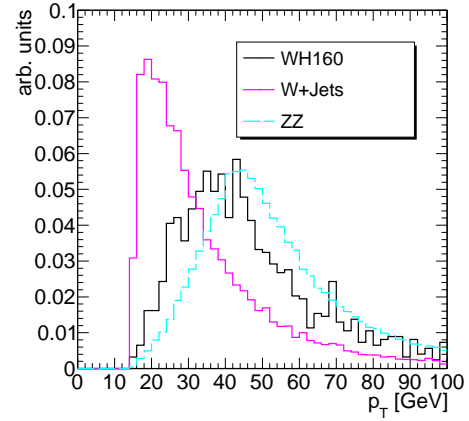
(d) p_T of second-leading leptons for $WH, W+$Jets, ZZ
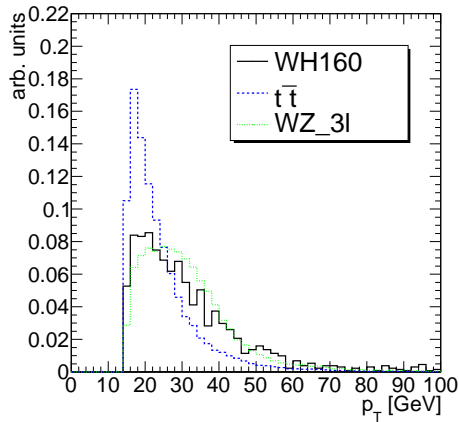
(e) p_T of third-leading leptons for $WH, t\bar{t}, WZ$
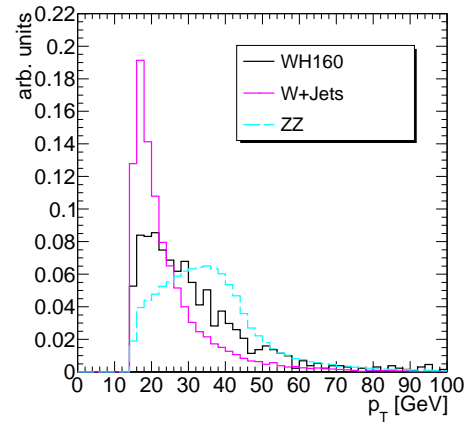
(f) p_T of third-leading leptons for $WH, W+$Jets, ZZ

Figure 7.2: The momentum distributions for the leading (*a* and *b*), second-leading (*c* and *d*) and third-leading (*e* and *f*) leptons for the signal and selected background processes.
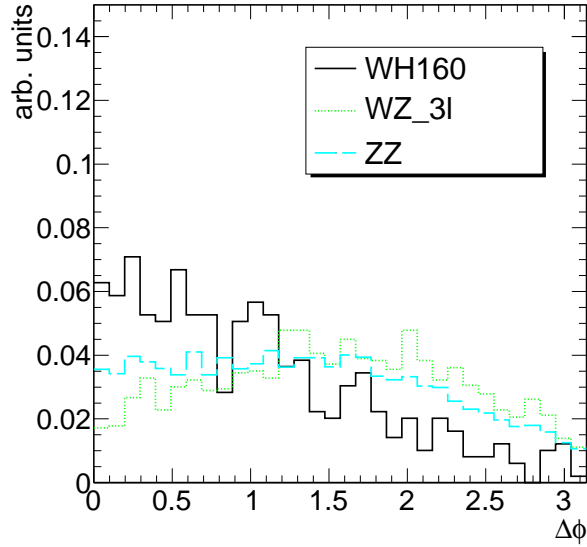
Figure 7.3: The distance in ϕ between the two opposite sign, same flavour leptons.

an efficient reduction of backgrounds that do not underlie this correlation, a value of

- $\Delta\phi < 1.1$

has been chosen after selecting only those leptons with opposite charge. In case more than one combination is possible, the smaller combination is chosen. Figure 7.3 shows the angular distribution for the signal and several background processes. The backgrounds show a flat distribution of the angles between the leptons, while the expected correlation clearly can be observed.

7.2.3 Hadronic Activity

Requiring the W bosons to decay leptonically implies the absence of jets with high transverse energy within the signal process. The hadronic fraction of the signal contains only jets from underlying events or pile-up, which are low-energetic. As a consequence, events with jets having a

- $p_T^{jet,1} > 60$ GeV and
- $p_T^{jet,2} > 30$ GeV

are rejected. The distribution of the transverse momenta of the jets is shown in figure 7.4. A cut on the transverse momenta was preferred over a cut on the sum of the jet energies in order to be more independent of underlying events or
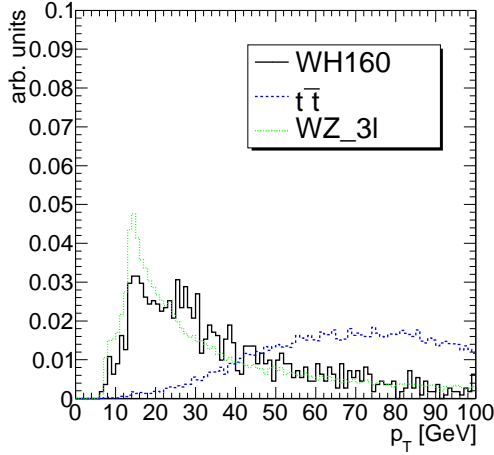
(a) p_T of leading jets for $WH, t\bar{t}, WZ$
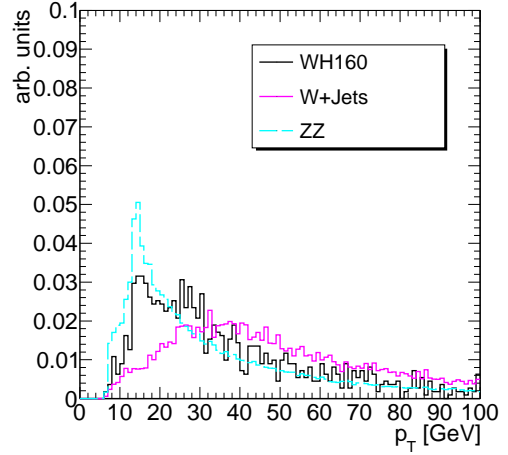
(b) p_T of leading jets for $WH, W+$Jets, ZZ
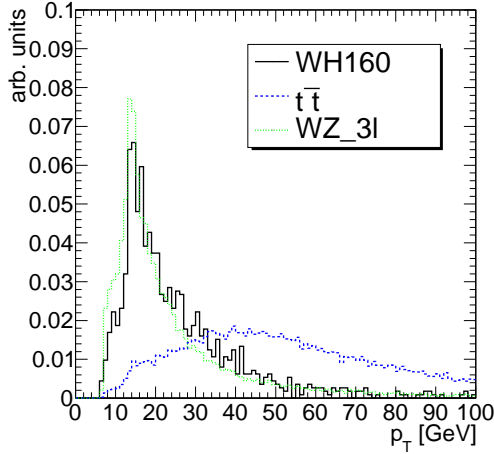
(c) p_T of second-leading jets for $WH, t\bar{t}, WZ$
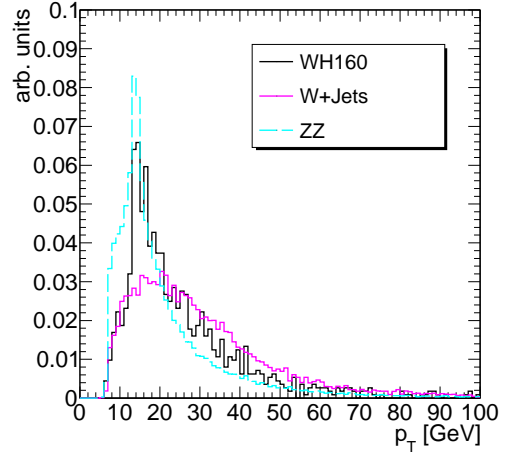
(d) p_T of second-leading jets for $WH, W+$Jets, ZZ

Figure 7.4: The momentum distributions for the leading (*a* and *b*) and second-leading (*c* and *d*) jets for the signal and selected background processes.
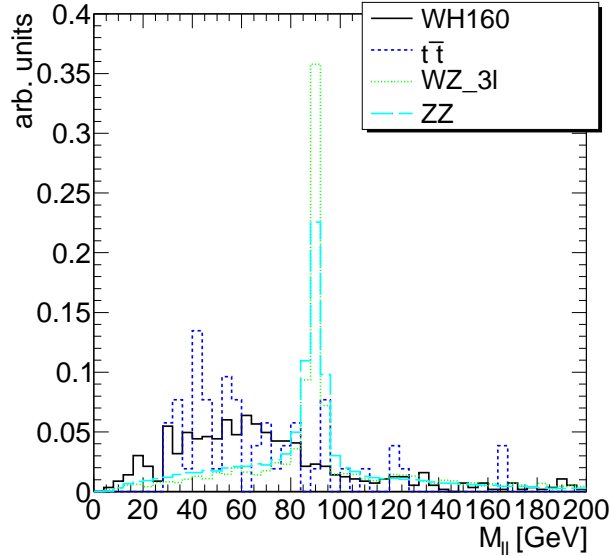
Figure 7.5: The dilepton mass reconstructed from two opposite sign, same flavour leptons.

pile-up effects. In more detail: jets from soft processes add to the sum of the jet energies. This contribution is hard to measure, in contrary to high-energetic jets, which are easier to identify. Hence, rejecting events with larger hadronic activity is easier to achieve and is less dependent on the jet energy scale.

7.2.4 Reconstruction of the Z Boson Mass

It has been mentioned at the beginning, that the WZ decay is one of the largest irreducible backgrounds. A pure leptonic decay of a W and a Z boson resembles the topology of the decay of a signal event. A major difference that can be exploited very well is the decay of the Z boson. The reconstruction of the invariant mass of two leptons with the same flavour, but opposite charge gives a clear peak around the mass of the Z boson, as illustrated in figure 7.5. The signal process does not contain a Z boson, consequently no mass peak can be reconstructed. This is a very powerful cut to reject background events containing a Z boson. As cut has been chosen:

- a cut window centered at $M_Z = 91.2$ GeV with a width of $M_Z \pm 20$ GeV

This cut is mainly responsible for the high background rejection potential of this channel.
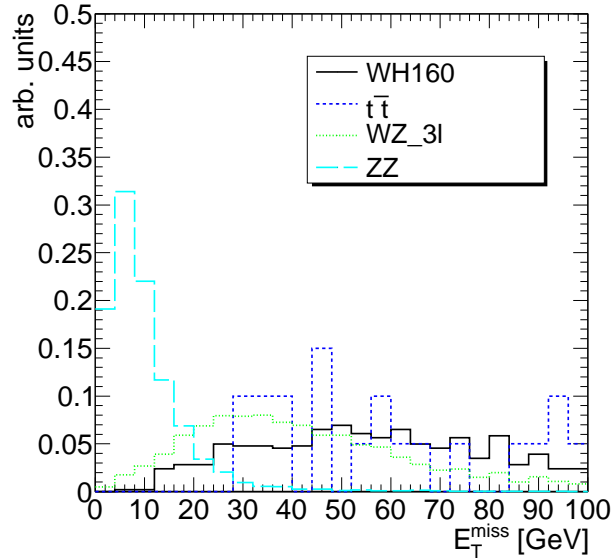
Figure 7.6: The missing transverse energy for the signal and selected background processes for the 3 lepton channel.

7.2.5 Missing Transverse Energy

The leptonic decay of the three W bosons produces three neutrinos that contribute to the missing transverse energy. The backgrounds behave differently. The decay of the W bosons produces only one neutrino, while from the decay of a Z boson no neutrinos and therefore no missing energy due to physics reasons can be expected. Nevertheless do all events contain a fraction of missing energy, that can be explained with detector effects (see chapter 5.1.4 for more details). Events have to pass the following criteria for missing transverse energy:

- $\not{E}_T > 40$ GeV

Figure 7.6 shows the distribution of missing transverse energy for the signal and selected backgrounds.

7.3 Selection Criteria for Different Mass Points

Like for the WH2L selection, for this channel no mass-dependent cuts have been used. Looking at the cuts presented in this chapter, the initial cut on the transverse momenta of the leptons and the cut on the missing transverse energy could suggest a mass-dependent behaviour. Figures 7.7 and 7.8 illustrate this. Nevertheless, there are only little deviations for each of the mass points. Overall, the shift of the mean momenta is approximately 5 GeV. Lowering one or more of the

p_T cuts about this value has very little impact on the signal, but gives rise to background contributions.

The same applies for the missing transverse energy. With respect to the available Monte Carlo statistics, the shift is negligible and no adjusting of the cut values has been applied. In figure 7.9 the transverse momenta of the jets are shown, for three mass-points. As mentioned earlier, there are no hard jets to be expected, as all three W bosons decay leptonically. Thus, the jet contribution stems from the event remnant and no shift for the mass-points can be seen. The spin correlation as well as the calculation of the invariant mass is independent of the mass of the Higgs boson.

To conclude, a modification of cuts which depend on the mass of the Higgs boson have emerged as insensitive for the signal efficiency, but would have given rise to background contributions and therefore have been dismissed.

7.4 Selection Efficiency and Cut Flow

In this section the selection efficiencies for the signal and the background processes will be discussed. Firstly, the cuts and respective thresholds are summarised:

- at least three leptons (e, μ)

- momenta of the leptons: $p_T^1 > 35$ GeV, $p_T^2 > 25$ GeV, $p_T^3 > 22.5$ GeV

- spin correlation between leptons with opposite charge: $\Delta\phi_{ll} < 1.1$

- momenta of the jets: $p_T^{jet,1} < 60$ GeV, $p_T^{jet,2} < 30$ GeV

- dilepton mass of leptons with opposite charge: $M_{ll} = M_Z \pm 20$ GeV

- $\slashed{E}_T > 40$ GeV

Table 7.2 shows the efficiencies of the cuts for each mass point of the Higgs boson signal as well as for the backgrounds investigated. The loss of events after the initial cut on the transverse momenta is smaller than for WH2L. The reason is the lowering of the threshold for the lepton with the second-highest transverse momentum. This has been done, because the influence of the backgrounds *a priori* is smaller because of the three isolated leptons. The cut on the jet energies reduces mainly the $t\bar{t}$ background (by 43%). This is due to hadronic fraction of the $t\bar{t}$ decay, which does not occur for the WH signal. The most efficient cut for the WZ and ZZ diboson backgrounds is the veto on the mass window around the mass of a Z boson. Nearly all of the remaining events get rejected at that level. The cut on missing transverse energy has been applied at the end and again is very efficient at rejecting ZZ events. The main contribution to the statistical error again is due to $t\bar{t}$, because of limited Monte Carlo statistics.
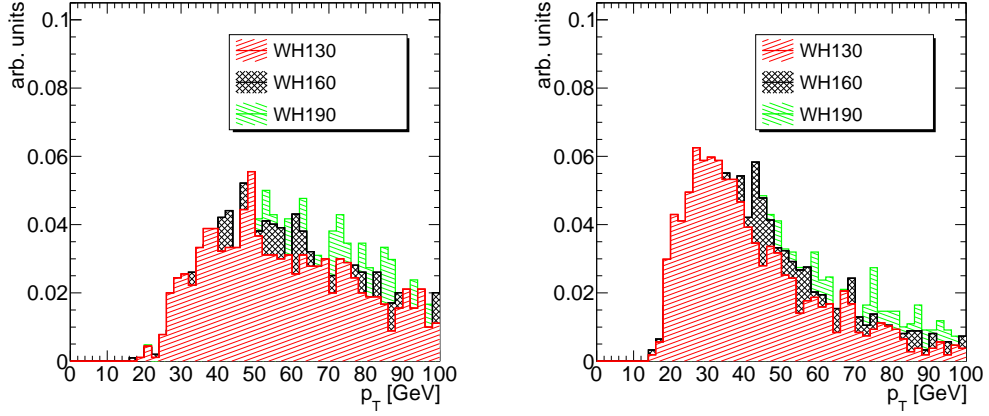
(a) p_T^1 of leptons for $m_H = 130, 160$ and 190 GeV

(b) p_T^2 of leptons for $m_H = 130, 160$ and 190 GeV
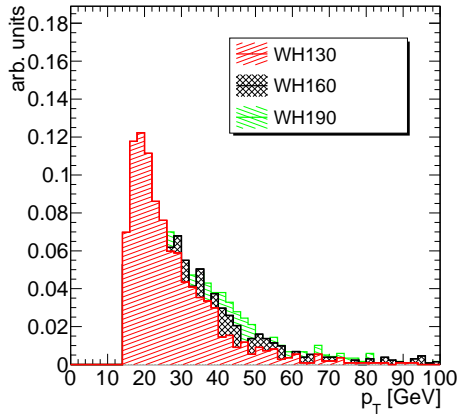
(c) p_T^3 of leptons for $m_H = 130, 160$ and 190 GeV

Figure 7.7: Transverse momenta of the leptons (p_T^1, p_T^2 and p_T^3) for the mass points $m_H = 130, 160$ and 190 GeV.
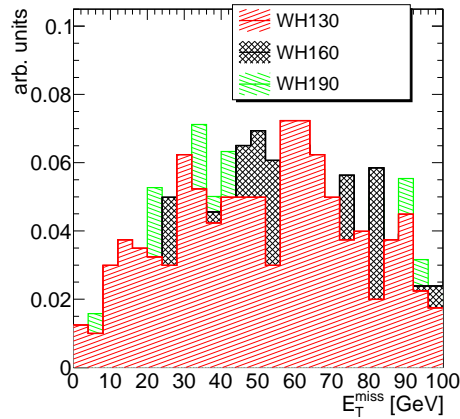
(a) $\not{E}_T$ for $m_H = 130, 160$ and 190 GeV

Figure 7.8: The distribution of the missing transverse energy ($\not{E}_T$) of the signal for the mass points $m_H = 130, 160$ and 190 GeV.
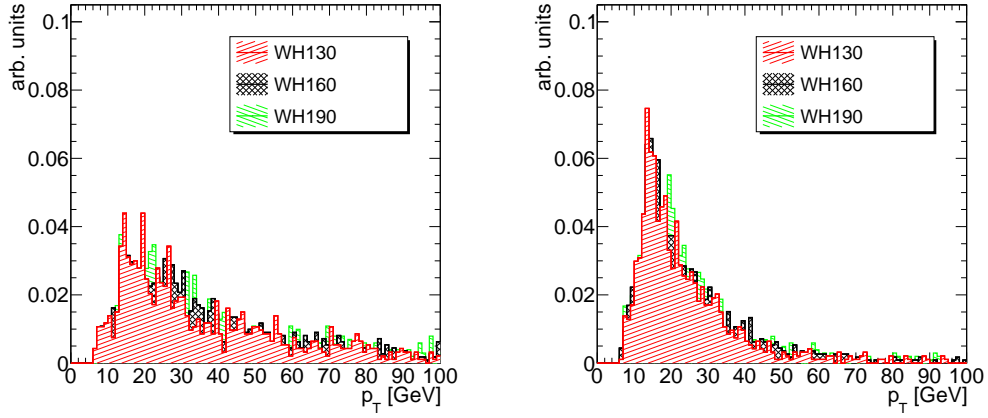
(a) p_T of jets for $m_H = 130, 160$ and 190 GeV

(b) p_T of jets for $m_H = 130, 160$ and 190 GeV

Figure 7.9: Transverse momenta of the jets (p_T^1 and p_T^2) for the mass points $m_H = 130, 160$ and 190 GeV.

As discussed, the contributions of the $W+$jets backgrounds have been studied without the preselection. It can be seen that the respective cuts are very efficient on their own and no event survives. Due to the completely different event topology it is very unlikely for an event to pass all cuts. Therefore the $W+$jets backgrounds have been neglected in the cutflow.

Process	Basic Cuts	p_T	Spin Corr.	Jets	M_Z	$\not{E}_T$
WH, 130 GeV	42.9	23.8	16.1	10.4	8.1	5.4 ± 0.7
WH, 140 GeV	56.6	34.4	24.2	16.8	13.6	10.6 ± 1.2
WH, 150 GeV	68.1	44.1	27.8	20.0	15.2	12.3 ± 1.2
WH, 160 GeV	65.8	46.9	31.3	21.0	17.2	14.0 ± 1.3
WH, 170 GeV	50.8	37.9	26.4	19.0	14.7	11.9 ± 1.2
WH, 180 GeV	45.6	34.6	21.9	13.5	9.6	8.2 ± 0.8
WH, 190 GeV	30.7	22.8	13.3	10.0	7.3	5.9 ± 0.6
WZ 3l	460.5	351.1	122.1	77.1	0.72	$0 + 0.4$
ZZ	71.4	62.7	27.9	20.0	0.36	0.04 ± 0.01
WW	0	0	0	0	0	$0 + 0.5$
$t\bar{t}$	37.7	14.4	12.6	5.4	1.8	1.8 ± 1.8
$Wb\bar{b}$	0	0	0	0	0	0
$W + jets$	0	0	0	0	0	0
Wt	0	0	0	0	0	0
Sum of background events						$1.8^{+1.9}_{-1.8}$

Table 7.2: Cutflow for the WH3L analysis for the different Higgs masses studied. Cross sections normalised to $\mathcal{L} = 30$ fb^{-1}. The errors include only statistical uncertainties due to Monte Carlo statistics.

Chapter 8

Systematic Uncertainties

The results presented in chapters 6 and 7 are not only affected by statistical uncertainties, which depend on the limited statistics of Monte Carlo events. An additional source that is more difficult to investigate are systematic uncertainties. These uncertainties can be classified as

- theoretical uncertainties and

- experimental uncertainties

As discussed earlier, the description of parton interactions is theoretically not understood in detail. Hence, by not being able to describe this process analytically, it has to be approximated. This is done by so-called parton density functions. They do contain errors, which have to be considered in the treatment of uncertainties, as well as effects due to the renormalisation scale and initial or final state radiation. For WH production, the uncertainty of the parton density functions is less than 5% [10] and the uncertainty of the energy scale is less than that [56]. These uncertainties and effects due to initial and final state radiation sum up to a total theoretical uncertainty of 9%.

There are also experimental uncertainties that contribute to the systematic errors. Those effects will be discussed now in more detail. All assumptions are made for an integrated luminosity of $\mathscr{L} = 30$ fb^{-1} for a centre-of-mass energy of $\sqrt{s} = 14$ TeV.

The luminosity is one of the sources of experimental uncertainty. Measurement methods have already been discussed in chapter 3.3. It should have become clear, that an exact determination of this parameter is very difficult and it is expected to be the main contribution to the systematic uncertainty in the early data taking period. The rough knowledge of machine parameters like bunch currents or beam profiles lead to an initial uncertainty of $20 - 30\%$. Better determination of these parameters and availability of the luminosity detectors will decrease this uncertainty to 5%. High precision measurements of the luminosity can be reached by incorporating results of precision calibration processes, e.g.

W/Z counting. Therefore, for a long running period, as necessary for this analysis, which corresponds to $\mathscr{L} = 30$ fb^{-1} at $\sqrt{s} = 14$ TeV, the accuracy of the luminosity measurement is assumed to be 3% [10].

Further systematical uncertainties arise through the reconstruction of the physics objects, i.e. leptons or jets. There are several sources of uncertainties related to this.

The ATLAS detector has a 4π layout, which means that the full solid angle is covered. Nevertheless, this layout is not perfect. There are gaps in the detector, e.g. for accessibility for maintenance work. It is possible that particles escape the detector and can not be reconstructed. Other factors that reduce the reconstruction efficiency are related to the detector response. All subdetectors have a certain dead time, which means that the read-out of electronics channels takes some time in which the respective components are not sensitive. The uncertainty of the identification of electrons (muons) is 0.2% (1%). As an example, the actual uncertainty of the muon identification can be determined with the so-called *tag and probe* method [57]. This technique uses the decay of Z bosons into two muons. Both muons produce tracks in the Inner Detector and the Muon Spectrometer. One of the reconstructed objects (a muon with Inner Detector track and Muon Spectrometer track) will be regarded as *tagged* while for the second muon the existence of a matched track in the in Muon Spectrometer with the Inner Detector track is *probed*. From that it is possible to determine the efficiency of the Muon Spectrometer. The reconstruction efficiency of muons is limited due to several factors: the huge ATLAS muon system is very difficult to align, small deviations have a large impact and the energy loss in the transition of the detector material fluctuates. Further effects are ambiguities with the track fitting and resolution of the monitored drift tubes. Figure 8.1a illustrates the impact of the uncertainty of the muon energy scale.

The energy scale of electrons is determined by the calibration of the electromagnetic calorimeter, the uncertainty has been modelled by varying the transverse energy of electrons by $\pm 1\%$. The uncertainty of the energy scale of the muons arise from the imprecise knowledge of the magnetic field, again an uncertainty of 1% has been considered.

The resolution of the lepton energy is affected not only by the capabilities of the subdetectors, but also by the material distribution within the detector. The impact of the limited resolution of the reconstruction has been estimated for muons by smearing the inverse momenta with a Gaussian with a width of $\sigma_{1/p_T} = 0.011/p_T \oplus 0.00017$ (p_T in GeV) [10]. The influence of the resolution of the electron reconstruction has been estimated by varying the p_T about $\pm 0.5\%$.

Jets in principle are affected to the same uncertainties, especially the jet energy scale is expected to show larger uncertainties. As described earlier, jets are measured in the calorimeter. To exactly measure the energy of a jet, the deposited energy has to be assigned to a certain jet. Moreover, additional detector effects, like dead material have to be understood in detail. The difference between leptons

(a) Muon energy scale   *(b)* Jet energy scale
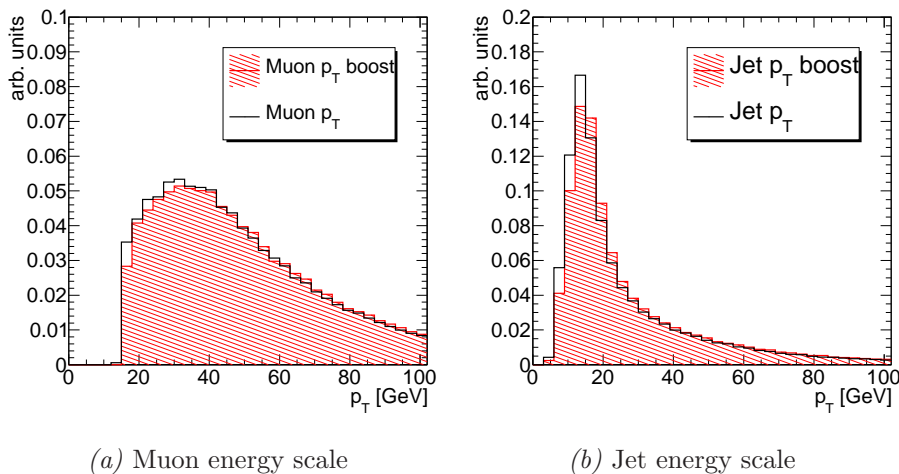
Figure 8.1: Figure *a)* illustrates the effect of the uncertainty of the transverse momenta of the muons and figure *b)* the impact of the jet energy scale of the jets.

and jets is their composite character, the lack of reference data from a testbeam and the limited quality of the hadronic shower simulation. In the beginning, the jet energy scale will therefore have a large uncertainty, but at higher luminosities the error is assumed to be of the order of 7% [10]. The same effects apply for the resolution of the jet energy, because the jet measurement is done in the calorimeters. This effect is also expected to be 7%, the consequences of varying the jet energy are illustrated in figure 8.1*b*.

The missing transverse energy is calculated from the quantities reconstructed in the detector and therefore depends on the respective errors. Hence, the missing energy is recalculated depending on the variation of these uncertainties.

Table 8.1 summarises the effects of the systematic uncertainties on the signal and the background. The total experimental uncertainty due to systematical uncertainties is the quadratic sum of the respective contributions. The large influence of the jet energy scale on the $\Delta WH(2L)$ is an effect of statistical fluctuations. Additionally, because of the limited statistics, the effects of the respective sources of uncertainty on the background have been estimated after the preselection, not after the full selection as for the signal. The large integrated luminosity has two consequences for this analysis. On the one hand, the systematic errors will be understood well and therefore be small. On the other hand, the needed statistics for a Monte Carlo study increases quickly. Therefore, compared to the statistical uncertainties (which are proportional to the number of remaining events after the cuts), the contribution of the systematic errors is small.

The experimental uncertainty of table 8.1 is the quadratic sum of the respective uncertainties. It is dominated by the uncertainty of the luminosity. The

uncertainty for the WH2L channel is dominated by the jet energy scale. This is an outlier due to statistical reasons: because of limited statistics, even small fluctuations of the number of events after the cuts have a substantial impact. Other uncertainties have only minor impact on the total uncertainty. In general, the analysis is limited by statistical uncertainties and not by systematic effects, which are expected to be understood sufficiently at larger integrated luminosities, such as $\mathscr{L} = 30 \text{ fb}^{-1}$.

Source of the uncertainty	%	WH2L (%)		WH3L (%)	
		$\Delta WH(2L)$	Δ background	$\Delta WH(3L)$	Δ background
Luminosity	3	3	3	3	3
Electron ID efficiency	0.2	0.2	1.2	0.4	0.5
Muon ID efficiency	1	2.0	0.7	1.55	2.7
Electron energy scale	0.5	0.26	0.3	0.18	0.5
Electron energy resolution	0.5	0	1.0	0.15	0.2
Muon energy scale	1	0.4	0.9	0.3	2.2
Muon p_T resolution	gauss.	0	0.9	0.15	3.6
Jet energy scale	7	15.0	0	3.1	0
Jet energy resolution	7	1.3	0	0.9	0
Experimental uncertainty		±15.5	±3.7	±4.7	±5.9

Table 8.1: Overview of the systematic uncertainties on the signal and the backgrounds for the two-lepton and three-lepton final states. The backgrounds include only WW, WZ, ZZ and $t\bar{t}$ and are limited by the available statistics. The term *gauss.* in the table is specified by the gaussian smearing of the p_T value with a width of $\sigma_{1/p_T} = 0.011/p_T \oplus 0.00017$ (p_T in GeV).

Chapter 9

Discovery Reach for the Associated WH Production

The previous chapters have been dedicated to the analysis of the associated WH production. Analysis strategies for two different and independent decay channels have been presented. After shortly recapitulating these results the discovery potential of both the separate channels as well as in combination will be derived.

9.1 The Statistical Description

There are two different approaches to statistical data analysis, the frequentist and the Bayesian method. The frequentist interpretation assumes a large number (in theory: an infinite number) of repeated experiments. The frequentist probability is defined as the frequency of an event relative to the total number of trials:

$$P(X) = \lim_{N \to \infty} \frac{n}{N} \tag{9.1}$$

$P(X)$ is defined as the probability that an event is of type X, where n is the number of events of type X and N is the total number of events. This means that a sufficiently large number of trials is needed for the determination of the probability. Hence, this definition of probability can only be applied to repeatable experiments.

The Bayesian approach can also be applied to non-repeatable experiments. The concept of frequency or probability respectively is substituted by the *degree of belief*, which is based on well-specified information. In a mathematical way Bayes' theorem [58, 59] can be written for discrete variables as follows

$$P(A|B) = \frac{P(B|A)P(A)}{P(B)} \tag{9.2}$$

where

- $P(A)$ is the prior probability of A.

- $P(B)$ is the prior probability of B (for normalisation).

- $P(B|A)$ is the conditional probability of B given A.

- $P(A|B)$ is the conditional probability of A given B. It is called the posterior probability, as it depends on B.

The prior probabilities $P(A)$ and $P(B)$ can be measured or are already known from other experiments. $P(B|A)$ could for example be measured from the efficiency of a detector. From that, $P(A|B)$ can be determined.

If A and B are not a set of events but a set of hypotheses θ_i, then $P(\theta_i)$ is taken to be the degree of belief in this hypothesis. Then Bayes' theorem can be written as

$$P(\theta_i|\mathbf{X^0}) = \frac{P(\mathbf{X^0}|\theta_i) \cdot P(\theta_i)}{P(\mathbf{X^0})} \tag{9.3}$$

with θ_i being different hypotheses and $\mathbf{X^0}$ representing the data. In correspondence with equation 9.2, the different factors are

- $P(\theta_i)$ is the prior probability and represents the degree of belief in different hypotheses

- $P(\mathbf{X^0})$ is a normalisation constant

- $P(\mathbf{X^0}|\theta_\mathbf{i})$ is the probability of obtaining the observed measurements $\mathbf{X^0}$. This quantity depends on the detector.

- $P(\theta_i|\mathbf{X^0})$ is the posterior probability for hypothesis θ_i given observed data $\mathbf{X^0}$

Thus, the degree of belief before the measurement and the results of the measurement determine the degree of belief in a hypothesis after the measurement. Here the hypothesis is the background model which is determined by the results of the cut-based analysis.

In this thesis Bayes' theorem is applied by using a programme called BAT - the Bayesian Analysis Toolkit [60]. The posterior probability is determined by a numerical integration using a Markov chain Monte Carlo algorithm. The Metropolis algorithm mentioned in chapter 4.3.1 is an implementation of a Markov chain. The characteristic of a Markov chain is the uniform distribution of the chain which is reached after a certain number of steps. The method is based on a sequence of random numbers and the next element of the chain does only depend on its current state – and not on the previous history. In BAT the algorithm is implemented as follows:

- for a system in a given state x, a new state y is proposed.

- the posterior probabilities of the new state and the current state are calculated and their ratio r compared to a random number U.

- if $U < r$, the new state is set to y, otherwise it is x.

This way the posterior probability density functions (pdf) can be calculated. The pdfs and their meaning will be discussed in the following chapters. In chapter 9.2.1 the individual limits for the WH2L and the WH3L channel will be calculated and in chapter 9.2.2 the combination of both channels will be derived. The discussion will focus on one Higgs boson mass ($m_H = 160$ GeV), while the result will be given for the full mass range.

9.2 Calculation of the Discovery Reach

9.2.1 Significance of the Individual Decay Channels

Following the explanations above, the pdf will be calculated for each background separately and for the combination of all backgrounds. This will be compared to the pdf of the combination of signal and background. BAT takes as input the absolute number of events after the cut-based selection (this corresponds to Monte Carlo events) and scales them using the weight for each event, i.e. takes the cross-section into account. Thus, the statistical error is considered. The luminosity is included by convolving the cross-section distributions of each background with the appropriate Gaussian distribution. All values are convolved with the gaussian distributions of the respective systematic error as discussed in chapter 8.

The posterior probability density functions for the respective backgrounds for the WH2L channel are shown in figure 9.1. The numbers are the median values to be expected for an integrated luminosity of 30 fb^{-1} as well as the errors, N_b^{exp}. The yellow shaded area is the 68% interval (also referred to as 1σ interval), or if the parameter is at the lower limit, the lower 95% limit is shown. A pdf is at the lower limit, if after the cut selection no events are left. That means that *probably* no events can be expected at all when compared to data. Nevertheless, this statement is not necessarily true. It could also be up to limited statistics that no events are seen after all cuts. To account for this uncertainty, a flat prior has been chosen. By that conservative approach, the posterior does not get suppressed for expected background numbers larger than zero. Therefore, even though the absolute number of events after the cut selection might be zero, I *believe* there is a chance (defined by the pdf) that there are events left when repeating the experiment with larger statistics.

The particular pdfs are then combined into one pdf, henceforth called $P_b(N|MC)$, corresponding to the overall probability density expected for the backgrounds at
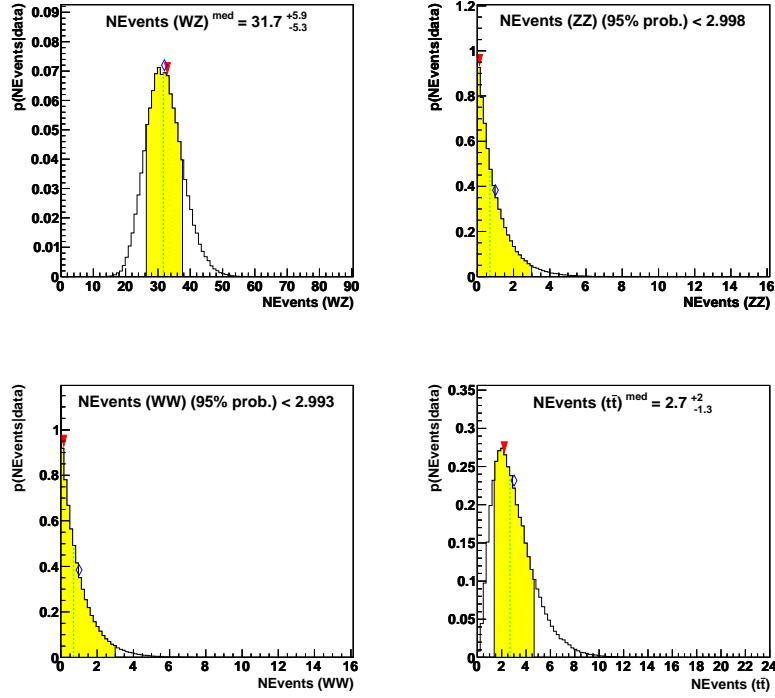
Figure 9.1: These plots show the posterior probability of the backgrounds for the WH2L channel according to the background model. The numbers in the plots (NEvents) are not scaled to the luminosity, but can be compared with the actual number of events after all cuts. Clockwise from upper left: WZ, ZZ, WW and $t\bar{t}$. The green line represents the median, the blue diamond the mean value and the global mode is marked with a triangle. The global mode is the single value with the largest probability encountered by the Markov Chain in the multidimensional phase space. The 68% interval (with respect to the mean value) is yellow shaded. If the posterior *pdf* is on the lower limit for one of the backgrounds, the 95% probability lowest interval is shown.

	130 GeV	140 GeV	150 GeV	160 GeV	170 GeV	180 GeV	190 GeV
WH2L	2.66	3.68	4.31	4.65	4.81	3.84	3.06
WH3L	1.58	2.47	2.60	2.85	2.60	2.05	1.74
combined	2.95	4.18	4.64	4.99	5.04	4.10	3.20

Table 9.1: Discovery limits for the channels separately and combined. $\mathscr{L} = 30$ fb^{-1}.

the given luminosity. Figure 9.2 illustrates the posterior for the WH2L channel. The median is calculated as $12.9^{+5.4}_{-4.3}$ events, which means that for an integrated luminosity of 30 fb^{-1} a total number of $12.9^{+5.4}_{-4.3}$ background events will be expected, given the background hypothesis. Of course, the contribution of each background is different, depending on the respective cross-section and rejection efficiency, presented in chapters 6 and 7.

The same can be done including the signal, which leads to the posterior $P_{s+b}(N|MC)$ shown in figure 9.2. For the WH2L analysis, the median is calculated to be $29.1^{+7.4}_{-6.5}$ events. For a derivation of the discovery reach for a certain mass point, the background only hypothesis has to be compared to the "signal + background" hypothesis. The expected number of events after the selection process, N^{exp}_{s+b}, is chosen to be at 50% of the *pdf*, which translates into a 50% probability of N_{s+b} either being smaller or larger than that. The probability of 50% equals the median of the probability density function and is therefore the natural choice. Using N^{exp}_{s+b}, the probability of the background only hypothesis can be calculated as

$$P_b^{WH2L}(N|MC) = \int_0^{N^{exp}_{s+b}} P_b(N|MC) \tag{9.4}$$

This probability can directly be translated into a significance using the error function

$$\mathrm{Erf}(x) = \frac{2}{\sqrt{\pi}} \int_0^x e^{-t^2} dt \tag{9.5}$$

The significance for the WH2L analysis channel is shown in figure 9.7 and summarised in table 9.1.

The same procedure is applied for the WH3L channel. The respective probability densities for the backgrounds are shown in figure 9.3. Figure 9.4 illustrates the *pdf*s for background only and the "signal + background" hypothesis. Again, the significance for a discovery can be calculated; the result is shown in figure 9.7 and summarised in table 9.1.

(a) Background only

(b) Signal + Background
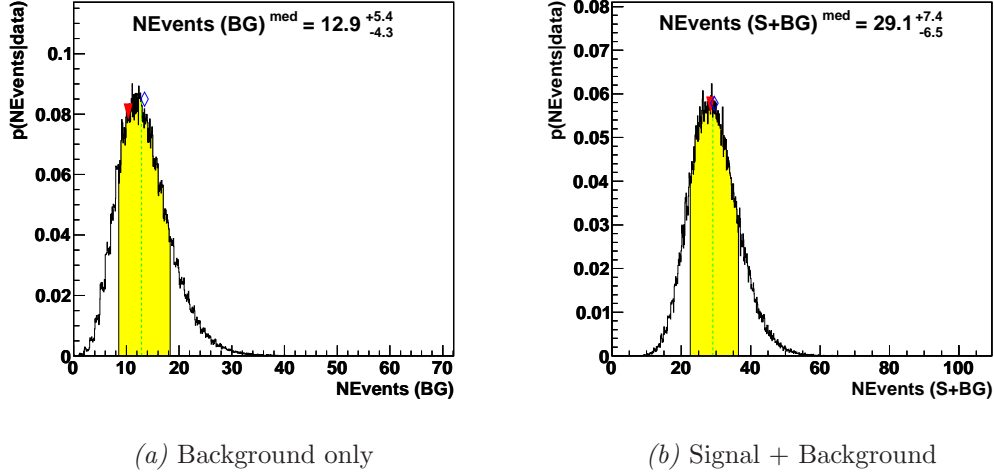
Figure 9.2: *a*): the probability density function of the background of the WH2L chan-
nel. *b*): the probability density function of signal and background of the
WH2L channel. All numbers are normalised to $\mathscr{L} = 30$ fb^{-1}.

9.2.2   Combination of Both Analysis Channels

Now that the significance of the individual channels has been derived, they will
be combined. As highlighted earlier, both channels are orthogonal, i.e. events
can only be allocated to exactly one channel – or discarded. Nevertheless, the
systematic errors are correlated and have therefore been considered accordingly.
To calculate a combined discovery limit that is comparable to the single limits
the expected number of events has to be reduced, such that the product of the
respective probabilities is 50% (as for the single limits). Hence,

$$P_{s+b}^{WH2L}(N|MC) \cdot P_{s+b}^{WH3L}(N|MC) = 0.5 \qquad (9.6)$$

Both channels have the same weight and therefore eq. 9.6 is equal to

$$P_{s+b}^{WH2L}(N|MC) = P_{s+b}^{WH3L}(N|MC) = \sqrt{0.5} = 0.707 \qquad (9.7)$$

This leads to a 2-dimensional probability density function, which is shown in
figure 9.6, calculated for both the background only as well as the signal + back-
ground hypothesis. The black lines indicate the 70% limit for the respective
channel. For example, in the WH2L (WH3L) channel there is a probability of
70% that 40 events (13 events) or more will be measured. The product of these
probabilities translates to a probability of 50% that at least 40 events will be
measured for WH2L *and* at least 13 events for WH3L. The upper right quad-
rant corresponds to this product. Thus eq. 9.5 can be used in the same way as
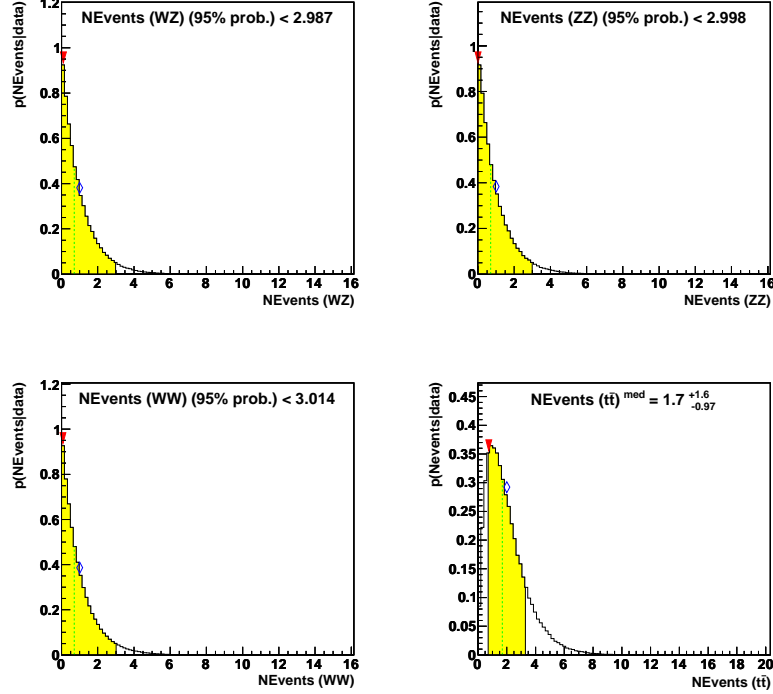
Figure 9.3: These plots show the probability density functions of the backgrounds for the WH3L channel. Clockwise from upper left: WZ, ZZ, WW and $t\bar{t}$.
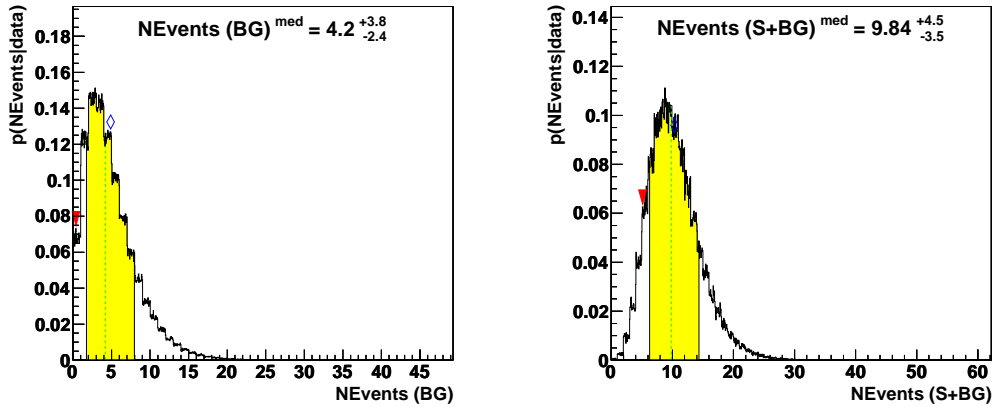
Figure 9.4: Left: the probability density function of background only of the WH3L channel. Right: the probability density function of signal and background of the WH3L channel.
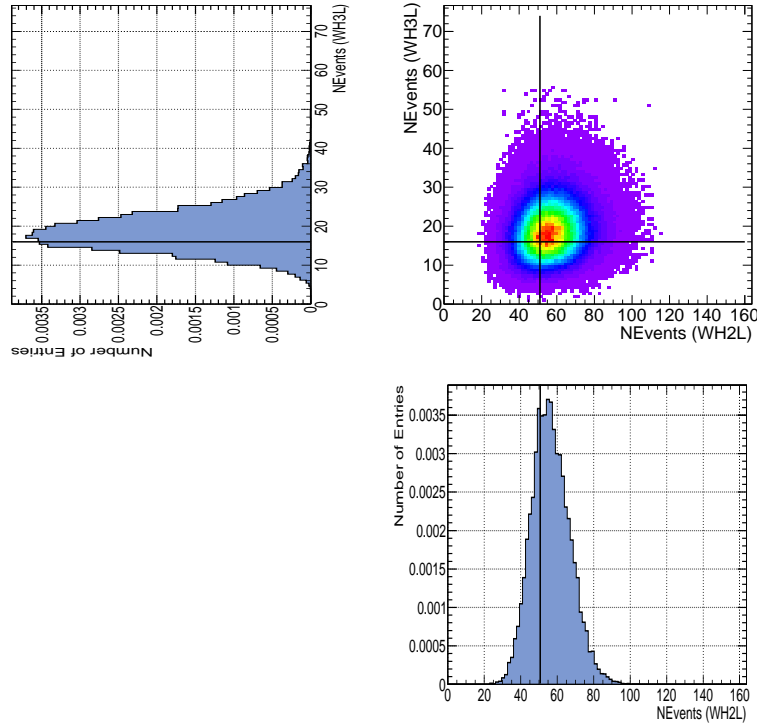
Figure 9.5: Illustration of the two-dimensional *pdf* for $m_H = 160$ GeV. The upper left
plot shows the projection onto the y-axis (WH3L) and the lower right plot
shows the projection onto the x-axis (WH2L). The black lines indicate the
70% threshold, as explained in eq. 9.6.

for the single channels to calculate the significance for the combination of both
channels. The result for the combined significance for all mass points can be
seen in figure 9.7 as well as in table 9.1. A reduced selection efficiency of 10%
for signal and background has also been considered. This leads to a reduction of
the significance of 5%. As a result it can be stated that for sufficient data the
associated WH production can improve the discovery limits of a Standard Model
Higgs boson over a wide mass range.
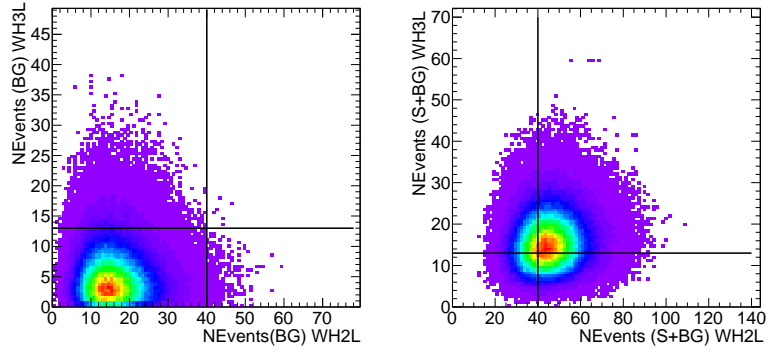
Figure 9.6: The 2-dimensional pdf of the expected background only distributions (left) and the pdf including the signal (right).
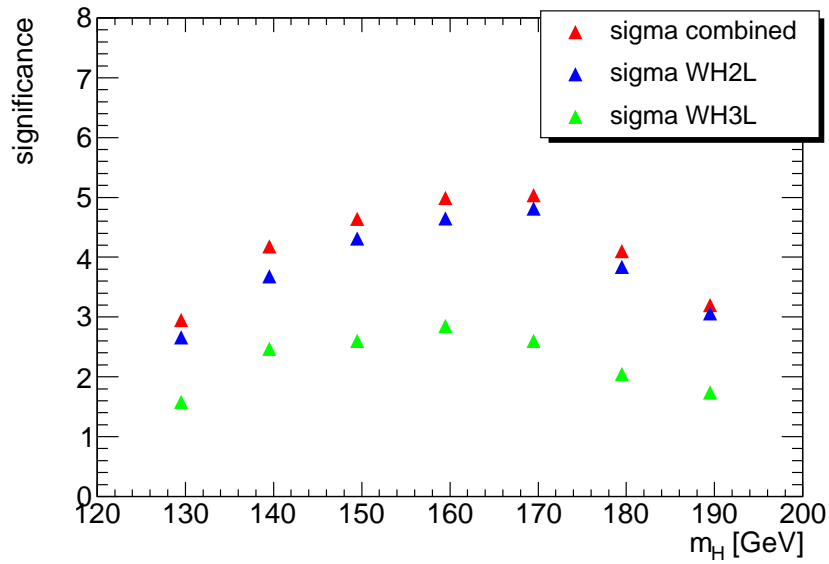
Figure 9.7: The expected significance for the discovery of a Higgs boson, based on the presented analysis.

Chapter 10

Summary and Outlook

The Higgs boson is the last particle missing to complete the Standard Model of particle physics: even though this model has been a tremendous success and describes the electroweak and the strong interaction of particles, it can not predict the masses of the bosons of the electroweak forces. The Higgs mechanism is one model to overcome this drawback through a spontaneous symmetry breaking, which produces a new particle: the Higgs-boson. So far, the Higgs boson has not been found, only constraints on the mass of this particle could be derived. Therefore, it will be one of the most important tasks of the LHC experiments at CERN to discover or exclude the existence of a Standard Model Higgs boson. If the Higgs boson can be found, the precise determination of its properties will be a challenging task.

The data taking of the Large Hadron Collider will start colliding proton beams by the end of 2009 with a centre-of-mass energy of $\sqrt{s} = 7$ TeV. The ATLAS detector is one of four large experiments at LHC and one of two multi-purpose detectors with a broad research area. This thesis is based on Monte Carlo generated events and dedicated to the production of a Higgs boson in association with a W boson at a centre-of-mass energy of $\sqrt{s} = 14$ TeV. A mass range of the Higgs boson of $130 - 190$ GeV (in 10 GeV steps) has been investigated for two orthogonal decay channels. The results of both analysis channels have been optimised with one-dimensional cuts.

Firstly, the mixed hadronic-leptonic decay channel: $WH, H \rightarrow WW, WWW \rightarrow 2l2\nu + 2$ jets with $l = e, \mu$ has been investigated. In the mixed channel, stringent cuts on the transverse momenta of the two leptons have been shown to be very efficient. All events have been filtered for exactly two leptons with the same charge, in order to reject many possible background contributions. Further cuts to discriminate background events have been applied on the invariant mass of the jets and the missing transverse energy.

The pure leptonic decay is the second decay channel investigated: $WH, H \rightarrow WW, WWW \rightarrow 3l3\nu$ with $l = e, \mu$. This channel is independent from the mixed channel and requires at least three leptons as input. Again, strict cuts on the

transverse momenta of the leptons have been applied. Furthermore, the spin correlation of the decay products of the Higgs boson has been utilised, as well as a cut on jet energies and the missing transverse energy. A very important cut for this channel is the rejection of events with an invariant mass that resembles the Z boson mass.

The discovery reach has been calculated for both channels separately and finally both channels have been combined, including the correlations of the systematic uncertainties using a Bayesian ansatz. Nevertheless, the discovery reach as derived in this thesis is limited by the statistical uncertainty. Systematic uncertainties are expected to be understood sufficiently at larger integrated luminosities (such as $\mathscr{L} = 30$ fb^{-1} for this thesis), on the other hand, especially the background is dominated by processes with large production cross-sections. The statistical limitation of event samples has been considered in the statistical error using a Bayesian method in order to not suppress contributions of backgrounds with no events after applying all cuts. The discovery reach derived for a Standard Model Higgs boson, produced in association with a W boson by colliding two protons with a centre-of-mass energy of $\sqrt{s} = 14$ TeV has been derived. It has a maximum of 5.04σ for a mass of the Higgs boson of $m_H = 170$ GeV. All discovery limits are summarised in table 9.1.

To conclude, this channel contributes to a prospective discovery of a Standard Model Higgs boson in the mass range of $130 - 190$ GeV. It is suitable for larger integrated luminosities, such as $\mathscr{L} = 30$ fb^{-1} (as used for this study). It is also an interesting channel to be studied for precision measurements of the properties of the Higgs boson, for example for measuring the coupling to W bosons.

Appendix

Appendix A

Distributed Computing at ATLAS

A.1 The ATLAS Computing Model

Modern experiments in particle physics have to cope with huge data rates. For example, in the last century bubble chambers were widely used for particle identification: the tracks of particles have been photographed and then analysed. With experiments getting larger, the data taking procedure became not only more sophisticated but also more complex. The ATLAS experiment will face data of several Petabytes per year, which has to be stored and processed. The reconstruction of the raw physics events is also very time consuming, i.e. on modern CPUs the reconstruction of one single event takes approximately 15 minutes. Clearly, at event rates of 1 GHz, it is impossible to consider every event. Still, after triggering and selecting only interesting events, a rate of 200 Hz remains (this has been explained in chapter 4.2). At design luminosity 10^9 events will be recorded per year. Each event consumes $1 - 2$ MB of disk space and several replicas of one event will be stored. To be able to cope with this enormous amount of data, large computing facilities with an overall computing power of more than 100000 modern CPUs are needed. This can not be done at one single computing facility, but has to be shared.

ATLAS uses a Grid structure for its computing purposes. This leads to a decentralised infrastructure of the computing resources[1], which are shared among

---

[1]The distribution of computing resources is a fundamental feature of a computing Grid, while the well known World Wide Web (WWW), invented in 1989 by Sir Tim Berners-Lee at CERN, distributes information.
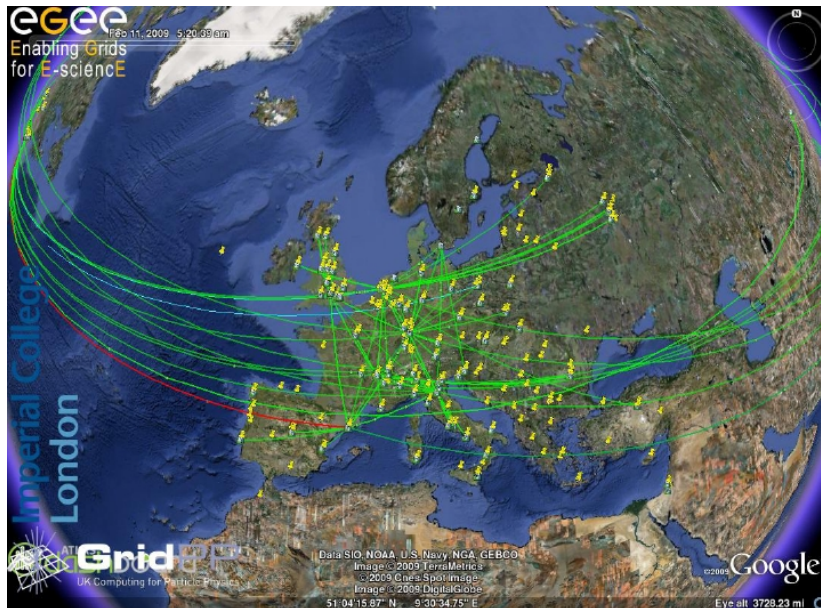
Figure A.1: This figure illustrates the data transport from CERN to and among the Grid computing facilities during as seen on a real time monitoring application.

the countries that are involved in the ATLAS experiment. An illustration is shown in figure A.1. The structure of the Grid has analogies to a spiderweb. The respective computing centres have distinct roles, especially the *centre* of the Grid is represented by CERN, where the experiments are located at [61].

The raw data taken by the subdetectors of ATLAS, e.g. the Muon Spectrometer, is recorded and stored at CERN – this is the first stage of data processing. The computing facility at CERN is referred to as Tier-0 centre. The data is archived, reconstructed and then distributed within 10 so-called Tier-1 facilities, which are located around the globe. Each Tier-1 centre is supposed to store 1/10 of the data. The main purpose of the Tier-1 centres is the storage and reprocessing of raw data (ESD, AOD and other relevant storage objects) and – within boundaries – they also provide computing access for analysis purposes.

The computing facilities in the next layer are called Tier-2 centres, approximately 40 sites are under operation. These are the main facilities to be used for physics analyses. Additionally, these computing facilities are used for the simulation of physics events. Therefore, the Tier-2 centres will host mostly AOD files, which are the basis for physics analyses, like the one presented in this thesis.

The lowest layer are Tier-3 resources, which correspond to the computing resources at an institute. This comprises dedicated storage and computing systems, but also desktop machines. These resources may be Grid-enabled and their main task is the storage of Ntuples which are used for analyses. All computing

facilities consist of two basic elements: a compute element (CE) and a storage element (SE).

The Tier-0 at CERN is expected to have an extremely high availability but also provides a buffer system of roughly 130 TB for data which corresponds to approximately five days of data taking with design parameters. Tier-1 centres must also provide a high availability, because a latency of data transport from CERN to the Tier-1 will be problematic to catch up. Tier-2 centres may have a lower availability than Tier-1 centres.

A.2 File Catalogue

As mentioned above, the ATLAS experiment will process huge amounts of data. This includes not only event data, which corresponds to physics events[2], but also calibration data and other data not connected to the physics events but necessary for running the experiment. This discussion concentrates on event data. The management of this data, which is in the order of 10 PB per year, is one of the main tasks of computing operations. Obviously, not all data that might be needed for a certain analysis can be expected to be stored at one computing facility. At ATLAS a system for distributed data management (DDM) called DonQuijote 2 (DQ2) is used. DQ2 manages over 10 Petabytes of data per year, which corresponds to 120 million files and 1.3 million datasets. These are distributed over more than 500 storage end points within the Grid [62]. For the management of the data, all sites are queried regularly and the information gets stored in a database at CERN. This database contains information about datasets, their location (i.e. at which computing facility it is stored) and a unique identifier of each file. While the physical filename may be different for copies of a file, each file can be identified by a globally unique identifier (GUID)[3], which is stored in the DQ2 database.

Each Tier-1 centre has associated Tier-2 computing facilities, which are organised as a computing cloud. For example, in Germany the Tier-1 centre is called GridKa and located in Karlsruhe. Several regional Tier-2 centres, e.g. the Leibniz-Rechenzentrum in Munich or DESY in Hamburg are associated to GridKa. Each Tier-1 centre has a file catalogue, called LCG File Catalogue (LFC), with information about the files stored within the respective cloud. This database contains information about the physical location of files and connects this with the GUID of the DQ2 database. Thus, to access a certain file, the DQ2 database at CERN has to be queried, as well as the respective LFC in order to get the exact location of a file [4].

---

[2]In this context, event data comprises real data as well as simulated data.

[3]In fact, the number is not guaranteed to be unique, but the probability of two different files having the same GUID is extremely low, given the number space is 2^{128}.

[4]The physical location of a file can be expressed through a so-called Storage URL (SURL).
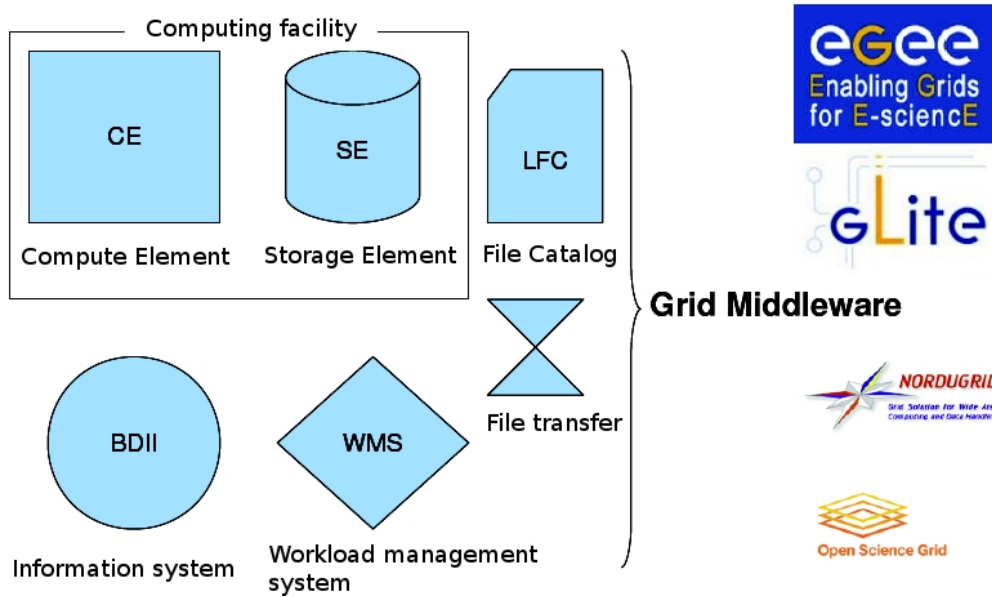
Figure A.2: Components of the Grid as used with ATLAS.

A.3 The Grid Middleware

At ATLAS three different Grid systems are used: EGEE[5], OSG[6] and NorduGrid[7]. The access to the computing facilities of a Grid for computing or storage purposes is done through software called middleware – as illustrated in figure A.2. The middleware allows to submit requests to the Grid system in order to execute a computation.

For example, the EGEE Grid uses gLite as middleware. gLite consists of a set of programs which can be used by the physicist to interact with the computing resources. However, the ATLAS software is designed to be independent of the respective middleware used. Athena will be installed at all computing centres and the decision which of the resources to be used is not made by the user, but by the workload management system (WMS) and the information system (BDII). These systems keep track about the load and properties of the individual computing resources that are available. The user only describes the requirements of a certain job and the BDII and the WMS delegate the job according to certain rules.

The authentication and authorisation of a single user is done by a X.509 certificate, which identifies the user as member of a Virtual Organisation (VO). All data that belongs to a VO can be read by a member, for example for analysis

---

[5] **E**nabling **G**rid for **E**-scienc**E**. EGEE is mostly an European and Asian project.

[6] **O**pen **S**cience **G**rid. This system is mainly used across USA.

[7] This refers to a middleware technology used in northern European countries.

jobs. The term *job* refers to a programme, usually written by a physicist, that performs certain tasks, like the analysis of a dataset on a remote computing facility. An example is given in chapter A.4 of this appendix.

Additional access rights of a user are determined by roles. For example, users that are associated to a German institute will acquire a role which gives them priority access to computing facilities that belong to German institutes, if there are extra resources available.

A.4 A Distributed Analysis Example

Typically, a physicist wants either to analyse data or simulate physics processes. This could be the generation of Monte Carlo events of a Higgs boson produced in association with a W boson as carried out in this thesis.

As the simulation and processing of one single event takes approximately 15 minutes, the production of several thousand events is very time consuming. Thus, it makes sense to distribute the computing onto many independent CPUs: as the physics events are independent from each other, the CPUs do not need to be interconnected.

The user creates a script which contains commands to run ATHENA, e.g. to produce 10000 events of a certain physics process using a Monte Carlo event generator like MC@NLO. The user submits a job using the middleware directly or via an interface, e.g. GANGA[63]. The middleware then interacts with the components of the grid, which are hidden from the user. From the bulk of the computing facilities the workload management system (WMS) and the information system (BDII) consider factors as availability of CPUs, free storage or required software and then delegates the job to a certain site, or even a number of sites. A very important feature is that the physicist does not need to know where the data actually is stored. The job gets transferred to the data.

After the job has run the output gets stored at a storage element and registered in the DDM catalogue. The user gets notified about the output of the job and then can proceed with the data, for example the user can carry out an analysis using Ganga and Athena. The information of the job output is then stored in the file catalog and also reported back to the user, who can then proceed with the analysis of the data.

List of Figures

List of Tables

Bibliography

[1] C. Amsler et al. Review of particle physics. *Phys. Lett.*, B667:1, 2008. 2.1, 2.2

[2] Peter W. Higgs. Broken symmetries, massless particles and gauge fields. *Phys. Lett.*, 12:132–133, 1964. 2.2

[3] Peter W. Higgs. Spontaneous Symmetry Breakdown without Massless Bosons. *Phys. Rev.*, 145:1156–1163, 1966. 2.2

[4] F. Englert and R. Brout. Broken symmetry and the mass of gauge vector mesons. *Phys. Rev. Lett.*, 13:321–322, 1964. 2.2

[5] G. S. Guralnik, C. R. Hagen, and T. W. B. Kibble. Global conservation laws and massless particles. *Phys. Rev. Lett.*, 13:585–587, 1964. 2.2

[6] Jeffrey Goldstone, Abdus Salam, and Steven Weinberg. Broken Symmetries. *Phys. Rev.*, 127:965–970, 1962. 2.2

[7] Abdelhak Djouadi. The Anatomy of electro-weak symmetry breaking. I: The Higgs boson in the standard model. *Phys. Rept.*, 457:1–216, 2008. 2.2

[8] M. Spira. V2HV, http://people.web.psi.ch/spira/v2hv/. 2.3

[9] A. Djouadi, J. Kalinowski, and M. Spira. HDECAY: A program for Higgs boson decays in the standard model and its supersymmetric extension. *Comput. Phys. Commun.*, 108:56–74, 1998. 2.4

[10] G Aad et al. Expected Performance of the ATLAS Experiment: Detector, Trigger and Physics. Technical report, Geneva, 2008. 2.4, 4.9, 5.1.4, 5.4, 5.4, 8, 10

[11] S Asai et al. Cross sections for Standard Model processes to be used in the ATLAS CSC notes. Technical Report ATL-PHYS-INT-2009-003. ATL-COM-PHYS-2008-077, CERN, Geneva, May 2008. 2.5

[12] R. Barate et al. Search for the standard model Higgs boson at LEP. *Phys. Lett.*, B565:61–75, 2003. 2.5.1

[13] Combined CDF and DZero Upper Limits on Standard Model Higgs-Boson Production with up to 4.2 fb-1 of Data. 2009. 2.5.1

[14] Martin W. Grunewald. Experimental Precision Tests for the Electroweak Standard Model. 2007. 2.5.2

[15] Michael Benedikt, Paul Collier, V Mertens, John Poole, and Karlheinz Schindl. *LHC Design Report.* CERN, Geneva, 2004. 3.1

[16] Jr. Callan, Curtis G. and David J. Gross. High-energy electroproduction and the constitution of the electric current. *Phys. Rev. Lett.*, 22:156–159, 1969. 6

[17] O. Biebel. Experimental tests of the strong interaction and its energy dependence in electron positron annihilation. *Phys. Rept.*, 340:165–289, 2001. 3.3

[18] Peter Jenni, Markus Nordberg, Marzio Nessi, and Kerstin Jon-And. ATLAS Forward Detectors for Measurement of Elastic Scattering and Luminosity. Technical report. 3.3, 3.3

[19] D. h. Perkins. INTRODUCTION TO HIGH-ENERGY PHYSICS. Reading, Usa: Addison-wesley (1982) 437p. 8

[20] ATLAS Collaboration. ATLAS: Detector and Physics Performance. Technical Design Report. Volume I. 4.1, 4.1.3

[21] G. Aad et al. The ATLAS Experiment at the CERN Large Hadron Collider. *JINST*, 3:S08003, 2008. 4.1, 4.1.2, 4.1

[22] A. Yamamoto et al. The ATLAS central solenoid. *Nucl. Instrum. Meth.*, A584:53–74, 2008. 4.1.1

[23] R. J. M. Y. Ruber and A. Yamamoto. Evolution of superconducting detector magnets. *Nucl. Instrum. Meth.*, A598:300–304, 2009. 4.1.1

[24] J P Badiou, J Beltramelli, J M Maze, and J Belorgey. ATLAS barrel toroid: Technical Design Report. Technical report, Geneva, 1997. 4.1.1

[25] ATLAS end-cap toroids: Technical Design Report. Technical report, Geneva, 1997. 4.1.1

[26] G. Aad et al. ATLAS pixel detector electronics and sensors. *Journal of Instrumentation*, 3(07):P07007, 2008. 4.1.2

[27] A. Ahmad et al. The Silicon microstrip sensors of the ATLAS semiconductor tracker. *Nucl. Instrum. Meth.*, A578:98–118, 2007. 4.1.2

[28] The ATLAS TRT collaboration. The ATLAS TRT Barrel Detector. *Journal of Instrumentation*, 3(02):P02014, 2008. 4.1.2

[29] The ATLAS TRT collaboration. The atlas trt end-cap detectors. *Journal of Instrumentation*, 3(10):P10003, 2008. 4.1.2

[30] Nicholas Metropolis and S. Ulam. The Monte Carlo Method. *Journal of the American Statistical Association*, 44(247):335–341, 1949. 8

[31] Stefano Frixione and Bryan R. Webber. Matching NLO QCD computations and parton shower simulations. *JHEP*, 06:029, 2002. 4.3.1

[32] E. Boos et al. Generic user process interface for event generators. 2001. 4.3.1

[33] G. Corcella et al. HERWIG 6.5: an event generator for Hadron Emission Reactions With Interfering Gluons (including supersymmetric processes). *JHEP*, 01:010, 2001. 4.3.1

[34] G. Corcella et al. HERWIG 6.5 release note. 2002. 4.3.1

[35] J. M. Butterworth, Jeffrey R. Forshaw, and M. H. Seymour. Multiparton interactions in photoproduction at HERA. *Z. Phys.*, C72:637–646, 1996. 4.3.1

[36] Michelangelo L. Mangano, Mauro Moretti, Fulvio Piccinini, Roberto Pittau, and Antonio D. Polosa. ALPGEN, a generator for hard multiparton processes in hadronic collisions. *JHEP*, 07:001, 2003. 4.3.1

[37] Michelangelo L. Mangano, Mauro Moretti, and Roberto Pittau. Multijet matrix elements and shower evolution in hadronic collisions: $Wb\bar{b} + n$ jets as a case study. *Nucl. Phys.*, B632:343–362, 2002. 4.3.1

[38] F. Caravaglios, Michelangelo L. Mangano, M. Moretti, and R. Pittau. A new approach to multi-jet calculations in hadron collisions. *Nucl. Phys.*, B539:215–232, 1999. 4.3.1

[39] Borut Paul Kersevan and Elzbieta Richter-Was. The Monte Carlo event generator AcerMC version 2.0 with interfaces to PYTHIA 6.2 and HERWIG 6.5. 2004. 4.3.1

[40] Torbjorn Sjostrand, Stephen Mrenna, and Peter Skands. PYTHIA 6.4 Physics and Manual. *JHEP*, 05:026, 2006. 4.3.1

[41] G. Duckeck et al. ATLAS Computing: Technical Design Report. 2205. 4.3.2

[42] G. Barrand et al. GAUDI - A software architecture and framework for building HEP data processing applications. *Comput. Phys. Commun.*, 140:45–55, 2001. 4.3.2

[43] G. Barrand et al. GAUDI - The software architecture and framework for building LHCb data processing applications. Prepared for International Conference on Computing in High- Energy Physics and Nuclear Physics (CHEP 2000), Padova, Italy, 7-11 Feb 2000. 4.3.2

[44] S. Agostinelli et al. GEANT4: A simulation toolkit. *Nucl. Instrum. Meth.*, A506:250–303, 2003. 4.3.2

[45] R. Brun and F. Rademakers. ROOT: An object oriented data analysis framework. *Nucl. Instrum. Meth.*, A389:81–86, 1997. 4.3.2, 5.2

[46] K Cranmer, A Farbin, and A Shibata. EventView - The Design Behind an Analysis Framework. Technical Report ATL-SOFT-PUB-2007-008. ATL-COM-SOFT-2007-012, CERN, Geneva, Sep 2007. 4.3.2, 5.2

[47] S. Dean and P. Sherwood. 4.3.2

[48] W Lampl et al. Calorimeter Clustering Algorithms: Description and Performance. Technical Report ATL-LARG-PUB-2008-002. ATL-COM-LARG-2008-003, CERN, Geneva, Apr 2008. 5.1.1

[49] S. Hassani et al. A muon identification and combined reconstruction procedure for the ATLAS detector at the LHC using the (MUONBOY, STACO, MuTag) reconstruction packages. *Nucl. Instrum. Meth.*, A572:77–79, 2007. 5.1.2

[50] I Gavrilenko. Description of Global Pattern Recognition Program (XKalman). Technical Report ATL-INDET-97-165. ATL-I-PN-165, CERN, Geneva, Apr 1997. 5.1.2

[51] J. M. Butterworth, J. P. Couchman, B. E. Cox, and B. M. Waugh. KtJet: A C++ implementation of the K(T) clustering algorithm. *Comput. Phys. Commun.*, 153:85–96, 2003. 5.1.3

[52] Stephen D. Ellis and Davison E. Soper. Successive combination jet algorithm for hadron collisions. *Phys. Rev.*, D48:3160–3166, 1993. 5.1.3

[53] M. Dittmar and Herbert K. Dreiner. How to find a Higgs boson with a mass between 155-GeV - 180-GeV at the LHC. *Phys. Rev.*, D55:167–172, 1997. 7.2.2

[54] Charles A. Nelson. Correlation between decay planes in Higgs boson decays into W pair (into Z pair). *Phys. Rev.*, D37:1220, 1988. 7.2.2

[55] E. W. Nigel Glover, J. Ohnemus, and Scott S. D. Willenbrock. Higgs boson decay to one real and one virtual W boson. *Phys. Rev.*, D37:3193, 1988. 7.2.2

[56] Oliver Brein, Abdelhak Djouadi, and Robert Harlander. NNLO QCD corrections to the Higgs-strahlung processes at hadron colliders. *Phys. Lett.*, B579:149–156, 2004. 8

[57] Matthias Schott. Study of the Z Boson Production at the ATLAS Experiment with First Data. *PhD Thesis, LMU Muenchen*, 2007. 8

[58] Rev. Thomas Bayes. An essay toward solving a problem in the doctrine of chances. *Phil. Trans. Roy. Soc. Lond.*, 53:370–418, 1764. 9.1

[59] Frederick James. Statistical methods in experimental physics. Hackensack, USA: World Scientific (2006) 345 p. 9.1

[60] Allen Caldwell, Daniel Kollar, and Kevin Kroninger. BAT - The Bayesian Analysis Toolkit. 2008. 9.1

[61] ATLAS computing: Technical Design Report. Technical report. A.1

[62] FH Barreiro-Megino, V Garonne, S Jezequel, M Branco, M Lassnig, and P Salgado. The ATLAS DQ2 Accounting and Storage Usage Service. Technical Report CERN-IT-Note-2009-010, CERN, Geneva, May 2009. A.2

[63] F Brochu, U Egede, J Elmsheuser, and K Harrison. Ganga: a tool for computational-task management and easy access to Grid resources. Technical Report arXiv:0902.2685, Feb 2009. A.4

Acknowledgements

Selbständigkeitserklärung

Ich versichere hiermit, die vorliegende Arbeit selbständig verfasst zu haben und keine anderen als die angegebenen Quellen und Hilfsmittel verwendet zu haben.

Benjamin Ruckert

München, im September 2009